

The background of the entire slide is a complex, abstract pattern of numerous thin, overlapping lines in various colors including purple, blue, green, yellow, and orange. These lines are oriented in many different directions, creating a dense, woven texture. Overlaid on this pattern are several thicker, solid-colored lines in shades of purple, blue, green, and yellow, which run diagonally across the frame.

# Properties of Ferritic/Martensitic Steels

July 12, 2023

Digital Materials Solutions, Inc.

7314 Golden Star Lane

Carlsbad, CA. 92011



## Contacts

Digital Materials Solutions Inc.  
7314 Golden Star Lane  
Carlsbad, CA 92011  
☎ 818-472-4669  
[ghoniem@ucla.edu](mailto:ghoniem@ucla.edu)

## Abstract

We present a comprehensive database for the ferritic-martensitic steel F82H. The database is intended to assist in the mechanical design of components manufactured from reduced activation 9 Cr steels (e.g. F82H), in particular, in a fusion reactor power source. The database is classified into three main categories: (1) fabrication and microstructure, (2) thermophysical properties, and (3) mechanical properties. The effects of irradiation (both neutron and ion) on the properties of F82H are also discussed. Data for each property is collected from various sources available in the public domain. The sources of data are given together with links to the original publication for verification or corrections. Various functional forms are developed to describe the properties of F82H as a function of temperature, and if available, as a function of the irradiation dose.

# Contents

<b>1</b>	<b>Introduction</b>	<b>4</b>
<b>2</b>	<b>Fabrication and Microstructure</b>	<b>6</b>
2.1	F82H Fabrication . . . . .	6
2.2	F82H Microstructure . . . . .	9
<b>3</b>	<b>Thermo-Physical Properties</b>	<b>13</b>
3.1	Coefficient of Thermal Expansion . . . . .	13
3.2	Specific Heat . . . . .	15
3.3	Thermal Conductivity . . . . .	16
3.4	Thermal Diffusivity . . . . .	17
3.5	Electrical Resistivity . . . . .	18
3.6	Thermal Emissivity . . . . .	18
<b>4</b>	<b>Mechanical Properties</b>	<b>20</b>
4.1	Elastic Properties . . . . .	20
4.2	Strength . . . . .	22
4.2.1	Yield Strength . . . . .	22
4.2.2	Ultimate Strength . . . . .	24
4.3	Ductility . . . . .	25
4.3.1	Uniform Elongation . . . . .	25
4.3.2	Total Elongation . . . . .	26
4.4	Stress-Strain Relationship . . . . .	28
4.5	Creep Properties . . . . .	30
4.5.1	Deformation Mechanisms . . . . .	30
4.5.2	Creep Strain Rate for HT-9 . . . . .	34
4.5.3	Creep Strain Rate for T91 . . . . .	35
4.5.4	Creep Strain Rate for F82H . . . . .	41
4.6	Fatigue Properties . . . . .	43
<b>5</b>	<b>Radiation Effects on Mechanical Properties</b>	<b>47</b>
5.1	Strength . . . . .	47
5.1.1	Yield Strength . . . . .	47
5.1.2	Ultimate Strength & Tangent Modulus . . . . .	51
5.2	Ductility . . . . .	52
5.2.1	Total Elongation . . . . .	52
5.2.2	Uniform Elongation . . . . .	52
5.3	Stress-Strain Relationship . . . . .	55
5.4	Volumetric Swelling . . . . .	57
5.5	Fracture Properties . . . . .	62
5.5.1	Ductile-Brittle Transition (DBTT) . . . . .	62
5.5.2	Fracture Toughness . . . . .	62
5.6	Irradiation Creep . . . . .	69
5.7	Fatigue Properties . . . . .	71
<b>6</b>	<b>Chemical Compatibility</b>	<b>73</b>
6.1	Liquid Metal Corrosion . . . . .	73
6.2	Liquid Metal Embrittlement (LME) . . . . .	77
6.3	Oxidation in Steam . . . . .	78

# 1 Introduction

Ferritic/martensitic (F/M) steels have been proposed as fusion structures for the past few decades, mainly because of their favorable response to neutron irradiation and their potential low-activation characteristics as compared to austenitic steels. Ghoniem et al. [1] estimated the effects of neutron irradiation on the lifetime of a ferritic/martensitic steel structural FW/B. They used available data and simple design rules (such as limiting the volumetric swelling strain to 5%) to show that an operating design window exists for such structures. The lower temperature limit is dictated by the shift in the Ductile-to-Brittle-Transition Temperature (DBTT), while the upper-temperature limit is dictated by creep strain accumulation and potential rupture. The structure lifetime in the intermediate temperature range is limited by volumetric swelling. To determine the precise operational temperature and lifetime of fusion structures, a validated property database is required. The objective of this document is to assemble such a database in forms that are suitable for large-scale structural and thermal analyses of the first wall and blanket components of fusion reactors.

Development of specific grades of F/M steels for fusion energy applications followed a parallel path to the larger effort of their development for the power industry, we mention here two fundamental differences. First, early efforts in introducing generations of fusion steels have recognized the importance and possibility of developing steels that have the characteristic of being “low activation” [2]. Second, the expected lifetime of structural materials in FW/B applications is only a few years, as opposed to the 40-60 year target for steels employed in most power industries. The first constraint has led to the elimination of Mo, Nb, Ni, Cu and N, and the introduction of W and V as carbide formers in place of Mo, while Ta was introduced as a replacement for Nb. In addition, the 7-9% Cr range was found to be very suitable in the elimination of the  $\delta$ -ferrite phase, which causes a reduction in fracture toughness.

Following parallel lines of development to fission reactor steels, the following generations of “fusion steels” have been developed (all compositions are in wt-%):[3]

1. *Gen-I. Low Activation F/M Steels (LAFMs)*: The first “low-activation” steel was developed in the mid-eighties on the basis of radioactivity and decay chain analysis of the main elements, and substitutions of Mo in low-Cr steels with V and W. The first such steel is the vanadium steel UCVS-1, with composition : 0.11C, 0.3Mn, 0.3Si, 2.46Cr, 0.05Ni, 1.5V, 0.02Mo, 0.007P, 0.015S, 0.015N, 0.043Al, 0.003Ti, 0.04Cu [2].
2. *Gen-II. Reduced Activation F/M Steels (RAFs)*: These steels have the composition range:  $\sim$ 0.1C, 0.04-0.3Si,  $\sim$ 0.45Mn, 8-9.4Cr, 1-2W,  $\sim$ 0.25V, 0.04-0.08Ta, 0.01-0.03N, 0.003-0.006B. They have been developed as follows:
  - (a) Japan: F82H, JLF-1 [4].
  - (b) Europe: Eurofer, Optifer-I, Optifer-II [5].
  - (c) US: 9Cr-2WVTa (CNA) [6].
  - (d) China: China Low-Activation Martensitic (CLAM) Steel [7].
3. *Gen-III. Oxide Dispersion Strengthened Reduced Activation F/M Steels (ODS-RAFM)*. These steels contain dispersoids of oxide particles (yttrium oxide and titanium oxide). Examples of steels under development are PM2000, MA957, with experimental grades of 9-12% Cr (martensites) and 12-20% Cr (ferrites). Although these steels are developed for fusion, they are also being considered for Gen-IV fission reactor steel applications in the cladding and structural supports. The alloy MA957 has a nominal composition 13.87Cr, 1.05Ti, 0.30Mo, 0.22Y<sub>2</sub>O<sub>3</sub>, 0.014C, 0.04Si, 0.13N, 0.1Al, 0.006S, while the alloy PM2000 has the composition of 19Cr, 5.5Al, 0.5Ti, 0.5Y<sub>2</sub>O<sub>3</sub>. W is sometimes used to replace Mo in fusion ODS steels, with lower Ti concentrations.
4. *Gen-IV. Super ODS-RAFM*. Mechanical alloying of metal and oxide powders is being developed to produce oxide dispersion-strengthened (ODS) ferritic alloys containing nano-scale oxide dispersoids.

For example, the alloy 12YWT has the composition: 13.3Cr, 0.92W, 0.46Ti, 0.13Y, 0.19O. The stability of these dispersoids at high temperatures and under irradiation has been studied recently. Ultrafine Ti-, Y- and O-enriched particles were found to be extremely resistant to coarsening during isothermal aging at 1300°C.

F82H is a ferritic-martensitic steel that has high chromium content and was developed as a reduced radioactivity variant from the commercial 9%-Cr steel (Grade 91) by replacing elements that have long-term radioactive decay chains, such as molybdenum, niobium, and nickel. The chemical composition of F82H is as follows (wt%): N=0.007, Ta=0.04, C=0.09, Si=.07, Mn=0.1, V=0.19, W=1.98, Cr=7.84, Fe=balance.

The development of RAFM steels is based on waste disposal considerations. Waste disposal considerations include:

1. Transportation of discharged components to a permanent storage or recycling site.
2. Burial disposal of waste materials.
3. Recycling of decommissioned materials if practical.

Let's define radiation dose units as follows.

#### Definitions

1. 1 mSv/a according to U.S. 10CFR-20.1301(a) is the dose limit for individual members of the public, total effective dose equivalent, per annum.
2.  $H = Q \times D$ ; H is tissue equivalent dose (1 Sv = 1 J/Kg), D is absorbed dose in Grays (1 J/Kg).

The transportation stage requires a limiting contact dose rate of 2 mSv/h without a radiation shield. The low-level, shallow-land (10CFR61 Class C) waste disposal is a more attractive waste disposal option for fusion. However, the ultimate waste management scenario is the recycling of used materials. For hands-on recycling, the limiting contact dose rate adopted is 25 mSv/h. RAFM steels are optimized for alloy compositions that can be recycled in several hundred years, and for minimum decay heat in accidents. This involves the elimination of elements that induce high radioactivity at shutdown, and those with long-term half-lives. The specific radioactivity after reactor shutdown for three candidate low-activation structural materials and the contact dose rate after the shutdown is shown in Fig. 1.

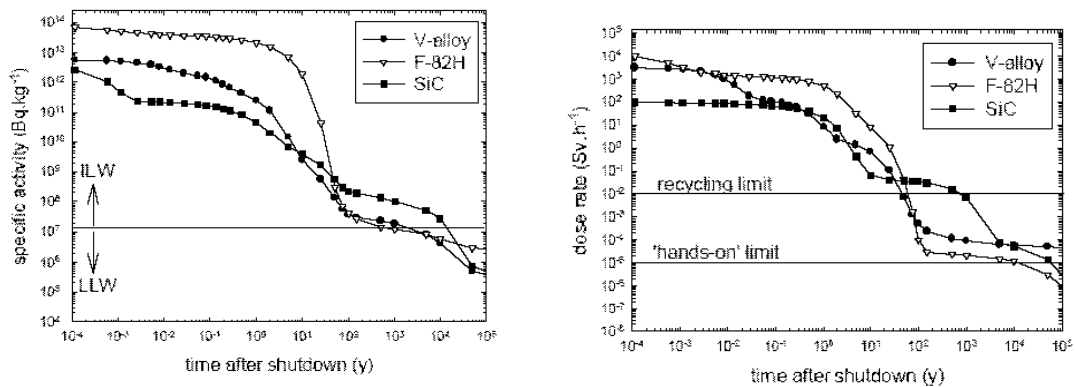


Figure 1: Specific activity response and Contact  $\gamma$ -dose rate response of three fusion structural materials [8].

The effect of impurities on the radioactive decay of RAFM steels is shown in Fig. 2 which gives the surface gamma dose rate dependence on the time after shutdown. First RAFM steels like OPTIFER (70 ppm Nb) reached the remote recycling level at about 100 years after irradiation, while EUROFER and F82H

mod could be stored as low-level waste after the same period of time after reactor shut-down. The difference between the latter two alloys (hatched area) is due to the lower Nb (1 ppm) content of F82H mod compared to 10 ppm for EUROFER. In order to move into the hands-on-level domain the activation level has to be reduced by two orders of magnitude. This seems to be technically feasible; it requires increased feedstock control and production lines [9].

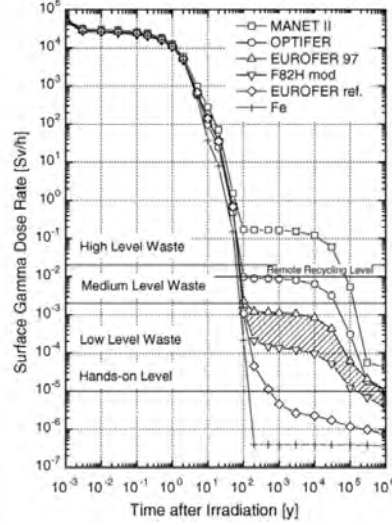


Figure 2: Calculated decay of  $\gamma$  surface dose rate in iron and ferritic-martensitic steels after irradiation ( $12.5 \text{ MW/m}^2$ ) in a first wall DEMO spectrum [9].

## 2 Fabrication and Microstructure

### 2.1 F82H Fabrication

The production of FM heats usually implies vacuum arc or induction melting, and purification through vacuum arc re-melting, to produce chemically and mechanically homogeneous ingots. Development aspects mainly focus on large-scale smelting and purification techniques. For RAFM steels in particular, there is a need to reduce neutron-induced activation and lower impurities levels. Two fabrication methods have been used for the production of large heats of F82H. The first is Hot Isostatic Pressing (HIP) for near-net-shape structures, and the second is Thermo-Mechanical-Controlled-Processing (TMCP) [10]. Because HIPPING is a solid-state bonding process, the process requires heating above temperatures that result in phase transformation and can cause coarsening of Prior-Austenite-Grains (PAG). The ASTM grain size for HIPPED F82H is 8 (17-24  $\mu\text{m}$ ), and is 3 (95-135  $\mu\text{m}$ ) for the TMCP-produced steel [10]. Tempering treatments are done for several hours in the temperature range of 1000-1100  $^{\circ}\text{C}$ . The resulting microstructure is shown in Fig. 7 [10]. To dissolve precipitates and normalize the grain size, heating above 1100  $^{\circ}\text{C}$  is required. However, because the  $\gamma$ -to- $\delta$  ferrite transformation temperature is  $>1200^{\circ}\text{C}$ , homogenization is carried out below 1200  $^{\circ}\text{C}$ . The HIPPING process is sequentially carried out as follows: HIP at  $>1100^{\circ}\text{C} \Rightarrow$  Normalize at  $< 1000^{\circ}\text{C} \Rightarrow$  Temper at 750  $^{\circ}\text{C}$  for 60 min. The heating and cooling rates are 400 K/s for typical HIPPING furnace conditions. A schematic of the manufacturing methods of RAFM and ODS steels is shown in Fig. 3 [6].

The tempering temperature has important consequences on the mechanical properties. As the temperature increases, the yield and ultimate strength decrease, while the toughness increases, as can be seen in Fig. 4. However, tempering above the AC1 (the temperature at which austenite begins to form during heating)

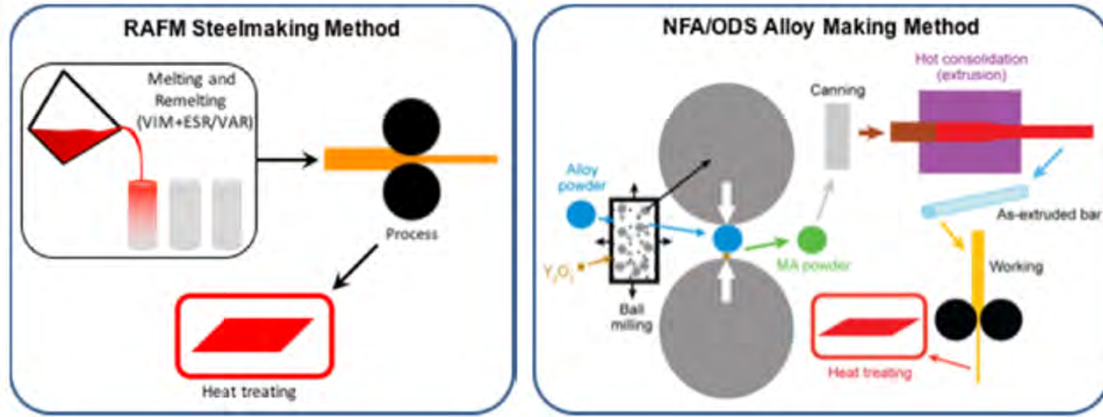


Figure 3: Manufacturing processes of RAFM and ODS steels[6].

has the opposite effects [11]. Typical resulting microstructures in low-carbon steels are shown in Figs. 5 and 6 [12].

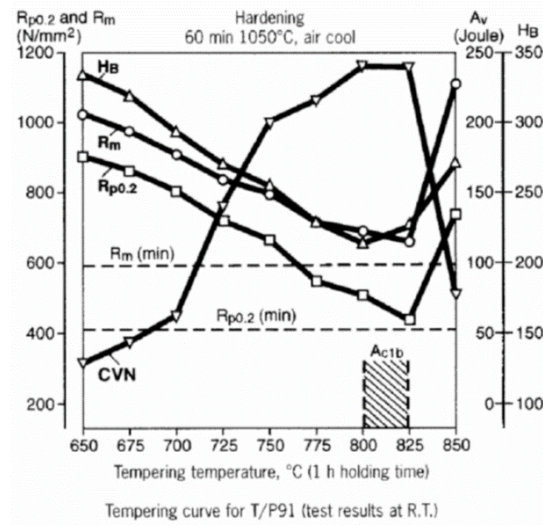


Figure 4: Effects of tempering temperature on the mechanical properties [11].

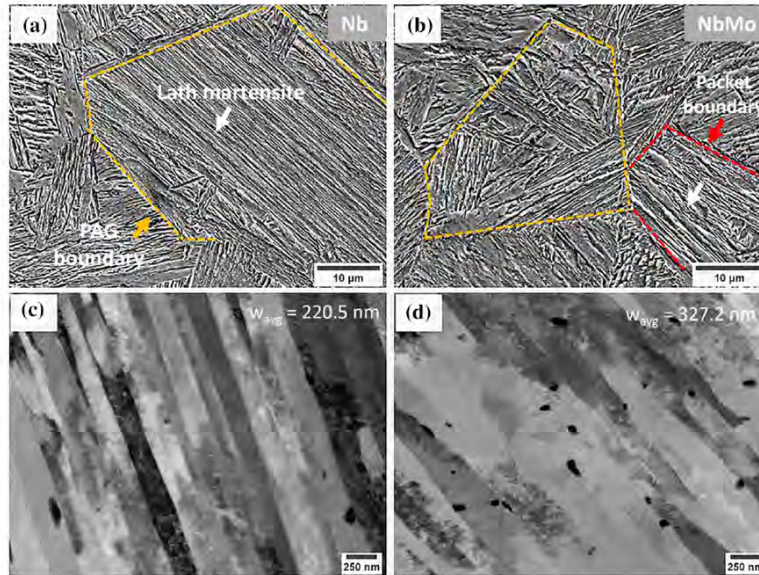


Figure 5: Typical microstructure of low-carbon steels [12].



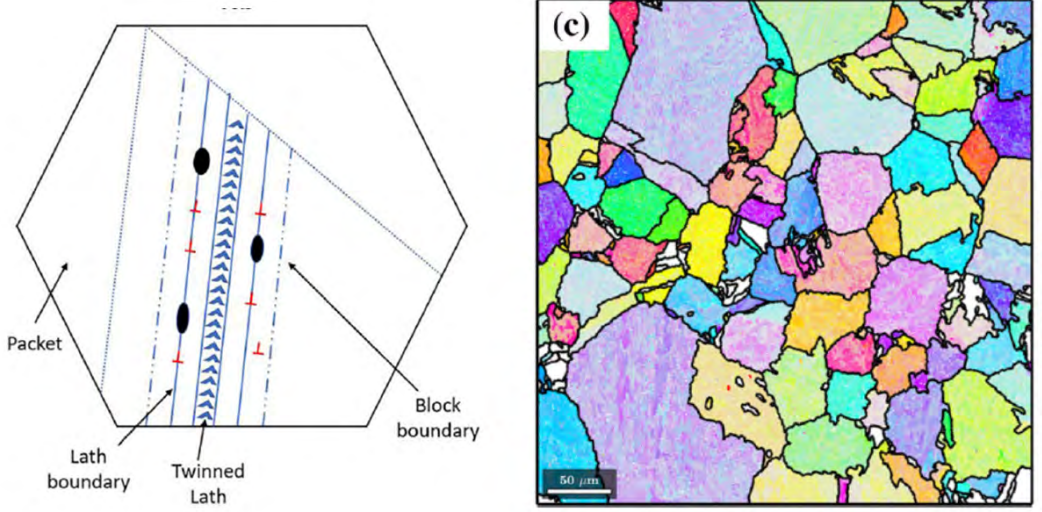


Figure 6: Schematic of a typical prior austenite grain (left) and the distribution of prior austenite grains in low-carbon steels [12].

## 2.2 F82H Microstructure

Optical micrographs after homogenizing and low-temperature normalizing are shown in Fig. 7 [10]. Higher magnification micrographs of F82H that is normalized at 1040°C for 38 min and tempered at 750 °C for 1 h, to produce a final fully tempered martensite lath structure are shown in Fig. 8. After irradiation, the defects (nano-voids and dislocation loops) accumulate, as shown in Fig. 10.

A schematic representation of the microstructure features in irradiated F82H is shown in Fig. 10.

The main microstructure components of RAFM and ODS steels are shown in Table 1, reproduced from reference [6].

Microstructure	9Cr RAFM steels	9Cr CNAs	9-20Cr NFA/ODS alloys	
Coarse particles	Size, nm	70-300 ( $M_{23}C_6$ , TaN, etc.)	70-150 ( $M_{23}C_6$ , TaN, etc.)	50-100 (TiN, $M_{23}C_6$ )
	Density, $m^{-3}$	$10^{18}$ - $10^{19}$	$10^{18}$ - $10^{19}$	$10^{18}$
	vol% (cal.)	2	0.9-1.8	$< \approx 0.1$
Fine particles	Size, nm	10-50 (MX)	3-20 (MX)	2-30 ( $Y_2O_3$ )
	Density, $m^{-3}$	$10^{19}$ - $10^{20}$	$10^{21}$ - $10^{22}$	$10^{21} - 10^{24}$
	vol% (cal.)	$< 0.2$	0.4-0.6	$< \approx 0.7 - 3$
Dislocations	Density, $m^{-3}$	$2 \times 10^{14}$	$3 \times 10^{14}$	$(0.1 - 7.8) \times 10^{14}$
Lath subgrains	Width, nm	200-500	100-500	200-500 (only in 9Cr)
Grains	Size, $\mu m$	10-60 (prior-austenite)	10-60 (prior-austenite)	0.4-2

Table 1: Comparison of microstructural components and estimated strengthening contributions at room temperature for 9Cr RAFM steels, 9Cr CNAs, and 9-20Cr NFA/ODS alloys in the as-fabricated condition [6].

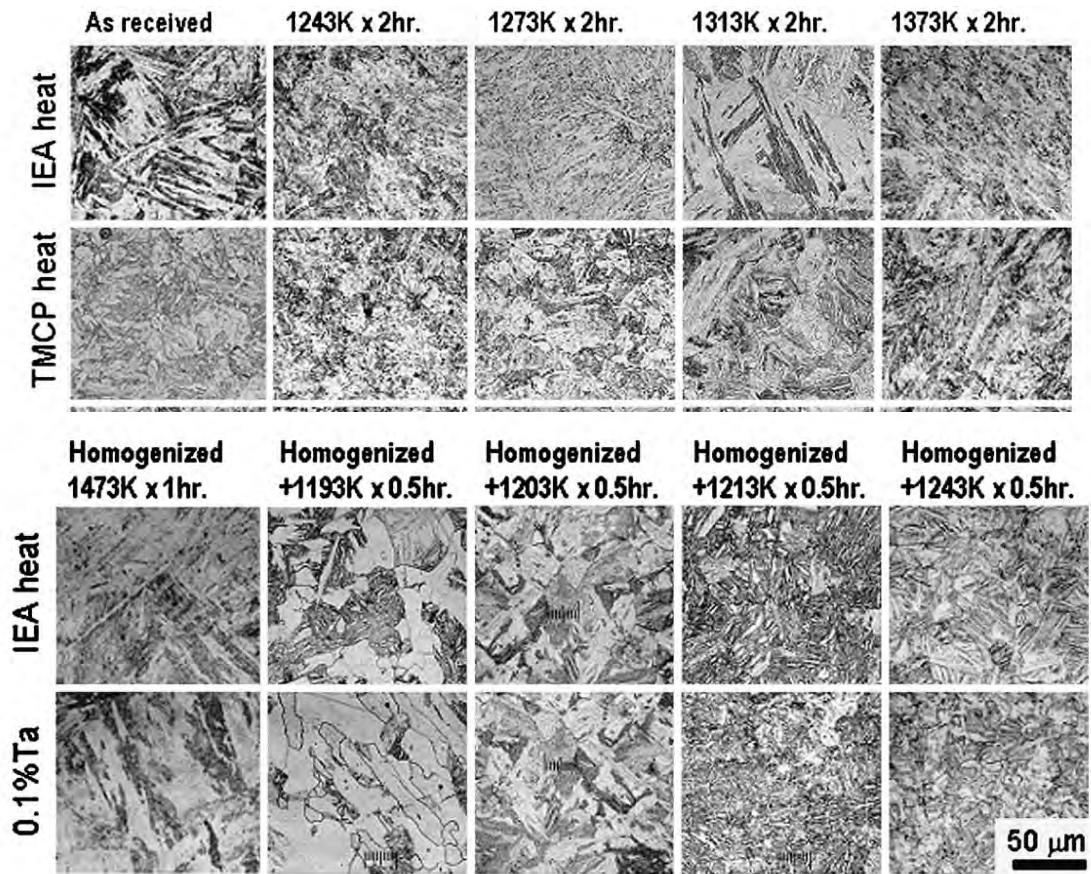


Figure 7: Optical micrographs of F82H after heat treatments [10].

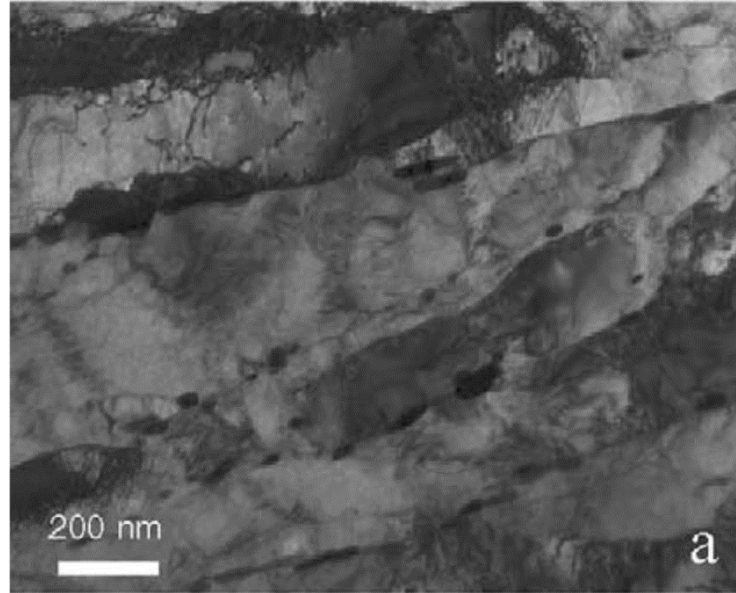
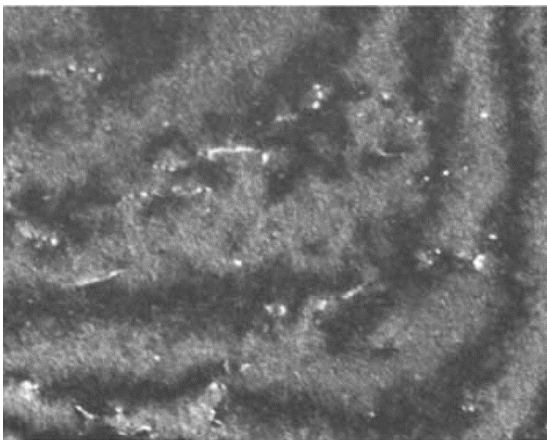
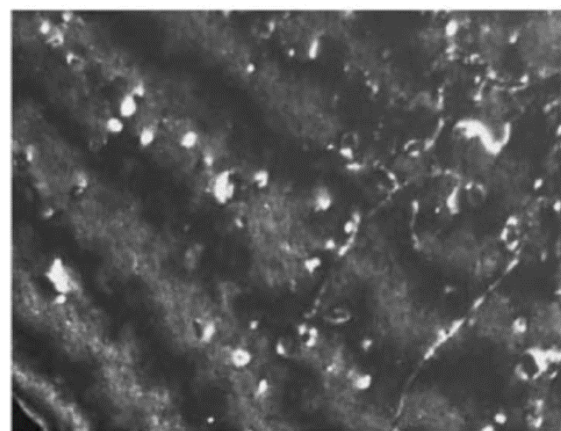


Figure 8: Higher magnification micrograph of F82H showing the martensite lath boundary [13].



(a) F82H, 3.8dpa / 110°C



(e) F82H, 9.7 dpa / 295°C

Figure 9: Optical micrographs of irradiated F82H showing dislocation loops and nano-voids[13].



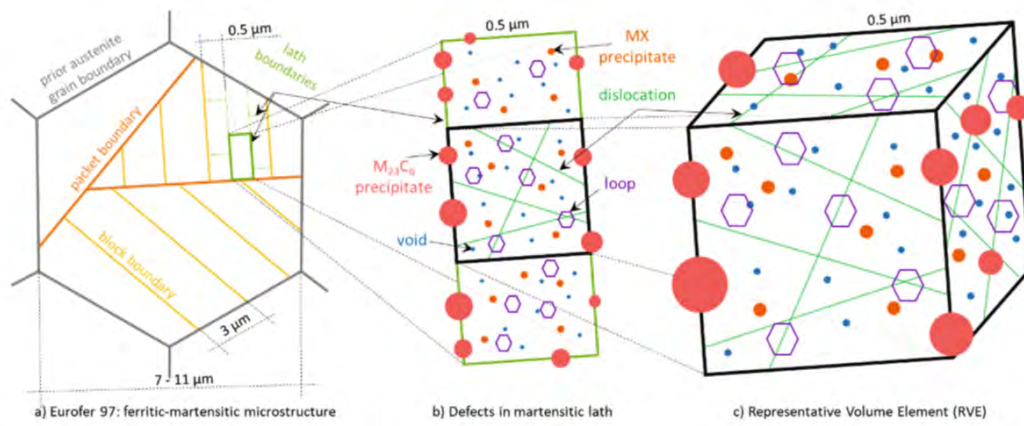


Figure 10: Schematic representation of the irradiated F82H microstructure[14].

### 3 Thermo-Physical Properties

The fundamental thermo-physical properties of F82H are shown in Table 2 below. Temperatures are in [K].

Table 2: Basic thermophysical properties of F82H [15, 16]

Parameter	Symbol	Value	Unit
Solid density at RT	$\rho$	7871	[Kg/m <sup>3</sup> ]
Specific heat at 500°C	$c_p$	630	[J/Kg.K]
Thermal conductivity (RT)	k	24	[W/(m.K)]
Thermal conductivity at 500°C	k	14.8	[W/m.K]
Thermal diffusivity at 500°C	$\alpha$	$6.5477 \times 10^{-8}$	[m <sup>2</sup> /s]
Thermal expansion (RT)	$C_{TE}$	10.4	[ $\mu\text{m}/(\text{m.K})$ ]
Electrical resistivity (RT)	$\rho_e$	$4.8931 \times 10^{-7}$	[ $\Omega.\text{m}$ ]
Young's modulus (RT)	E	220	[GPa]
Shear modulus (RT)	G	80	[GPa]
Bulk modulus (RT)	K	160	[GPa]
Poisson ratio (RT)	$\nu$	0.29	[-]

#### 3.1 Coefficient of Thermal Expansion

The temperature dependence of the coefficient of thermal expansion of F82H is given by [16]:

$$C_{TE} = 9.0955 + 4.6477 \times 10^{-3}T - 1.2141 \times 10^{-6}T^2 \quad (1)$$

where  $C_{TE}$  is in [ $10^{-6}/K$ ] and T in [K]. The temperature dependence of the CTE is displayed in Fig. (11).

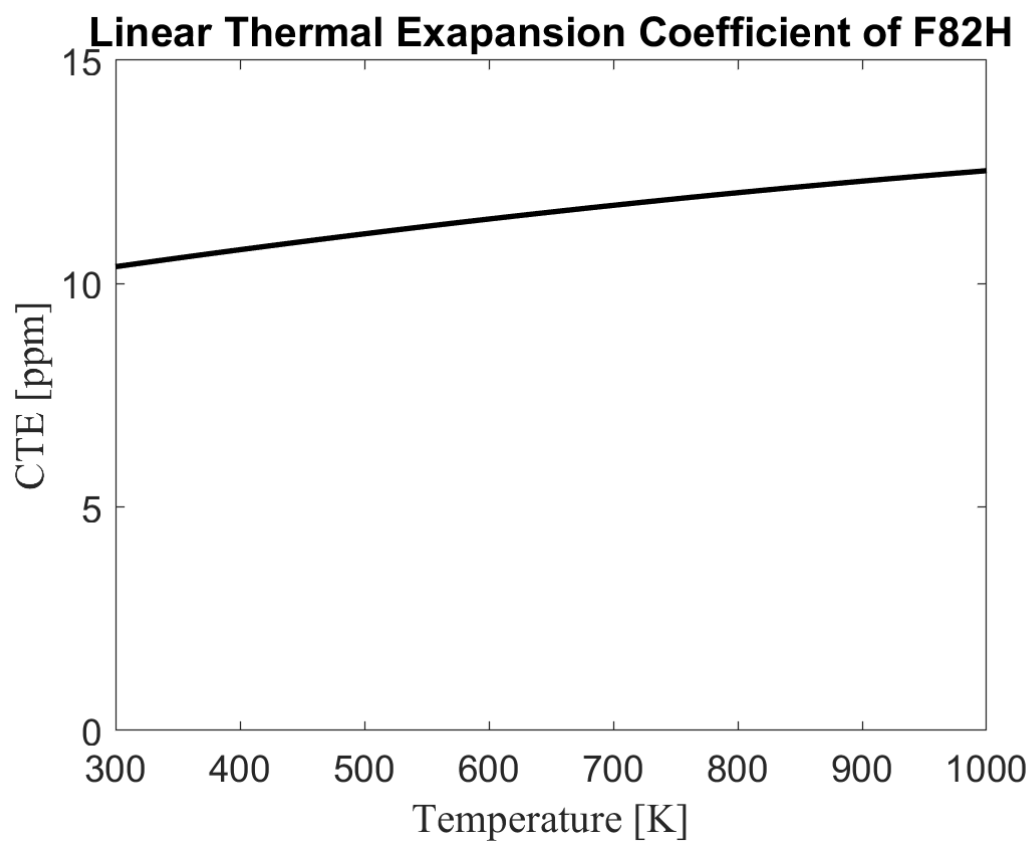


Figure 11: F82H CTE as a function of temperature [16].



### 3.2 Specific Heat

The specific heat of F82H is given by [16]:

$$C_p = 1390.2 - 7.8498T + 0.022969T^2 - 2.7446 \times 10^{-5}T^3 + 1.1932 \times 10^{-8}T^4 \quad (2)$$

and the temperature dependence is displayed in Fig. (12).

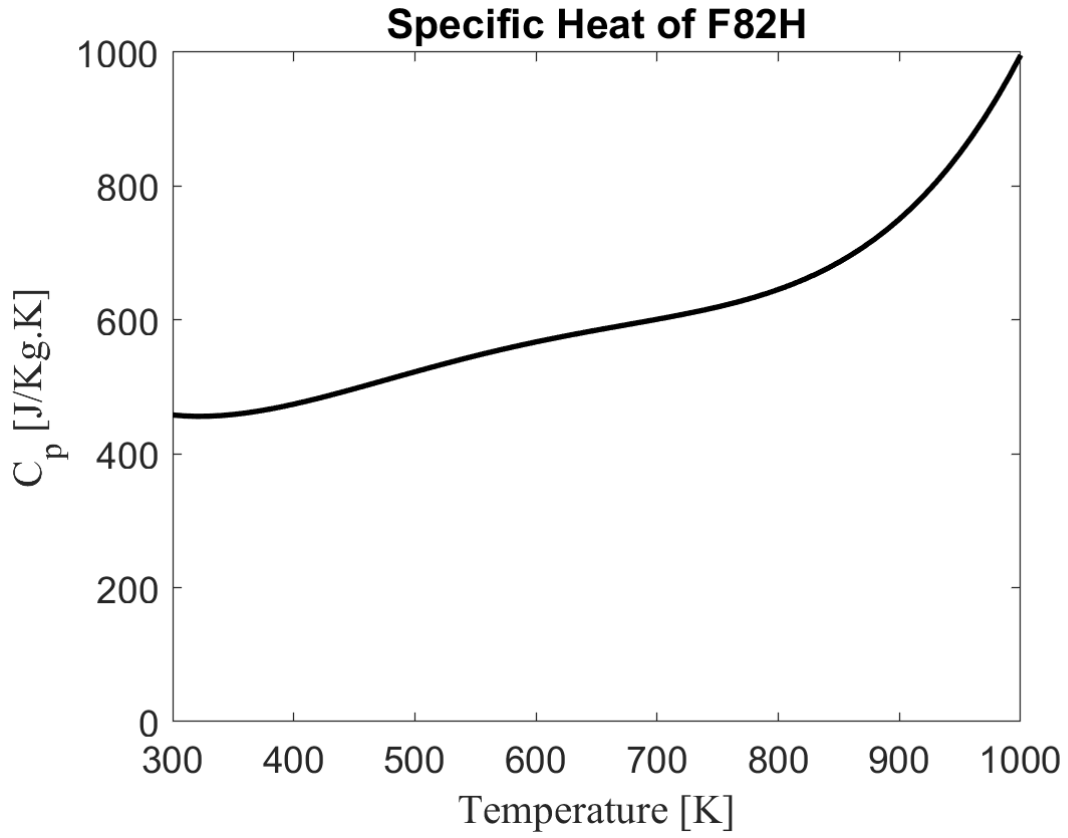


Figure 12: F82H specific heat at constant pressure as a function of temperature [16].

### 3.3 Thermal Conductivity

The thermal conductivity of F82H is given by [16]:

$$k = 28.384 - 0.011777T - 1.0632 \times 10^{-6}T^2 - 8.2935 \times 10^{-9}T^3 \quad (3)$$

and the temperature dependence is displayed in Fig. (13).

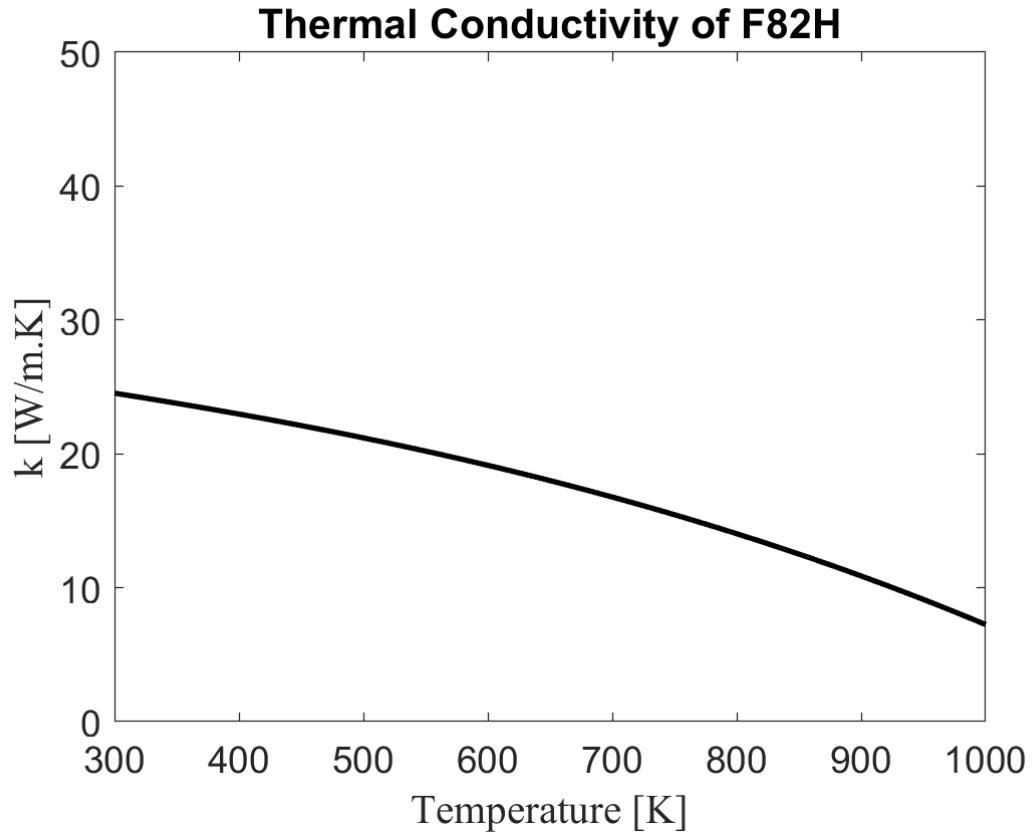


Figure 13: F82H thermal conductivity as a function of temperature [16]

### 3.4 Thermal Diffusivity

The thermal diffusivity of F82H is given by [16]:

$$\alpha = 0.089188 + 1.4051 \times 10^{-5}T - 5.7859 \times 10^{-8}T^2; \quad T[K], \alpha[mm^2/s] \quad (4)$$

and the temperature dependence is displayed in Fig. (14).

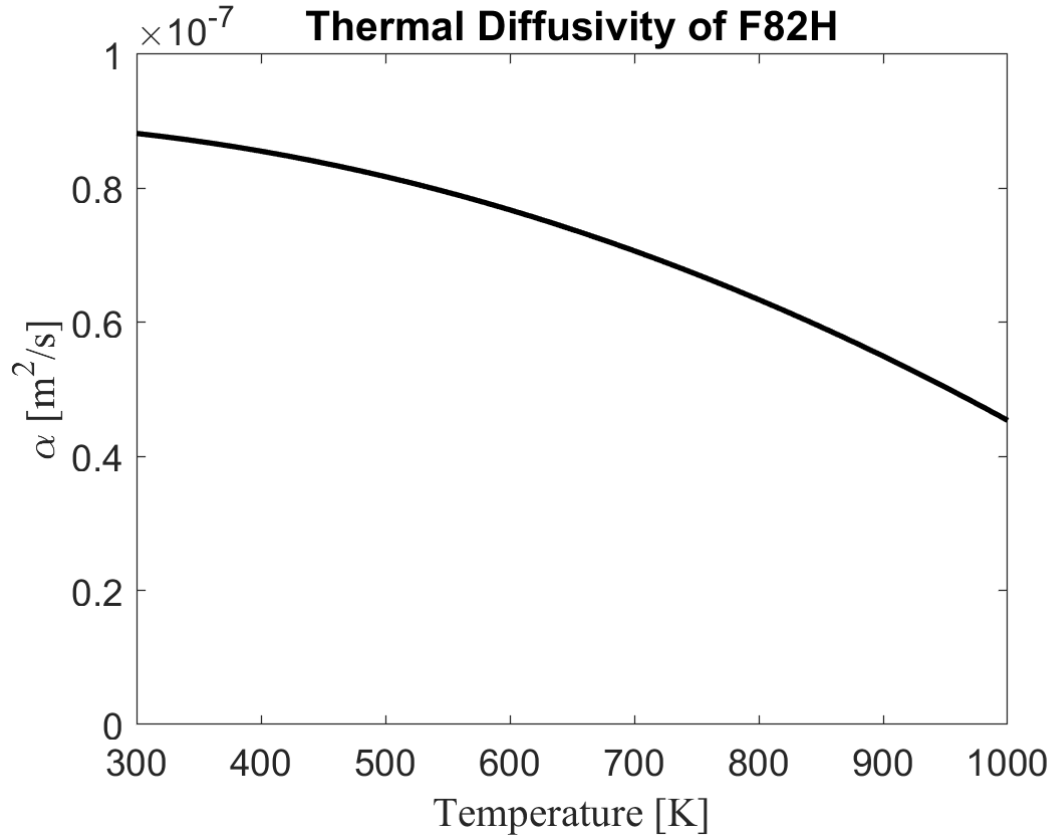


Figure 14: F82H thermal diffusivity as a function of temperature [16]



### 3.5 Electrical Resistivity

The electrical resistivity of F82H is given by [16]:

$$\rho_e = 3.289 \times 10^{-7} + 5.867 \times 10^{-10}T - 1.733 \times 10^{-13}T^2; \quad T[K], \rho_e[\Omega.m] \quad (5)$$

and the temperature dependence is displayed in Fig. (15).

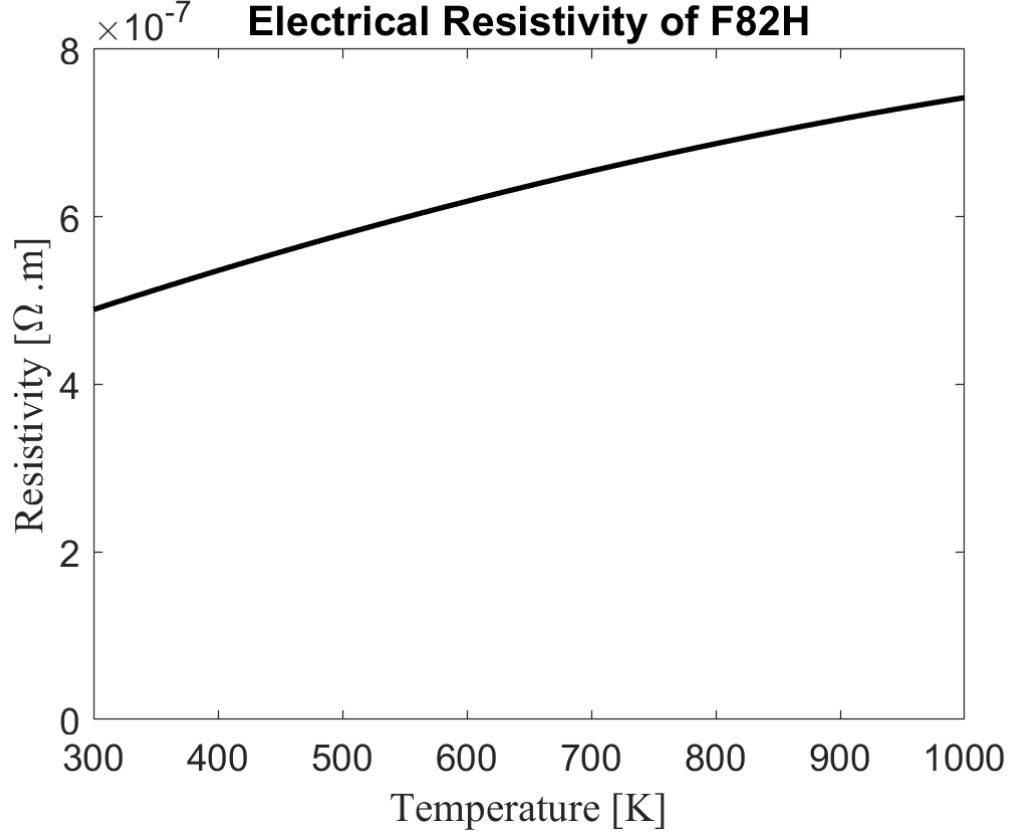


Figure 15: F82H electrical resistivity as a function of temperature [16]

### 3.6 Thermal Emissivity

Davisson and Weeks [17] used the Hagen-Rubens relation together with the Fresnel equations to calculate the total hemispherical emissivity of a metal. Their expression, as modified by Parker and Abbott, is as follows [18]:

$$\sigma = 0.766\sqrt{(T\rho_e(T))} - (0.309 - 0.0889\ln(T\rho_e(T)))(T\rho_e(T)) - 0.0175(T\rho_e(T))^{3/2}; \quad T[K], \rho_e[\Omega.cm] \quad (6)$$

The electrical resistivity, and hence the emissivity, depend on the surface roughness. The electrical resistivity ( $\Omega.cm$ ) of polished and rolled F82H are fitted to the following equations:

$$\rho_e = 4.2757 \times 10^{-5} + 7.6271 \times 10^{-8}T - 2.2529 \times 10^{-11}T^2 \quad \text{polished} \quad (7)$$

$$\rho_e = 7 \times 10^{-5} + 3.15 \times 10^{-7}T - 2.8 \times 10^{-12}T^2 \quad \text{rolled} \quad (8)$$

The temperature dependence is displayed in Fig. (16).

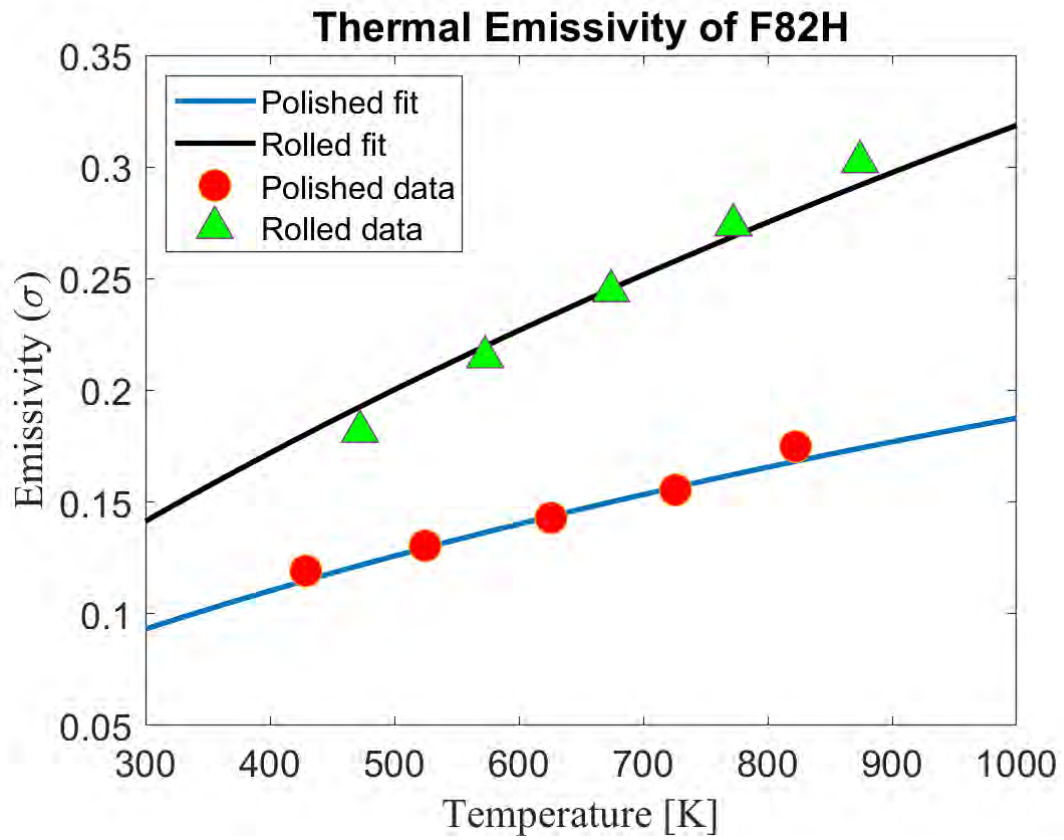


Figure 16: F82H total hemispherical emissivity as a function of temperature. The data source is reference [19]

## 4 Mechanical Properties

### 4.1 Elastic Properties

Young's (E), the shear (G) modulus, and Poisson's ratio of F82H are given by [16]:

$$E = 218.76 - 0.077834 \times (T - 273) + 1.4735 \times 10^{-4} \times (T - 273)^2 - 2.1998 \times 10^{-7} \times (T - 273)^3 \quad (9)$$

$$G = 84.902 - 0.03378 \times (T - 273) + 6.8965 \times 10^{-5} \times (T - 273)^2 - 9.828 \times 10^{-8} \times (T - 273)^3 \quad (10)$$

$$\nu = 0.28247 + 6.1902 \times 10^{-6}(T - 298) + 3.162 \times 10^{-9}T^2 \quad (11)$$

The temperature dependence of the elastic and shear moduli are displayed in Fig. (17). The temperature

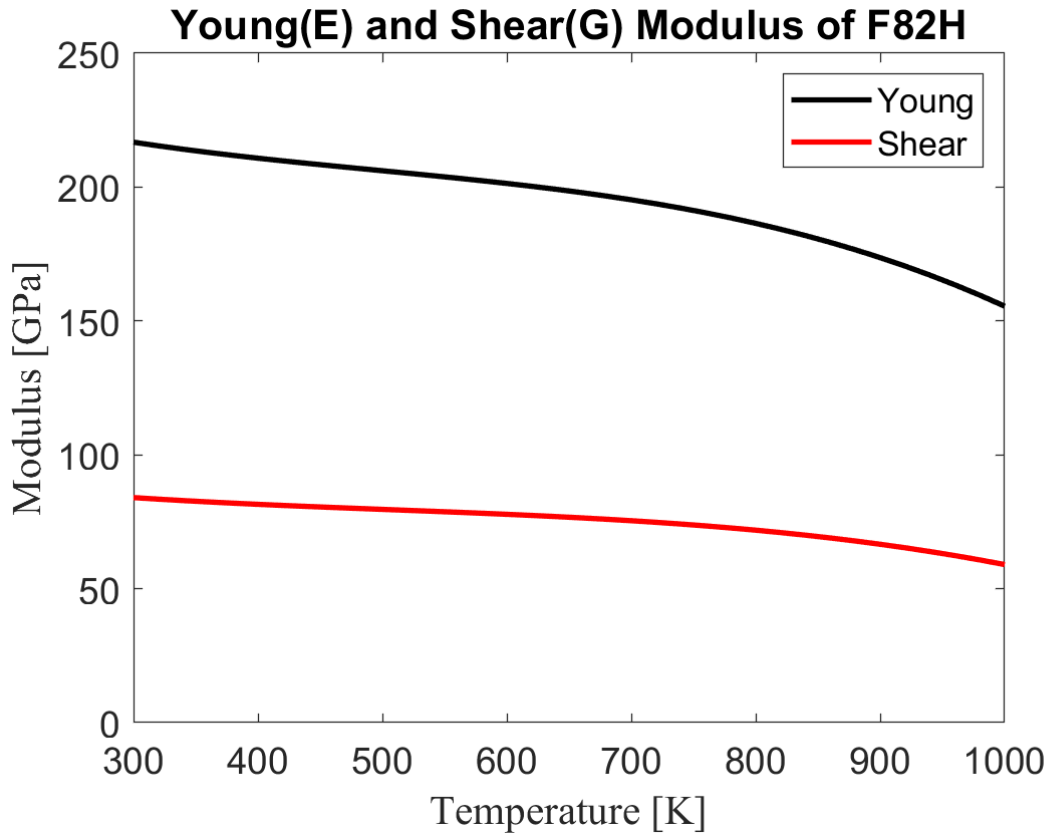


Figure 17: F82H elastic and shear moduli as a function of temperature.

dependence of Poisson's ratio is displayed in Fig. (18).



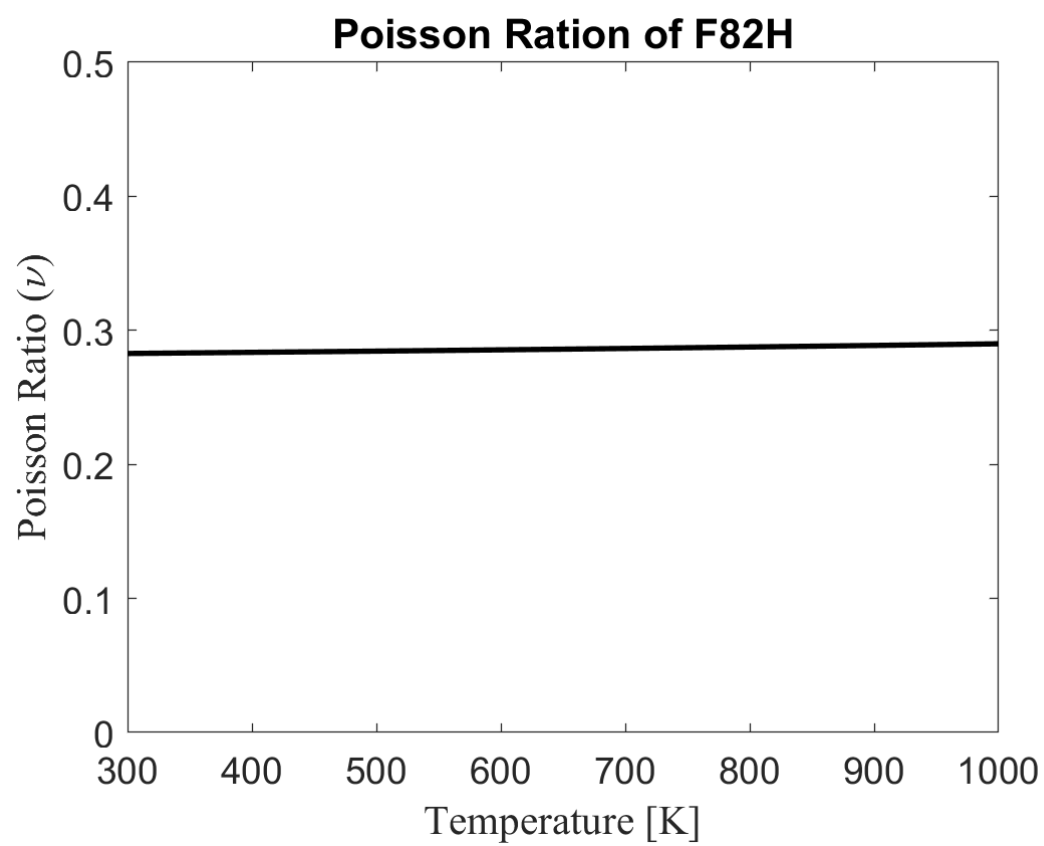


Figure 18: F82H Poisson's ratio as a function of temperature.

## 4.2 Strength

The general characteristics of the uniaxial stress-strain diagram are shown in Fig. 19.

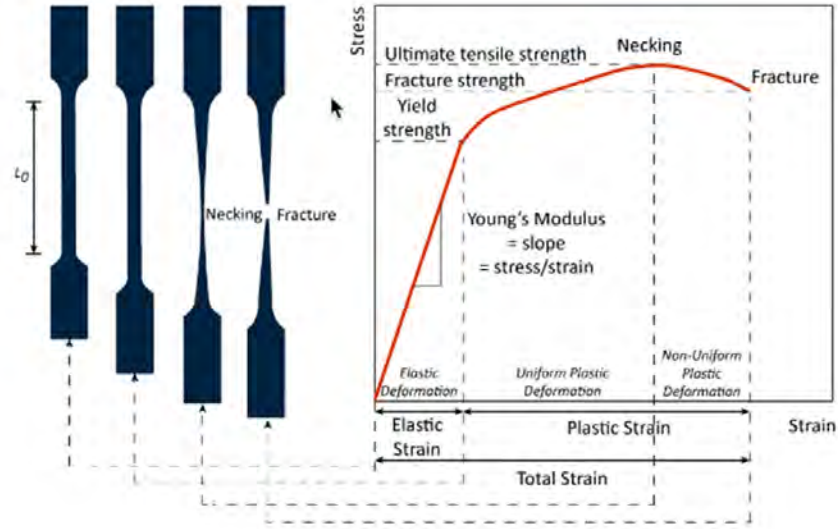


Figure 19: General characteristics of the stress-strain curve for a ductile material.

### 4.2.1 Yield Strength

The yield strength of F82H is given by [16, 20, 21]<sup>1</sup>:

```
s_fit_y =
```

```
Linear model Poly3:
s_fit_y(x) = p1*x^3 + p2*x^2 + p3*x + p4
Coefficients (with 95% confidence bounds):
p1 = -3.112e-06 (-4e-06, -2.224e-06)
p2 = 0.00496 (0.003292, 0.006628)
p3 = -2.716 (-3.695, -1.738)
p4 = 960.9 (785, 1137)
```

```
gof_y =
```

```
struct with fields:
```

```
sse: 1.5705e+04
rsquare: 0.9609
dfe: 39
adjrsquare: 0.9579
rmse: 20.0671
```

<sup>1</sup>CEA=French Alternative Energies and Atomic Energy Commission, JAERI=Japan Atomic Energy Agency, ECN=Energy Research Centre of the Netherlands, CIEMAT=The Centre for Energy, Environmental and Technological Research-Spain, FZK=Forschungs Zentrum Karlsruhe.

$$\sigma_y = 960.9 - 2.716T + 0.00496T^2 - 3.112 \times 10^{-6}T^3; \quad T[K], \sigma_y[MPa] \quad (12)$$

The "goodness of fit" parameters are as follows: *sse* is the "sum of squares error" between data and fit, "rmse" is the root mean square error defined as:  $rmse = \sqrt{MSE}$ , where *MSE* is the mean square error or the residual mean square  $rmse = sse/dfe$ , and *sse* is the sum of squares error, and *dfe* is the residual degrees of freedom, defined as the number of response values *n* minus the number of fitted coefficients *m* estimated from the response values. *rsquare* is defined as the ratio of the sum of squares of the regression (SSR) and the total sum of squares (SST). R-square can take on any value between 0 and 1, with a value closer to 1 indicating that a greater proportion of variance is accounted for by the model. Here, an R-square value of 0.9609 means that the fit explains 96.09% of the total variation in the data about the average.

The temperature dependence is displayed in Fig. (20).

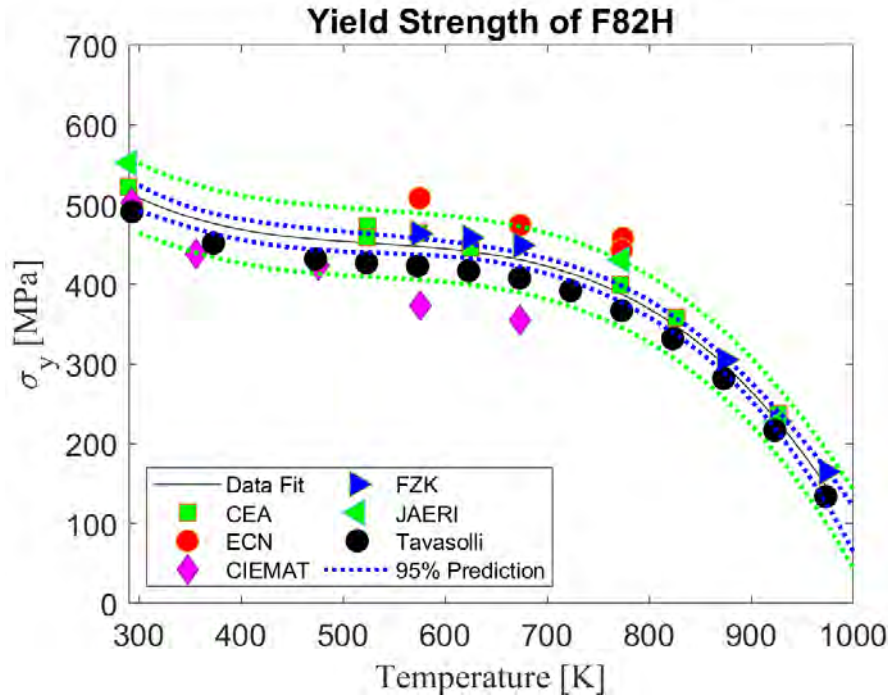


Figure 20: Yield strength of F82H [16, 20, 21].

#### 4.2.2 Ultimate Strength

The ultimate strength of F82H is given by [16, 20, 21]<sup>2</sup>:

```
s_fit_u =  
  
Linear model Poly3:  
s_fit_u(x) = p1*x^3 + p2*x^2 + p3*x + p4  
Coefficients (with 95% confidence bounds):  
p1 = -2.575e-06 (-3.372e-06, -1.778e-06)  
p2 = 0.004087 (0.002572, 0.005603)  
p3 = -2.468 (-3.368, -1.568)  
p4 = 1065 (902.2, 1228)  
  
gof_u =  
  
struct with fields:  
  
sse: 1.3068e+04  
rsquare: 0.9803  
dfe: 38  
adjrsquare: 0.9788  
rmse: 18.5443
```

$$\sigma_u = 1065 - 2.468T + 0.004087T^2 - 2.575 \times 10^{-6}T^3; \quad T[K], \sigma_u[MPa] \quad (13)$$

and the temperature dependence is displayed in Fig. (21).

---

<sup>2</sup>sse=The sum of squares due to error, rsquare=R-squared (coefficient of determination),dfe=Degrees of freedom in the error,adjrsquare=Degree-of-freedom adjusted coefficient of determination,rmse=Root mean squared error (standard error)

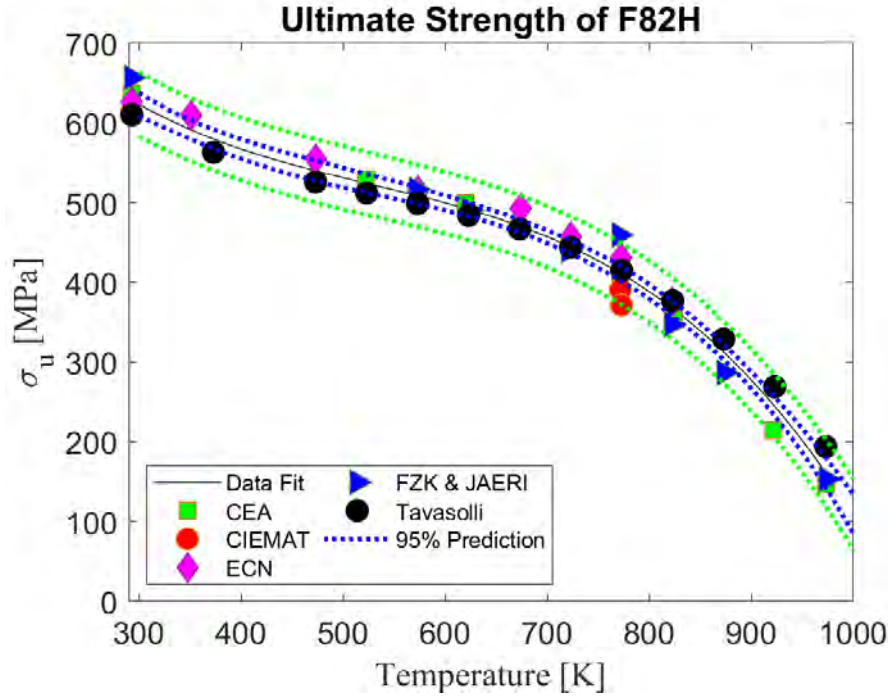


Figure 21: Ultimate strength of F82H [16, 20, 21].

### 4.3 Ductility

#### 4.3.1 Uniform Elongation

e\_fit\_u =

```
Linear model Poly3:
e_fit_u(x) = p1*x^3 + p2*x^2 + p3*x + p4
Coefficients (with 95% confidence bounds):
p1 = 1.282e-08 (-8.372e-09, 3.402e-08)
p2 = -1.649e-05 (-5.579e-05, 2.282e-05)
p3 = -0.002602 (-0.02521, 0.02001)
p4 = 7.393 (3.471, 11.32)
```

gof\_u =

struct with fields:

```
sse: 4.3319
rsquare: 0.9509
dfe: 30
adjrsquare: 0.9460
rmse: 0.3800
```

$$\varepsilon_u = 7.393 - 0.002602T - 1.649 \times 10^{-5}T^2 + 1.282 \times 10^{-8}T^3; \quad T[K], \varepsilon_u[ \quad (14)$$

and the temperature dependence is displayed in Fig. (22).



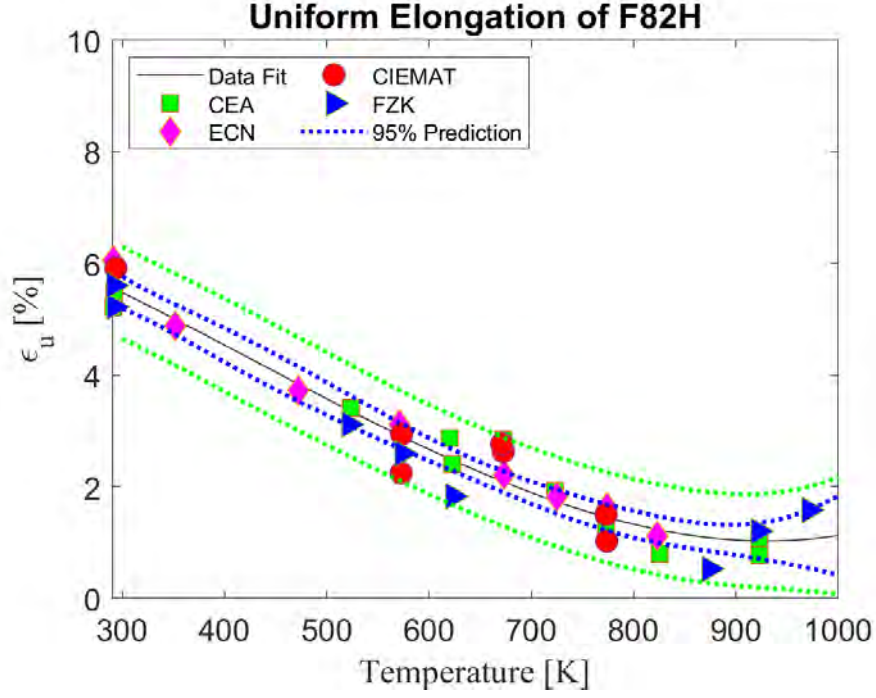


Figure 22: Uniform elongation (%) of F82H [16, 20, 21].

#### 4.3.2 Total Elongation

e\_fit\_tot =

Linear model Poly3:

e\_fit\_tot(x) = p1\*x^3 + p2\*x^2 + p3\*x + p4

Coefficients (with 95% confidence bounds):

p1 = -1.082e-07 (-3.167e-07, 1.004e-07)

p2 = 0.0003032 (-8.296e-05, 0.0006894)

p3 = -0.2306 (-0.4528, -0.008505)

p4 = 62.09 (23.83, 100.3)

gof\_tot =

struct with fields:

sse: 502.9577

rsquare: 0.5675

dfe: 33

adjrsquare: 0.5282

rmse: 3.9040

$$\varepsilon_{tot} = 62.09 - 0.2306T + 0.0003032T^2 - 1.082 \times 10^{-7}T^3; \quad T[K], \varepsilon_{tot}[\%] \quad (15)$$

and the temperature dependence is displayed in Fig. (23).

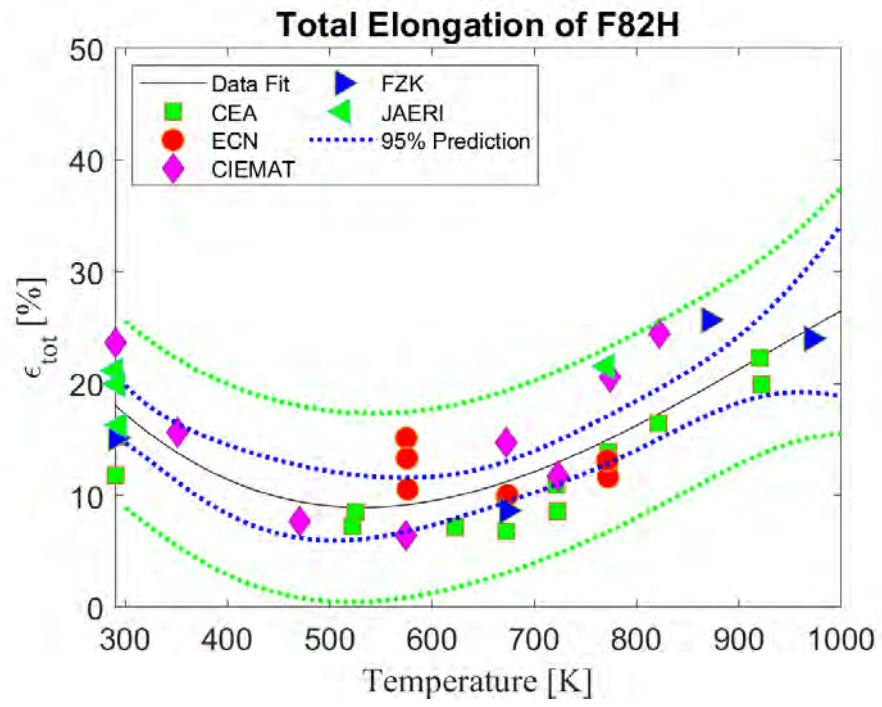


Figure 23: Total elongation of F82H [16, 20, 21].

#### 4.4 Stress-Strain Relationship

The stress-strain diagram of F82H at various temperatures is displayed in Figs. (24) and (25).

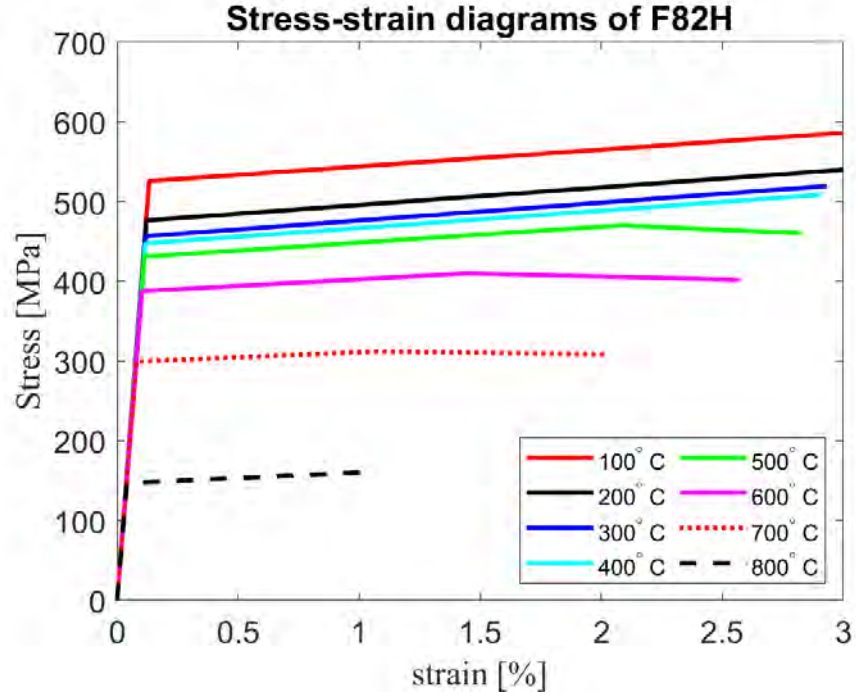


Figure 24: Simplified stress-strain diagrams of F82H at various temperatures for small strain.

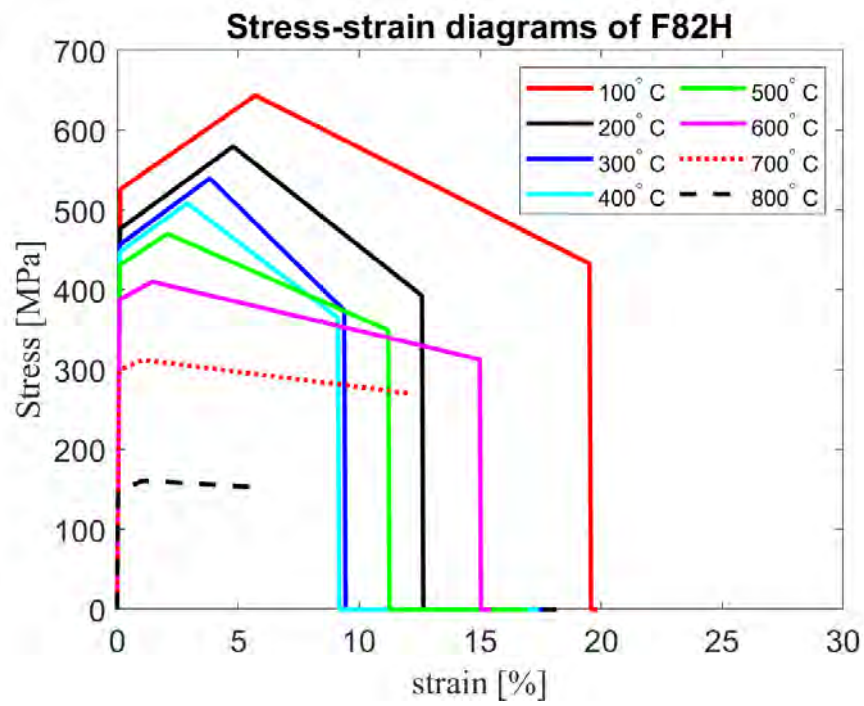


Figure 25: Simplified stress-strain diagrams of F82H at various temperatures.

## 4.5 Creep Properties

### 4.5.1 Deformation Mechanisms

We now discuss the deformation mechanisms and their relationship to material and operational variables, following the deformation map approach first proposed by Ashby [22], and then systematically adopted by Frost [23]. Deformation mechanism maps identify dominant deformation mechanisms by comparing their strain rates, which are modeled as functions of material and operational variables. In particular, we study the gen-II fusion grade F/M steel F82H and consider four types of deformation mechanisms and their relationship to two operational variables, namely the normalized tensile stress  $\sigma/\mu_0$  and homologous temperature  $T/T_m$  (where  $\mu_0$  is the shear modulus at 300°K and  $T_m$  is the melting temperature). In all our calculations we employ a piecewise<sup>3</sup> linear dependence of the shear modulus  $\mu$  on temperature, which was obtained fitting experimental data from [24]. Other material parameters for F82H are listed in Table 3. The four deformation mechanisms are:

Parameter	Description	$\alpha/\delta$	$\gamma$
$b$	Burgers vector [m]	$0.248 \cdot 10^{-9}$	$0.258 \cdot 10^{-9}$
$\Omega$	atomic volume [m <sup>3</sup> ]	$1.18 \cdot 10^{-29}$	$1.21 \cdot 10^{-29}$
$A$	Dorn constant [-]	$7 \cdot 10^{13}$	$4.3 \cdot 10^5$
$n$	power law creep exponent [-]	6.9	4.5
$D_{0v}$	bulk diffusion coefficient [m <sup>2</sup> /s]	$1 \cdot 10^{-4}$	$1 \cdot 10^{-5}$
$Q_{0v}$	activation energy for bulk diffusion [J/mol]	$240 \cdot 10^3$	$270 \cdot 10^3$
$\dot{\epsilon}_0$	prefactor for dislocation glide [s <sup>-1</sup> ]	$10^6$	-
$\mu_0$	shear modulus at 300°K [Pa]	$84 \cdot 10^9$	-
$V$	activation volume [m <sup>3</sup> ]	$100b^3$	-
$\tau_f$	flow stress [Pa]	$320 \cdot 10^6$	-
$\tau_0$	athermal part of $\tau_f$ [Pa]	$170 \cdot 10^6$	-
$d$	average grain size [m]	$22 \cdot 10^{-6}$	-
$D_{0B}$	grain boundary diff. coefficient [m <sup>2</sup> /s]	$1 \cdot 10^{-4}$	-
$Q_{0B}$	activation energy for g.b. diffusion [J/mol]	$150 \cdot 10^3$	-
$\delta$	g.b. cross section for diffusion transport [m]	$2b$	-

Table 3: Material parameters for F82H in SI units. A distinction between the bcc phase ( $\alpha$  or  $\delta$  iron) and fcc phase ( $\gamma$  iron) is made when appropriate. Data from [22, 23].

1. *Crystal instability.* Crystals exhibit a theoretical shear strength corresponding to the shear stress required to shift planes of atoms with respect to neighboring planes in the absence of material defects. Above the theoretical shear strength, which can be taken as  $\mu/20$ , the crystal structure becomes unstable and immediate plastic collapse takes place. Therefore, the strain rate  $\dot{\epsilon}_1$  associated with crystal instability can be expressed as:

$$\dot{\epsilon}_1 = \begin{cases} \infty & \frac{\sigma}{\mu} \geq \frac{1}{20} \\ 0 & \frac{\sigma}{\mu} < \frac{1}{20} \end{cases} \quad (16)$$

<sup>3</sup>A piecewise function was used to account for the change in the slope  $\frac{d\mu}{dT}$  corresponding to the martensite annealing temperature.



2. *Plastic flow by dislocation glide.* The plastic strain rate due to dislocation glide is controlled by the flow stress  $\tau_f$ , which includes a contribution due to obstacles and, in body centered cubic (bcc) materials, a contribution arising from the lattice resistance. Since in heavily alloyed steels, such as F82H, the obstacle resistance is the dominant the rate-controlling mechanism, the strain rate for dislocation glide can be expressed as [22]:

$$\dot{\epsilon}_2 = \begin{cases} \dot{\epsilon}_0 \exp\left(-\frac{V(\tau_f - \sigma)}{kT}\right) & \sigma \geq \tau_0 \\ 0 & \sigma < \tau_0 \end{cases} \quad (17)$$

In Eq. (17),  $\dot{\epsilon}_0$  is a pre-exponential factor,  $V$  is the activation volume for dislocation glide and  $\tau_0$  is the athermal part of the flow stress.

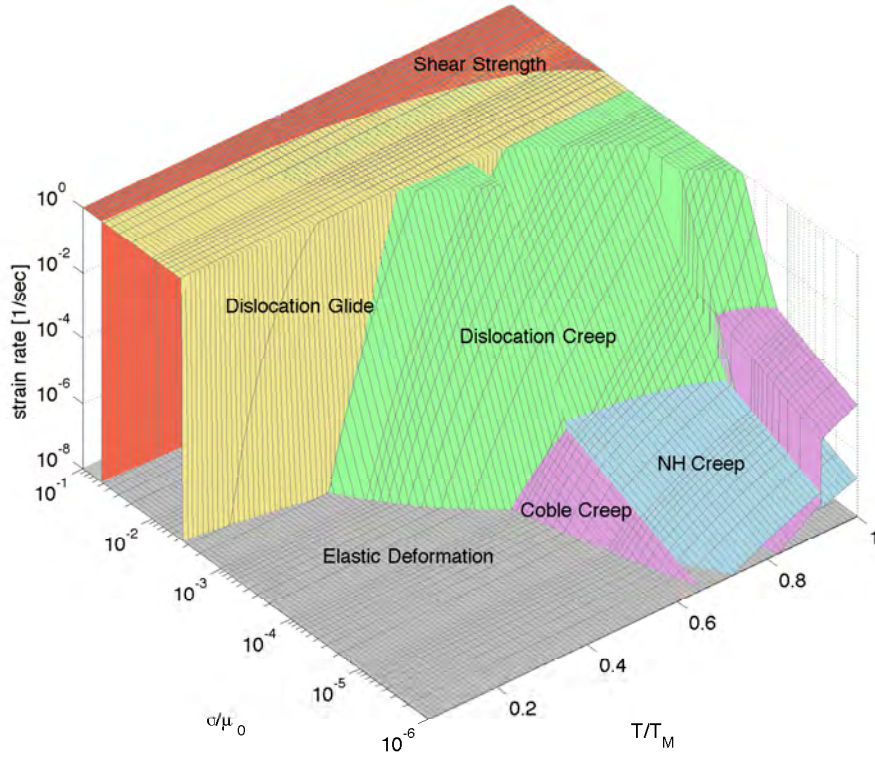


Figure 26: Deformation mechanism map for F82H. Strain rate surfaces corresponding to the described mechanisms are plotted as a function of normalized tensile stress  $\sigma/\mu_0$  and homologous temperature  $T/T_m$ , in the range  $10^{-8} \leq \dot{\epsilon} \leq 10^0$  [ $s^{-1}$ ]. The highest strain rate determines the dominant deformation mechanism.

3. *Diffusional creep:* At sufficiently high temperatures, diffusion becomes the main mechanism of material transport. Following [22], we distinguish between two regimes, dominated by bulk diffusion (Nabarro-Herring creep, NH creep henceforth) and grain boundary diffusion (Coble creep), respectively. The strain rate for NH creep is given by:

$$\dot{\epsilon}_3 = 14 \frac{\sigma \Omega}{k_b T} \frac{1}{d^2} D_v \quad D_v = D_{0v} \exp\left(-\frac{Q_v}{RT}\right) \quad (18)$$

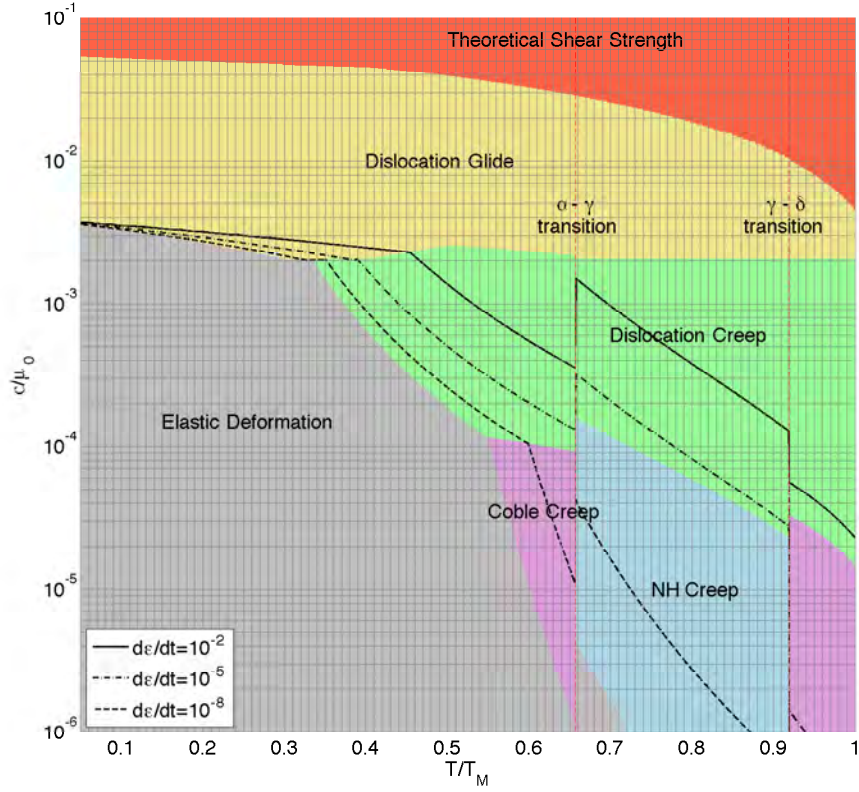


Figure 27: Dominant deformation modes experienced by power plant components during different operational conditions: normal operations ( $\dot{\epsilon} \approx 10^{-8}\text{s}^{-1}$ ), startup/shutdown transient operations ( $\dot{\epsilon} \approx 10^{-5}\text{s}^{-1}$ ), off-normal conditions ( $\dot{\epsilon} \approx 10^{-2}\text{s}^{-1}$ ).

where  $\Omega$  is the atomic volume,  $d$  the average grain size and the bulk diffusion coefficient  $D_v$  depends on the pre-exponential factor  $D_{0v}$  and on the activation energy  $Q_{0v}$ . Similarly, for Coble creep we have:

$$\dot{\epsilon}_4 = 14 \frac{\sigma \Omega}{k_b T} \frac{1}{d^2} \frac{\pi \delta}{d} D_B \quad D_B = D_{0B} \exp \left( -\frac{Q_B}{RT} \right) \quad (19)$$

with  $\delta$  being the grain boundary cross-section for diffusional transport. The overall strain rate due to diffusional creep is  $\dot{\epsilon}_3 + \dot{\epsilon}_4$ .

4. *Dislocation creep.* At high temperatures (typically defined as  $T > T_m/2$ ), the deformation mode is controlled by the formation and subsequent evolution of dislocation cell structures within each grain. The dislocation cell size is inversely proportional to the applied stress, and climb-controlled recovery of dislocations takes place within the cell walls. The rate of recovery is dictated by point defect diffusion, while the accumulation of plastic strain is governed by a dislocation glide in between cell walls. Thus, it is expected that the deformation is diffusion-controlled with a non-linear stress dependence as a result of dislocation glide. The appropriate constitutive equation is given by [25]:

$$\dot{\epsilon}_5 = A \frac{D_v \mu b}{kT} \left( \frac{\sigma}{\mu} \right)^n \quad (20)$$

where  $A$  and  $n$  are material parameters listed in table 3.

The constitutive equations for strain rates are plotted in Fig 26 as a function of normalized tensile stress and homologous temperature, in the range  $10^{-6} \leq \sigma/\mu_0 \leq 10^{-1}$  and  $0.05 \leq T/T_m \leq 1$ , respectively. Plastic strain rates lower than  $10^{-8} \text{ s}^{-1}$  are considered negligible and the corresponding area in the map is associated with elastic deformation. Fig. 27 illustrates what deformation mechanisms are encountered in power-plant components during different typical operational conditions (associated with global strain rates).

#### 4.5.2 Creep Strain Rate for HT-9

To fit the creep strain as a function of time ( $t$ ), temperature ( $T$ ), and stress ( $\sigma$ ), we utilize available HT9 data in a procedure similar to reference [26]. The present fitting procedure is more accurate than [26], and is summarized as follows.

First, define the functions:

$$F_1 = 0.5 - 2600/T \quad (21)$$

$$F_2 = 1 + 50/T \quad (22)$$

$$F_3 = -5.7 - 5562.28/T \quad (23)$$

$$m = 2 \times 10^{-6} \quad (24)$$

$$\sigma_0 = 0.025\sigma + 0.0055\sigma^2 \quad (25)$$

$$\dot{\epsilon}_p = 10^{(F_1 + F_2 \log(\sigma))} \quad (26)$$

$$\dot{\epsilon}_s = 10^{(F_3 + 2.5 \log(\sigma - \sigma_0))} \quad (27)$$

$$\epsilon = \epsilon_p(1 - \exp(-mt)) + \dot{\epsilon}_s t; \quad (28)$$

The results of this fitting procedure in the low-stress range are shown in Figure 28.

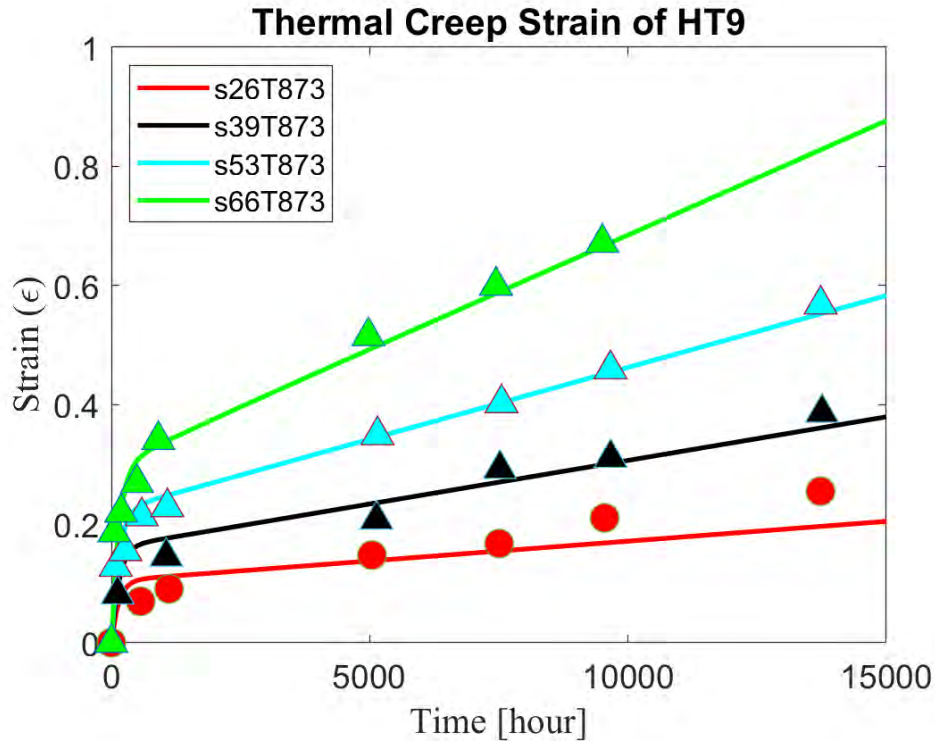


Figure 28: Comparison between measured and fitted creep strains for HT9 at  $T=873K$  in the low-stress range.

#### 4.5.3 Creep Strain Rate for T91

We develop here a process for fitting the creep strain data of steels in the three creep regimes (primary, secondary, and tertiary). The process is motivated by a geometric construction of equations from the three regimes based on expressing the creep strain data as a function of time on a log-log plot, similar to fatigue data or the Monkman-Grant relationship. Figure 29 shows a schematic of the creep strain diagram, where the strain rates in the three regimes are represented by linear relationships on the log-log plot. The linear equations have "anchor points" that can be fitted to simple functions of the stress and temperature. Once these anchor points are determined from a sufficient data set, the transient creep curve can be described at any combination of temperature and stress. The representation should be good for design and analysis within the range of the database, with some risk of extrapolation outside this range.

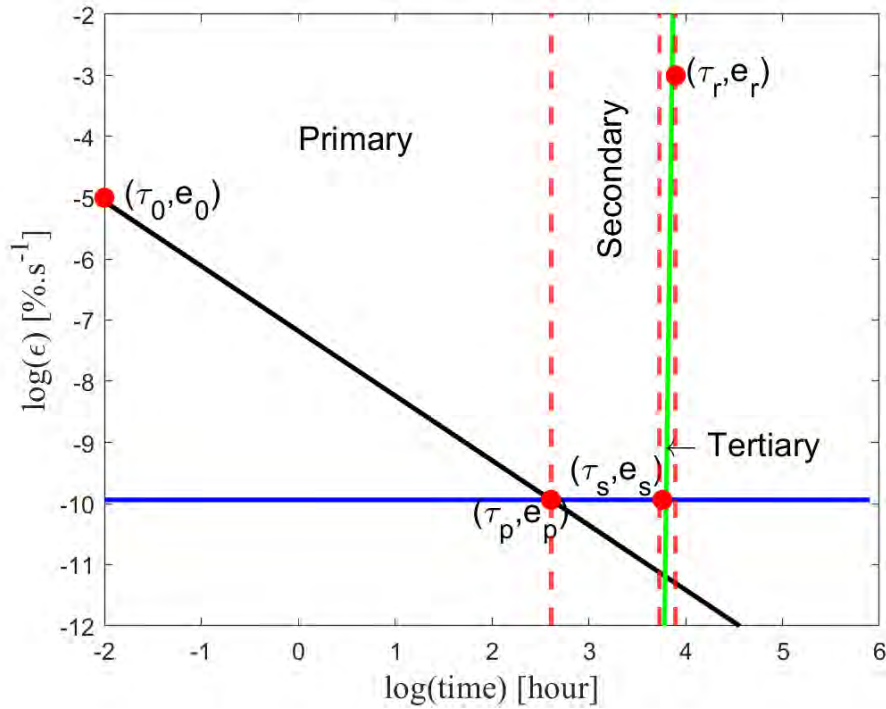


Figure 29: Schematic representation of the *three-line* model for creep strain rate

To determine the parameters in the three linear relationships, we need four anchor points. These will have the subscripts (0, p, s, and r), for reference, end of primary stage, and of secondary stage, and rupture, respectively. Also, we use  $\tau = \log 10(t)$  and  $e = \log 10(\dot{\epsilon})$  as the independent and dependent variables, respectively. The coordinates of the four "anchor points" are as follows:

1. The reference point:  $\tau_0 = \log 10(t_0)$  and  $e_0 = \log 10(\dot{\epsilon}_0)$ .
2. The end of the primary creep stage:  $\tau_p = \log 10(t_p)$  and  $e_p = \log 10(\dot{\epsilon}_p)$ .
3. The end of the secondary creep stage:  $\tau_s = \log 10(t_s)$  and  $e_s = \log 10(\dot{\epsilon}_s)$ .
4. The rupture point:  $\tau_r = \log 10(t_r)$  and  $e_r = \log 10(\dot{\epsilon}_r)$ .

The three straight-line equations are determined as follows (stresses are in MPa and temperatures in K):



1. **Primary regime:**

The "reference" point coordinates:

$$\tau_0 = -3 \quad (29)$$

$$e_0 = a_0 + b_0(\sigma - 100) + c_0(T - 873) \quad (30)$$

The "primary" point coordinates:

$$\tau_p = A_p\sigma + B_pT + C_p \quad (31)$$

$$e_p = A_s + B_s \log_{10}(\sigma) + C_sT \quad (32)$$

2. **Secondary regime:**

The "secondary" point coordinates:

$$\gamma = \gamma_0 + \gamma_1(T - 873) + \gamma_2(\sigma - 100) \quad (33)$$

$$\tau_s = \tau_r \gamma \quad (34)$$

$$e_s = e_p \quad (35)$$

3. **Tertiary regime:**

The "rupture" point coordinates:

$$\tau_r = A_r\sigma + B_rT + C_r \quad (36)$$

$$e_r = -1.6\tau_r \quad (37)$$

The model has 15 parameters, as shown in table 4.

Creep stage	Parameter	Value
Primary	$A_p$	-0.02193
	$B_p$	-0.02796
	$C_p$	28.7
	$a_0$	-4.2
	$b_0$	0.0035
	$c_0$	$10^{-6}$
Secondary	$A_s$	-68.97
	$B_s$	11.75
	$C_s$	0.04084
	$\gamma_0$	1.04
	$\gamma_1$	$4 \times 10^{-3}$
	$\gamma_2$	$2 \times 10^{-3}$
Tertiary	$A_r$	-0.021
	$B_r$	-0.0231
	$C_r$	26.1

Table 4: Creep model parameters for F/M steels at high-temperature.

The three linear equations for the creep rates are given by the following:

$$a_1 = \frac{(e_0 - e_s)}{(-3 - \tau_p)} \quad (38)$$

$$b_1 = e_0 + 3a_1 \quad (39)$$

$$a_3 = \frac{(e_r - e_s)}{(\tau_r - \tau_s)} \quad (40)$$

$$b_3 = e_r - a_3\tau_r \quad (41)$$

$$e_p(\tau) = a_1\tau + b_1 \quad (42)$$

$$e_s(\tau) = e_s = \text{const.} \quad (43)$$

$$e_t(\tau) = a_3\tau + b_3 \quad (44)$$

$$\dot{\epsilon}(\sigma, T, t) = 10^{e_p} + 10^{e_s} + 10^{e_t} \quad (45)$$

The results of this fitting procedure are shown in Figure 30 and 31 for the T91 steel at 600 °C and various applied stress, and at 100 MPa and various temperatures, respectively. The data was digitized from reference [27].

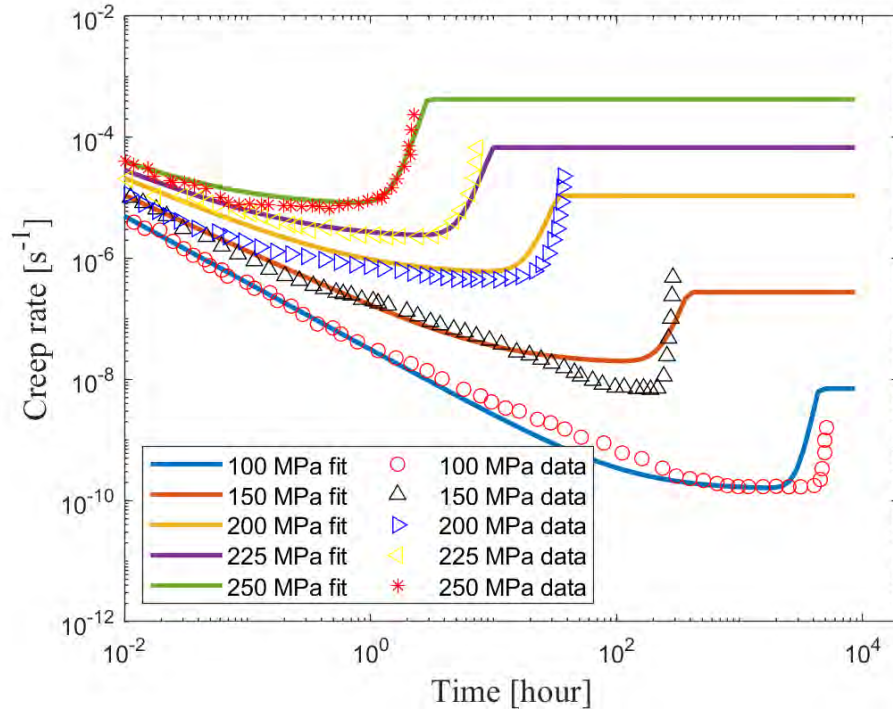


Figure 30: Model representation of creep strain data at 600 °C and various applied stress levels. Data was digitized from reference [27]

Examples of model results are shown in Figures 32 and 33.

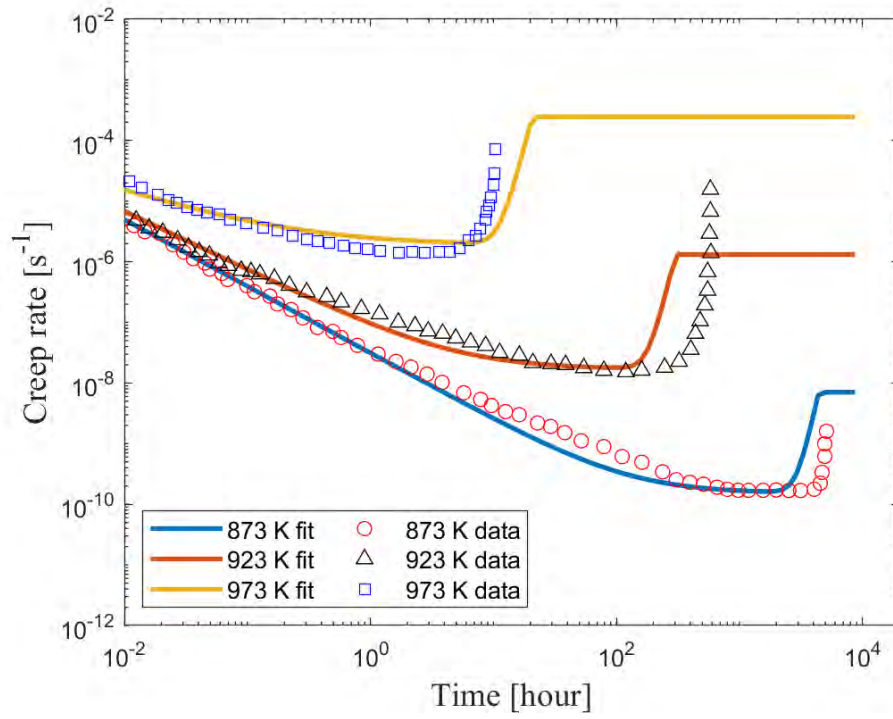


Figure 31: Model representation of creep strain data at 100 MPa and various temperatures. Data was digitized from reference [27]

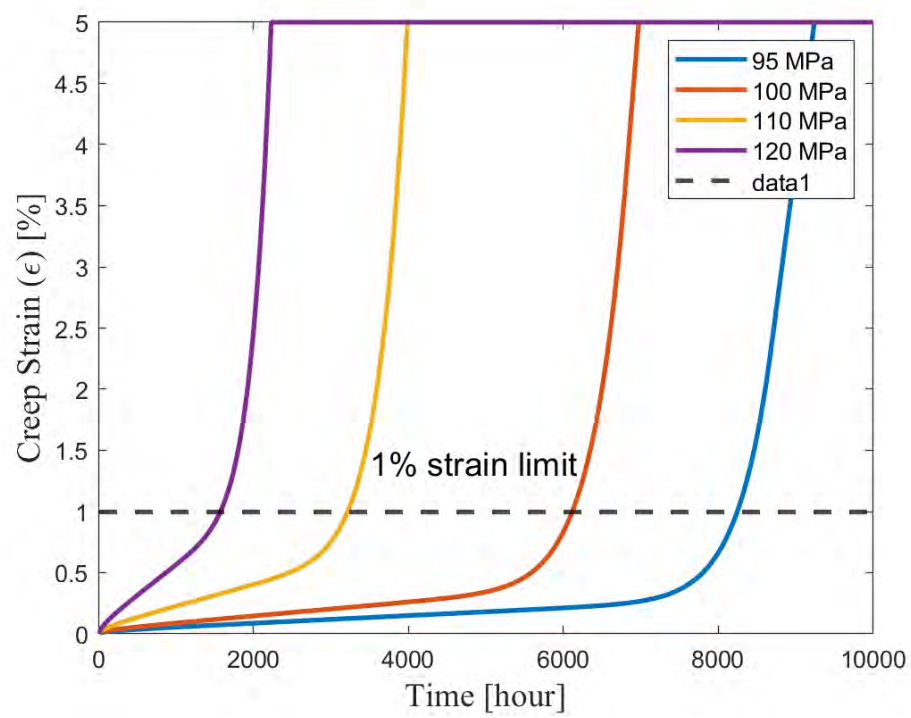


Figure 32: Model results for creep strain data at 600 °C and various applied stress levels.

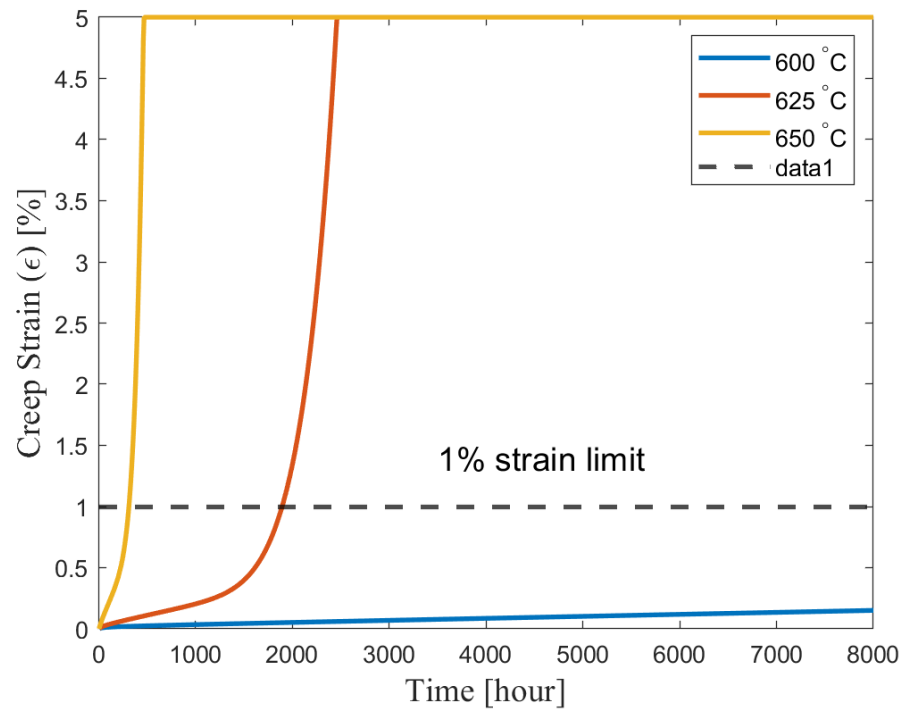


Figure 33: Model results of creep strain at 90 MPa and various temperatures.



#### 4.5.4 Creep Strain Rate for F82H

The exact set of parameters used to fit the T91 data have been used to fit the creep data of F82H [28]. The only parameter that was changed is  $\gamma_0$  from a value of 1.04 to 1.15. The results of the fit are shown in Figures 34 and 35.

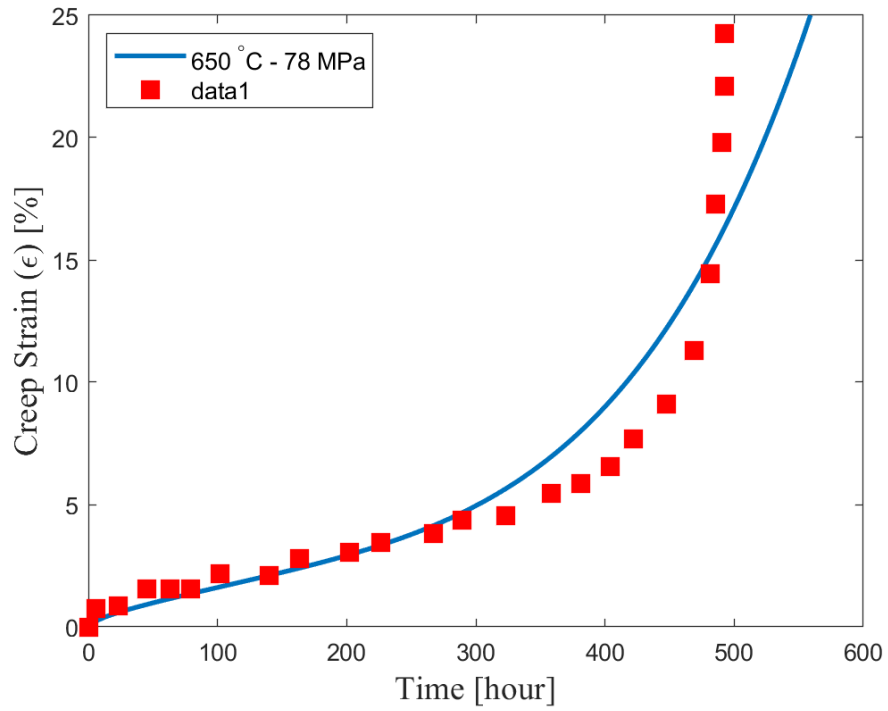


Figure 34: Model results of creep strain of F82H at 650 °C and 78 MPa. Data is digitized from reference [28]

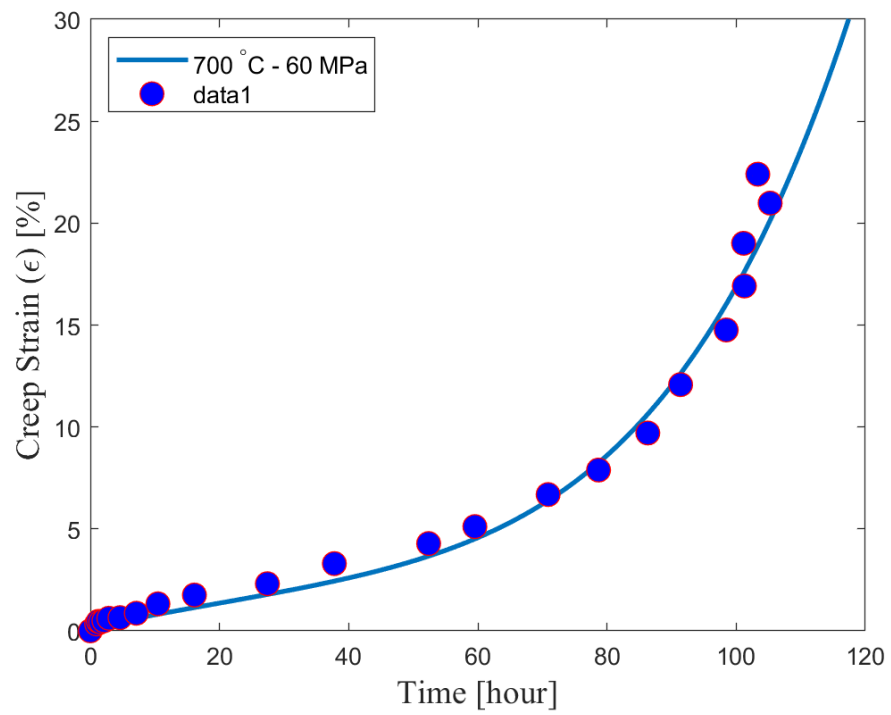


Figure 35: Model results of creep strain of F82H at 700 °C and 60 MPa. Data is digitized from reference [29]

## 4.6 Fatigue Properties

Fatigue failure is almost always initiated at a local discontinuity such as a notch or a crack. When the stress at the discontinuity exceeds the elastic limit, plastic strain occurs. If a fatigue fracture is to occur, there must exist cyclic plastic strains. Thus, the detailed elastoplastic analysis may be required for several loading cycles to determine a stable hysteresis loop, as shown in Fig. 36 [30]. Note that cyclic loading leads to stress relaxation (or hardening), yet the applied strain range ( $\varepsilon$ ) remains constant in any given test. When the applied strain range per cycle is plotted against the number of reversals (each cycle has two reversals), the resulting plot is known as the Manson-Coffin diagram and is used as a basis for low-cycle fatigue design [30].

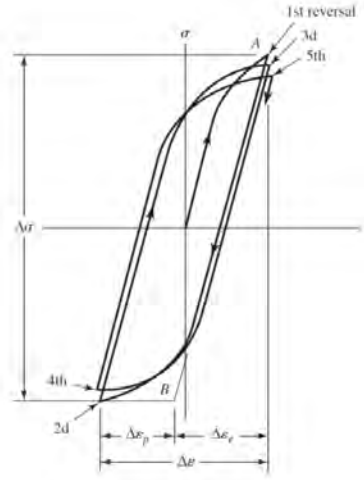


Figure 36: True stress–true strain hysteresis loops. The stress range is  $\Delta\sigma$ ,  $\Delta\varepsilon_p$  is the plastic-strain range, and  $\Delta\varepsilon_e$  is the elastic strain range. The total-strain range is  $\Delta\varepsilon_e + \Delta\varepsilon_p$  [30].

Low-cycle fatigue design relies on fitting experimental data to the power (linear on the log-log plot) relations between the total strain amplitude and the number of cycle reversals. We define the following:

- *Fatigue ductility coefficient*  $\varepsilon'_F$  is the true strain corresponding to fracture in one reversal (point A in Fig. 6–12). The plastic-strain line begins at this point in Fig. 36.
- *Fatigue strength coefficient*  $\sigma'_F$  is the true stress corresponding to fracture in one reversal (point A in Fig. 36). Note in Fig. 37 that the elastic-strain line begins at  $\sigma'_F/E$ .
- *Fatigue ductility exponent*  $c$  is the slope of the plastic-strain line in Fig. 37 and is the power to which the life  $2N$  must be raised to be proportional to the true plastic strain amplitude. If the number of stress reversals is  $2N$ , then  $N$  is the number of cycles.
- *Fatigue strength exponent*  $b$  is the slope of the elastic-strain line and is the power to which the life  $2N$  must be raised to be proportional to the true-stress amplitude

The total strain amplitude is half the total strain range

$$\frac{\Delta\varepsilon}{2} = \frac{\Delta\varepsilon_e}{2} + \frac{\Delta\varepsilon_p}{2} \quad (46)$$

The equation of the plastic-strain line in Fig. 37 is

$$\frac{\Delta\varepsilon_p}{2} = \varepsilon'_f (2N)^c \quad (47)$$

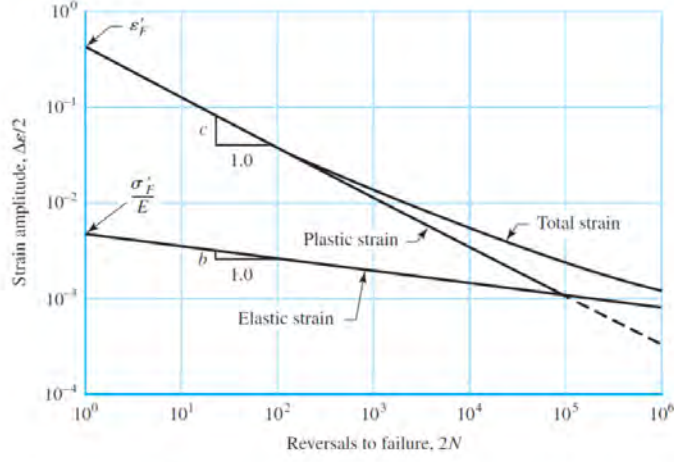


Figure 37: A log-log plot for the relationship between the fatigue life and the true-strain amplitude (The Manson-Coffin Plot) [30].

The equation of the elastic strain line is

$$\frac{\Delta \varepsilon_e}{2} = \frac{\sigma'_f}{E} (2N)^b \quad (48)$$

Therefore, we have for the total-strain amplitude

$$\frac{\Delta \varepsilon}{2} = \frac{\sigma'_f}{E} (2N)^b + \varepsilon'_f (2N)^c \quad (49)$$

which is the Manson-Coffin relationship between fatigue life and total strain. For F82H, the following equations have been used to generate the Manson-Coffin model parameters.

$$E = 4.0761 \times 10^{11} - 3.5521 \times 10^7 T - 5.87 \times 10^3 T^2 \quad (50)$$

$$\varepsilon_f = 0.01(62.09 - 0.2306T + 0.0003032T^2 - 1.082 \times 10^{-7}T^3) \quad (51)$$

$$\sigma_u = 1065 - 2.468T + 0.004087T^2 - 2.575 \times 10^{-6}T^3 \quad (52)$$

$$\varepsilon'_f = 100 \log(1 + \varepsilon_f) \quad (53)$$

$$\frac{\sigma'_f}{E} = 2.5 \times 10^8 (1 + \varepsilon_f) \sigma_u \quad (54)$$

$$b = -0.06 \quad (55)$$

$$c = -0.63; \quad (56)$$

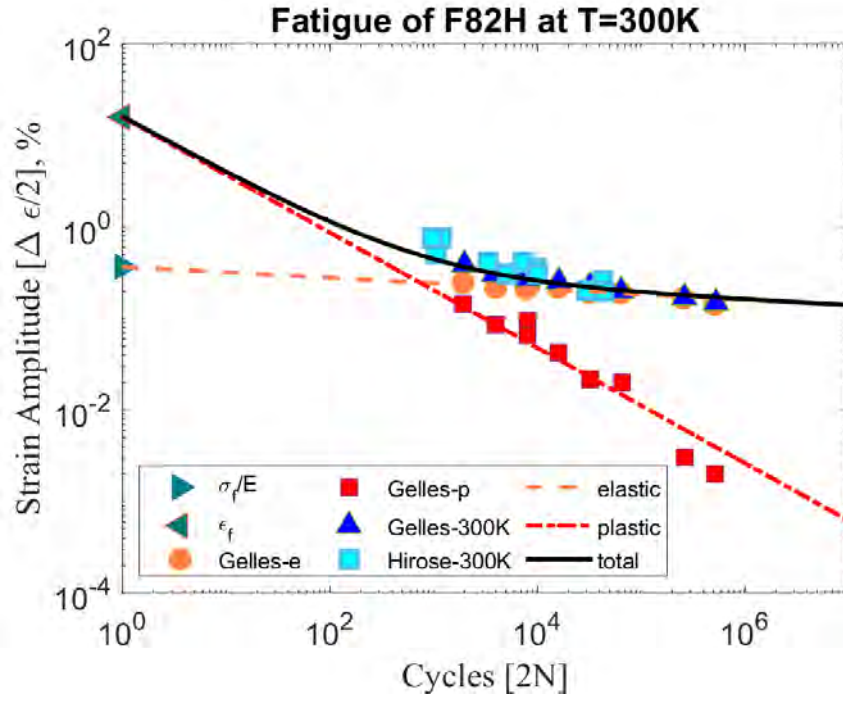


Figure 38: Room temperature fatigue strain amplitude versus the number of reversals for F82H. Data are taken from references [31, 32]

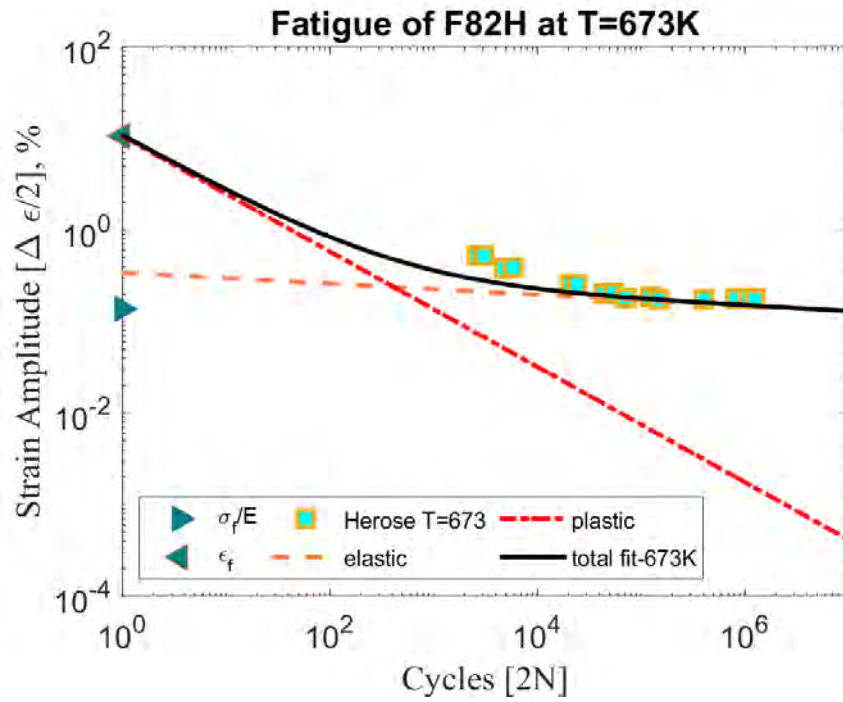


Figure 39: Fatigue strain amplitude versus the number of reversals for F82H at 673K. Data are taken from reference[32]

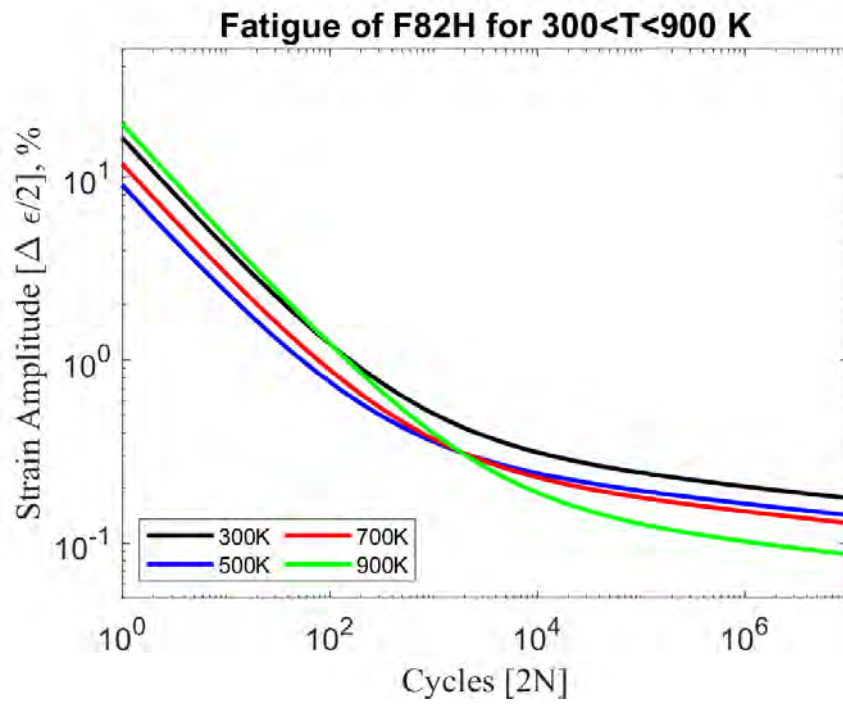


Figure 40: Predicted fatigue strain amplitude versus the number of reversals for F82H in the temperature range of 500-900 K. Data are taken from reference[32]



## 5 Radiation Effects on Mechanical Properties

### 5.1 Strength

#### 5.1.1 Yield Strength

We use the dispersed barrier model [33] to determine the increase in the yield strength of F82H. The model gives:

$$\Delta\sigma_y^d = C\sqrt{1 - \exp(-\frac{\Phi}{\Phi_0})} \quad (57)$$

where  $C$  and  $\Phi_0$  are model parameters,  $\Delta\sigma_y^d$  is the increase in the yield strength due to displacement damage at a neutron irradiation dose of  $\Phi$  is units of (dpa). The parameter  $C$  is related to the saturation density of radiation-induced defect clusters (interstitial or vacancy loops). It is therefore dependent on the temperature through the temperature dependence of the defect density. Thus, a temperature-dependent version of the Makin-Minter model is:

$$\Delta\sigma_y^d = C(T)\sqrt{1 - \exp(-\frac{\Phi}{\Phi_0})} \quad (58)$$

In reference [5], the parameter  $C(T)$  was given as:  $C_d \exp(-\nu \exp[-\frac{\Gamma}{kT}])$ . For helium bubbles, the increase in yield is given by [34, 5],

$$\Delta\sigma_y^{He} = C_{He} [\beta(\phi \times h)^{m-2}/\phi^3 D^2]^{1/2m} \sqrt{\Phi - \Phi_0^{He}} \quad (59)$$

The parameters that fit the F82H data are given by [5]:

$C_d$	$\Gamma$	$\nu$	$\Phi_0^d$	$C_{He}$	$D_0$	$U_a$	$\beta$	$\Phi_0^{He}$	m
500	0.9	$10^7$	3	330	$10^{-5}$	0.93	$10^{-30}$	$50 \times h$	7
MPa	eV	-	dpa	MPa	$m^2s^{-1}$	eV	$m^4$	dpa	-

Table 5: Hardening model parameters according to reference [5].

We collected available hardening data for F82H and Eurofer. The data were fitted to a function of the neutron dose (dpa), and the irradiation temperature,  $T$  [K]. Motivated by the Minter-Makin model and subsequent embodiment, the fitting function is given by:

$$\Delta\sigma_y^d = (a + bT + dT^2)\sqrt{1 - \exp(-dpa/c)} \quad (60)$$

The best-fit values of the constants are given by:  $a = 3700$ ,  $b = -7.9$ ,  $c = 9.992$ ,  $d = 0.0039$ . The function  $\Delta\sigma_y(T, dpa)$  is shown in Fig. 41, together with the hardening data from various sources [35].

The formation of helium bubbles as a result of the production of helium gas inside the steel by the inelastic  $(n, \alpha)$ -reaction will increase the yield strength of F82H further as a result of obstructing dislocation motion and glide. Available experimental data [35] on helium effects have been fitted to a function of the form:

$$\Delta\sigma_{He}(appm) = (a_1 + b_1\sqrt{appm})\sqrt{(1 - \exp(-appm/c_1))} \quad (61)$$

The fitting coefficients (with 95% confidence bounds) are:  $a_1 = -233.5$ ,  $b_1 = 0.4 A_{He}$ , and  $c_1 = 0.02922$ , where  $\Delta\sigma_{He}$  is in MPa. The value of  $A_{He}$  is related to the helium diffusion coefficient by

$$A_{He} = C_{He}(D(T)/D(300))^{-1/m}$$

The results of the data fit are shown in Fig. 45.

The yield strength as a function of temperature  $T$  [K] and irradiation dose [dpa] is obtained by adding up the yield strength as a function of temperature (Equation 12) to the increase due to irradiation given by Equations 60 and 61, for dpa and helium effects, respectively. The results are shown in Fig. 46.

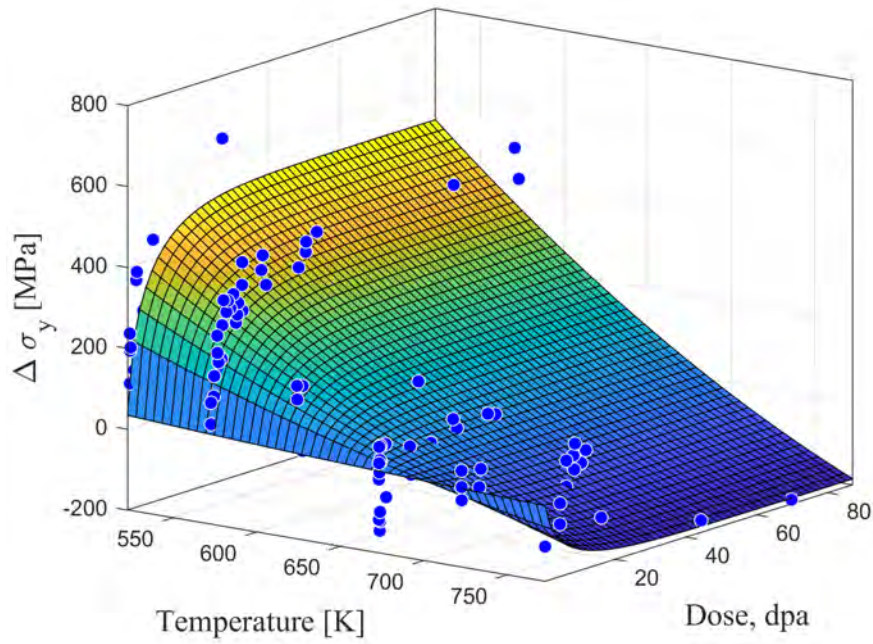


Figure 41: Temperature (K) and neutron dose (dpa) dependence of radiation hardening (increase in yield strength) of F82H. The fitting function (surface) is shown together with experimental data obtained from various sources and compiled by [35].

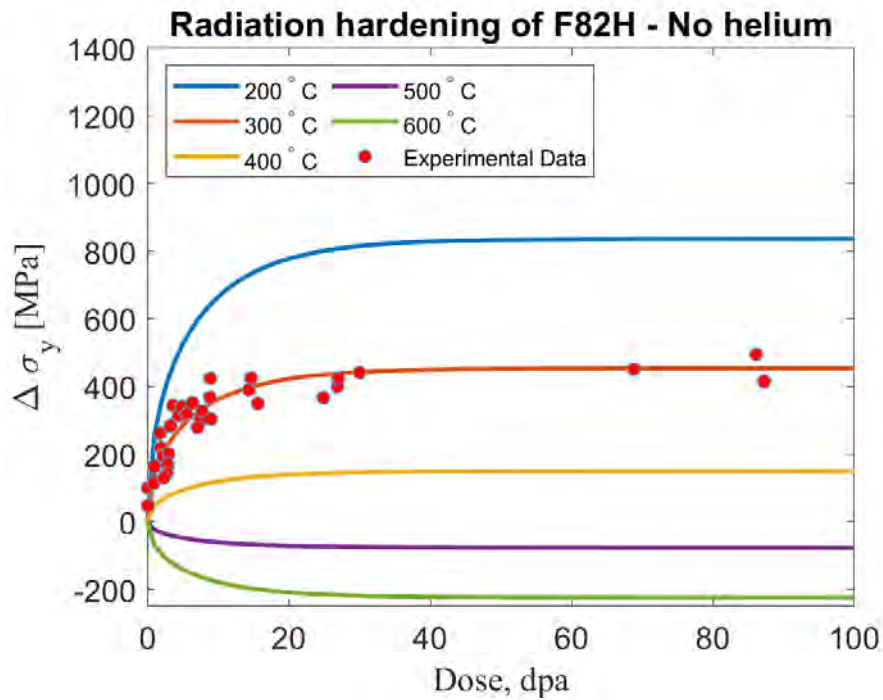


Figure 42: Neutron dose (dpa) dependence of radiation hardening (increase in yield strength) of F82H without the effects of helium bubbles on the yield strength.

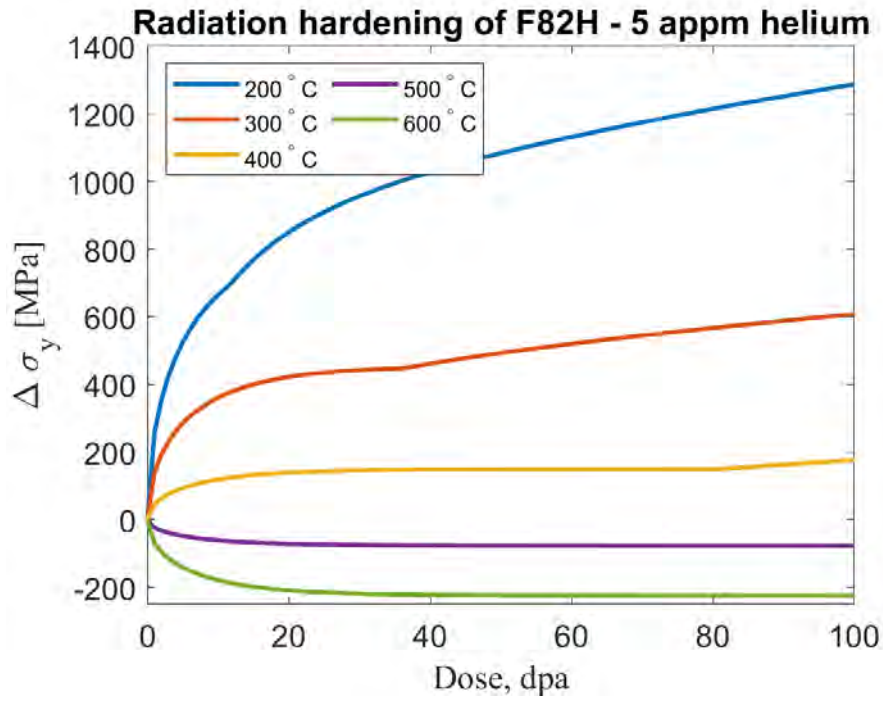


Figure 43: Neutron dose (dpa) dependence of radiation hardening (increase in yield strength) of F82H at a helium-to-dpa ratio of 5 appm/dpa.

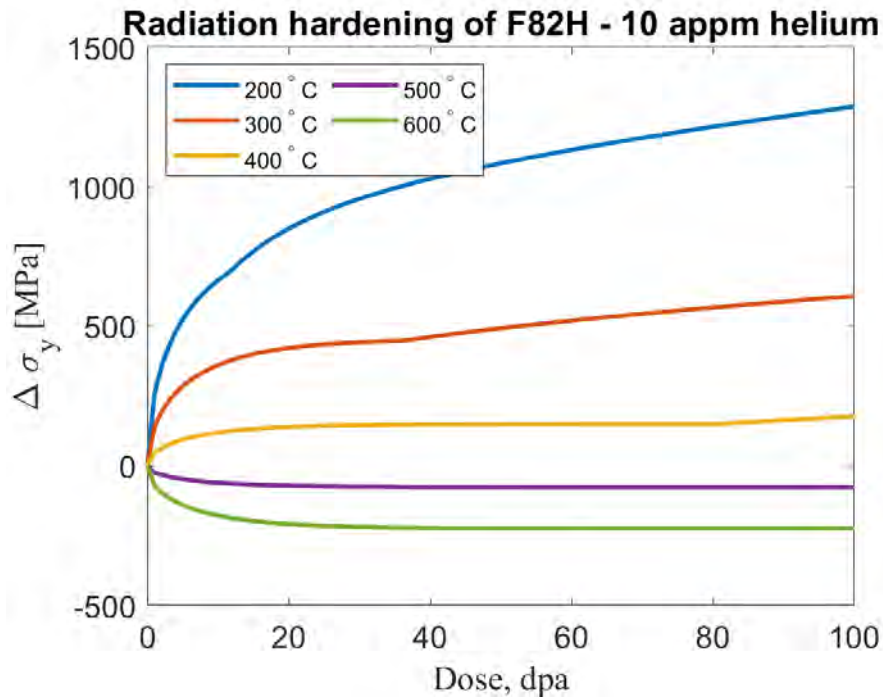


Figure 44: Neutron dose (dpa) dependence of radiation hardening (increase in yield strength) of F82H at a helium-to-dpa ratio of 10 appm/dpa.

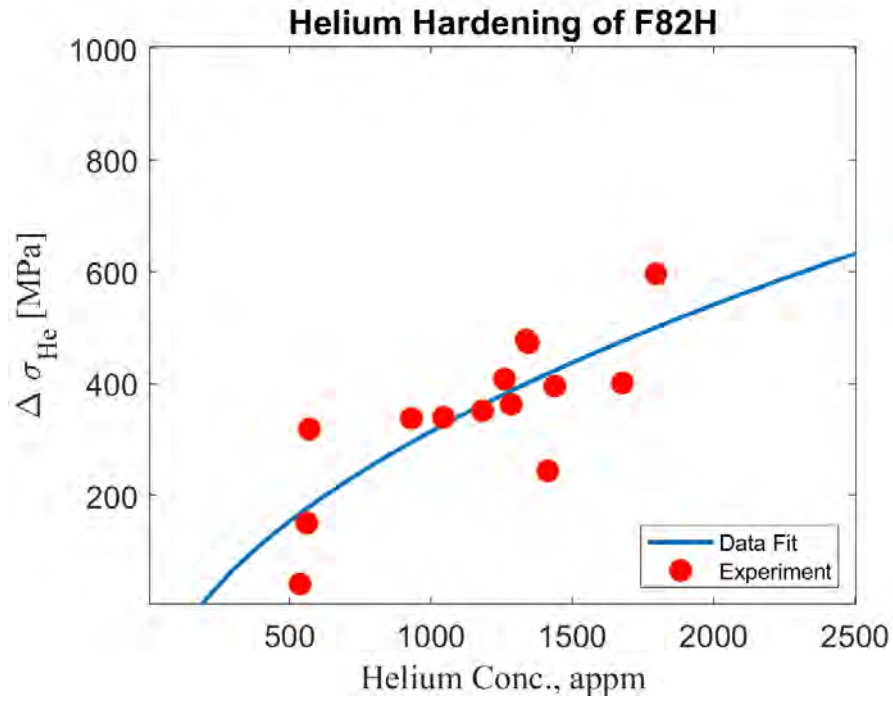


Figure 45: Dependence of radiation hardening (increase in yield strength) of F82H on the concentration of helium in appm.

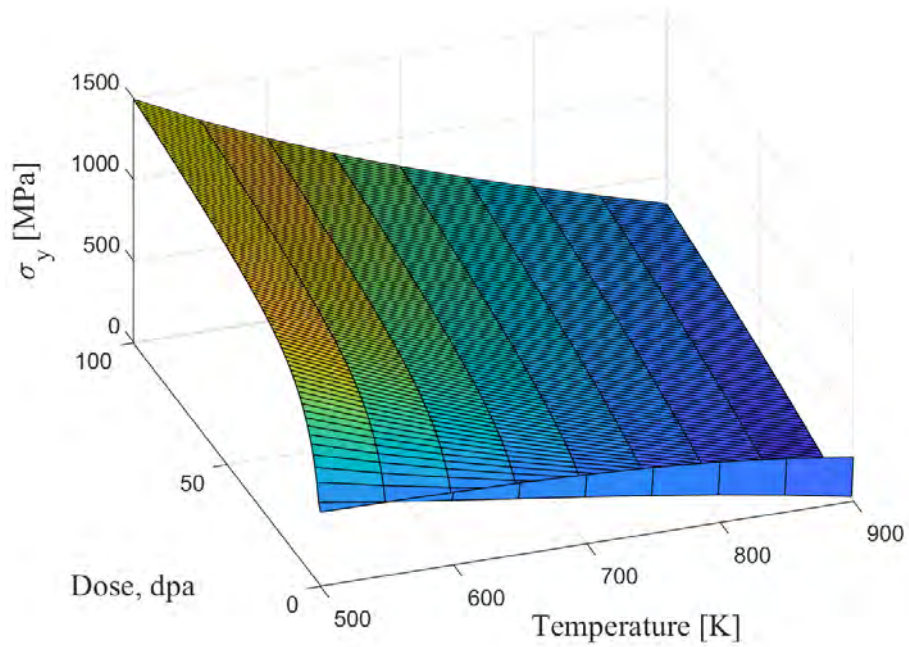


Figure 46: Dependence of the yield strength of F82H on the neutron dose (dpa) and temperature (K) from appm He/dpa ratio of 10.

### 5.1.2 Ultimate Strength & Tangent Modulus

Because of the lack of data on the details of the stress-strain behavior of F82H under irradiation, we will assume that the yield and ultimate strength are linearly related through the uniform elongation [36]. Thus, if we use the relationship  $\varepsilon_u = C(1 - \sigma_y/\sigma_u)$ , where  $C$  is a temperature-dependent parameter, determined from the un-irradiated data. Thus, using the unirradiated correlations developed earlier, we find:

$$C(T) = \varepsilon_u(T) / (1 - \sigma_y(T)/\sigma_u(T)) \quad (62)$$

The temperature-dependencies of  $\sigma_y$ ,  $\sigma_u$ , and  $\varepsilon_u$  are given in Equations 14, 12, and 13, respectively. Finally, we can obtain the ultimate strength as a function of neutron dose and temperature in the form:

$$\sigma_u(T, dpa) = \frac{\sigma_y(T, dpa)}{(1 - \varepsilon_u(T, dpa)/C(T))} \quad (63)$$

The dependence of the ultimate strength on the temperature  $T$  [K] and neutron dose [dpa] at a helium-to-dpa ratio of 10 is shown in Fig. 47. The tangent modulus, which is now a function of temperature and dose, is given by:

$$E_t = \frac{(\sigma_u - \sigma_y)}{(\varepsilon_u - 0.001)} \quad (64)$$

The dependence of the tangent modulus [GPa] on temperature  $T$  [K] and radiation dose [dpa] is shown in Fig. 48.

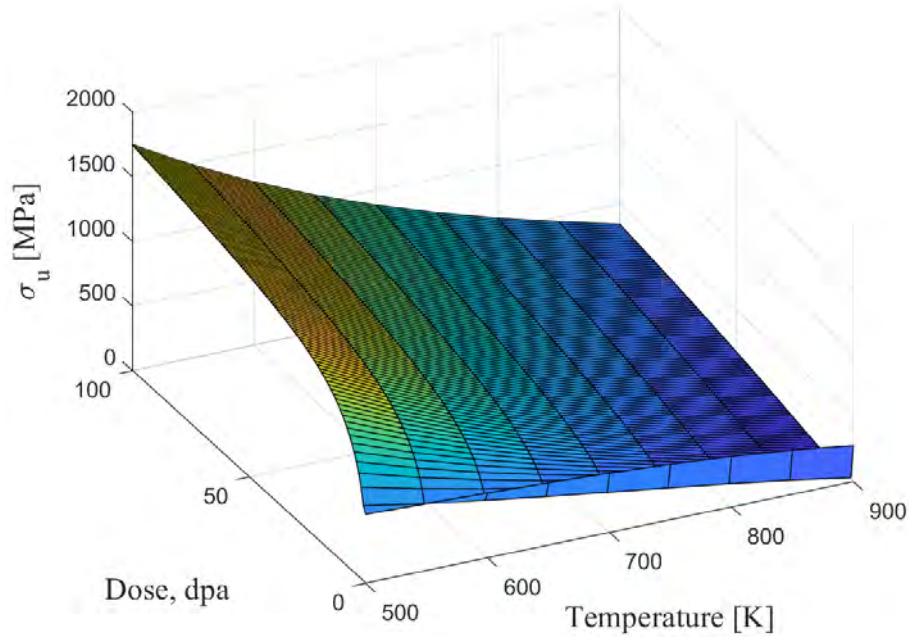


Figure 47: Dependence of the ultimate strength of F82H on the temperature,  $T$  [K], and neutron dose [dpa] at a helium-to-dpa ratio of 10.



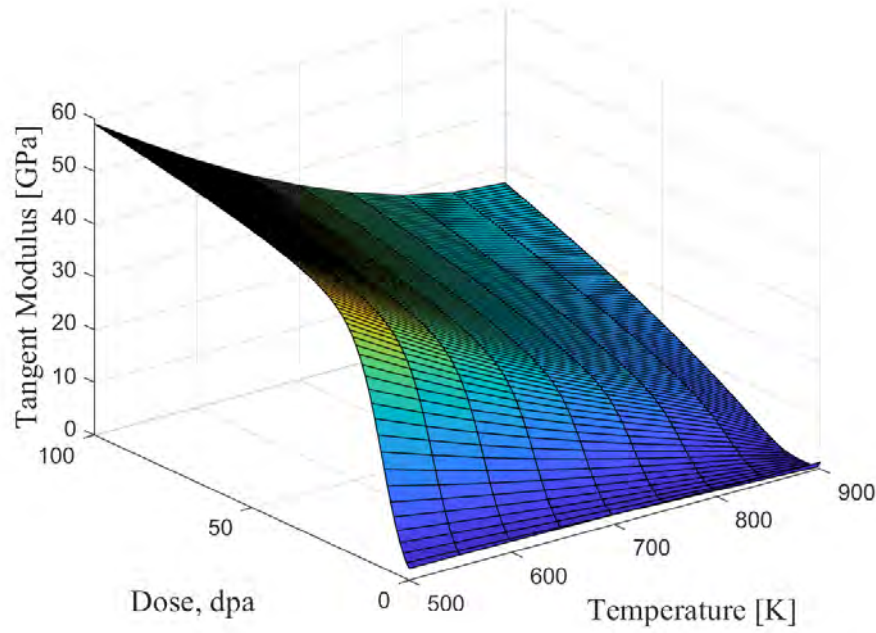


Figure 48: Dependence of the tangent modulus [GPa] on temperature  $T$  [K] and radiation dose [dpa] at a helium-to-dpa ratio of 10.

## 5.2 Ductility

### 5.2.1 Total Elongation

The total elongation remains at an acceptable level of above 5% for RAFM steels even after neutron irradiation up to 80 dpa. The surface fit for the total elongation ( $\varepsilon_{tot}$  as a function of the neutron dose ( $x$  [dpa]) and temperature ( $y$  [K]) is given by:

```
surffit(x,y) = (62.09-0.2306*y+ 0.0003032*y^2-1.082e-7*y^3)*(a+b*x+c*x^2)
Coefficients (with 95% confidence bounds):
a =      1.066  (0.9976, 1.135)
b =    -0.004282 (-0.01595, 0.007384)
c =   -0.0001004 (-0.0003582, 0.0001573)
```

The fitting function for the total elongation and experimental data are shown in Fig. 49, and can be written in the form:

$$\varepsilon_{tot} = ((62.09 - 0.2306T + 0.0003032T^2 - 1.082 \times 10^{-7}T^3)(1.066 - 0.004282 \times dpa - 0.0001004 \times dpa^2)) \quad (65)$$

where the temperature  $T$  is in Kelvin, and  $\varepsilon_{tot}$  is the total strain at fracture in [%]. A minimum value of 2% was assumed to prevent negative values from the fit at a high dose, as shown in Fig. 49.

The fitted surface for the total elongation extrapolated to 100 dpa, is shown in Fig. 50.

### 5.2.2 Uniform Elongation

The uniform elongation of FM steels falls below 0.5% after a few dpa [37]. This behavior linked with strong suppression of the strain hardening capability is believed to be correlated with the localization of inelastic



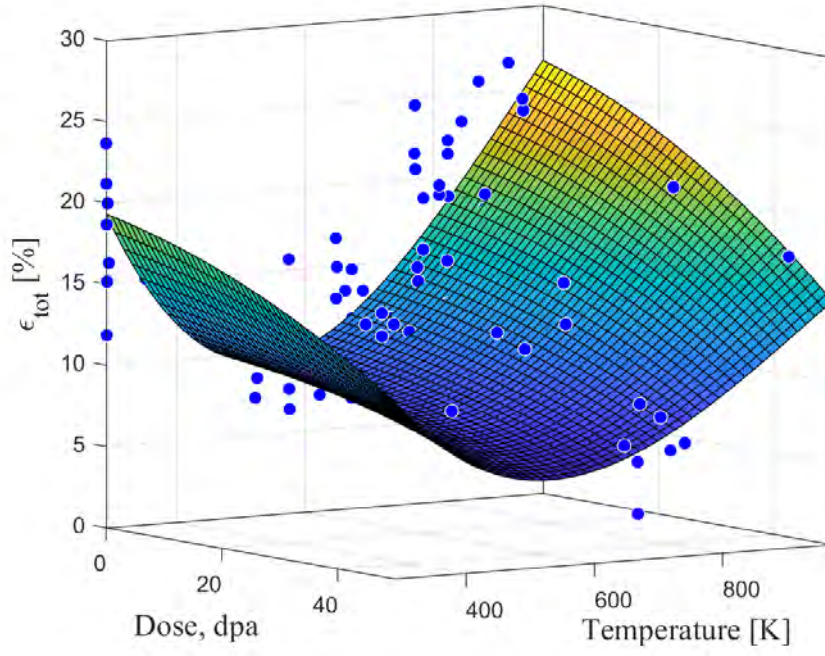


Figure 49: Dependence of the total elongation on the temperature and neutron dose (dpa) for F82H.

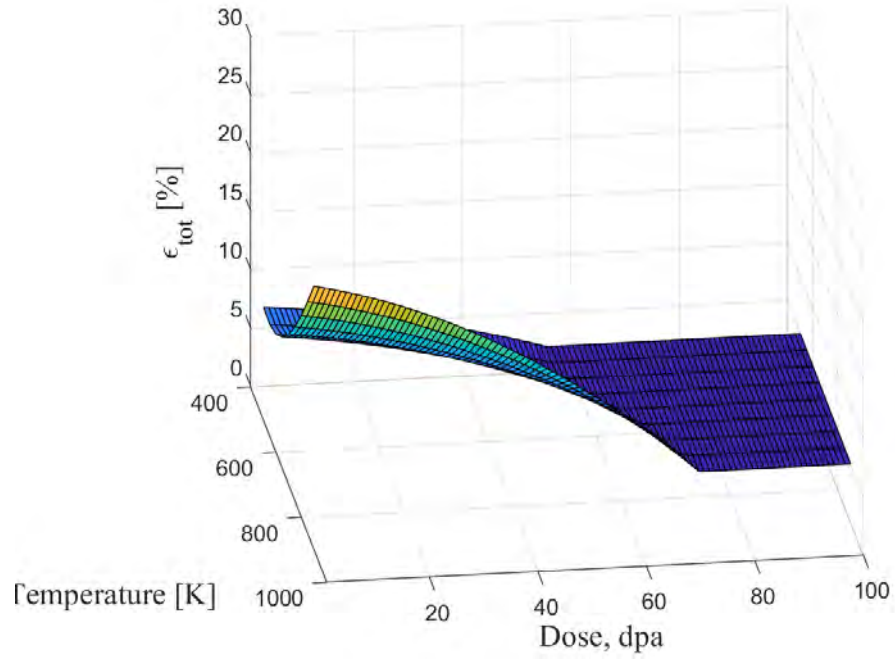


Figure 50: Dependence of the total elongation on the temperature and neutron dose (dpa) for F82H up to 100 dpa.

deformation in irradiated FM steels. In the case of EUROFER97, it was furthermore shown that a roughly linear relationship of the type  $\varepsilon_u = C(1 - \sigma_y/\sigma_u)$  holds between the uniform elongation  $\varepsilon_u$  and the strain hardening capability  $\sigma_y/\sigma_u$  [36]. Data on the uniform elongation at 350 °C shows a sharp drop after a few dpa [37]. The data was fit to a function of the form:

$$\varepsilon_u(350C) = 0.5118 + 2.942 \exp(-dpa/3.906) \quad (66)$$

Data at various temperatures for the uniform elongation as a function of dpa are not available. We will assume that the ratio of the irradiated to the unirradiated value of the uniform elongation remains the same for any other temperature. The ratio is thus given by:

$$f_{irr} = 0.1482 + 0.8518 \exp(-dpa/3.906) \quad (67)$$

Equations 14, and 67 can be used to determine the uniform elongation at an operational temperature T [K] and at any neutron dose [dpa]. The functional dependence is thus given by:

$$\varepsilon_u = (0.1482 + 0.8518 \exp(-dpa/3.906))(7.393 - 0.002602T - 1.649 \times 10^{-5}T^2 + 1.282 \times 10^{-8}T^3) \quad (68)$$

The dependence of the uniform elongation on the neutron dose and the irradiation temperature [K] is shown in Fig. 51.

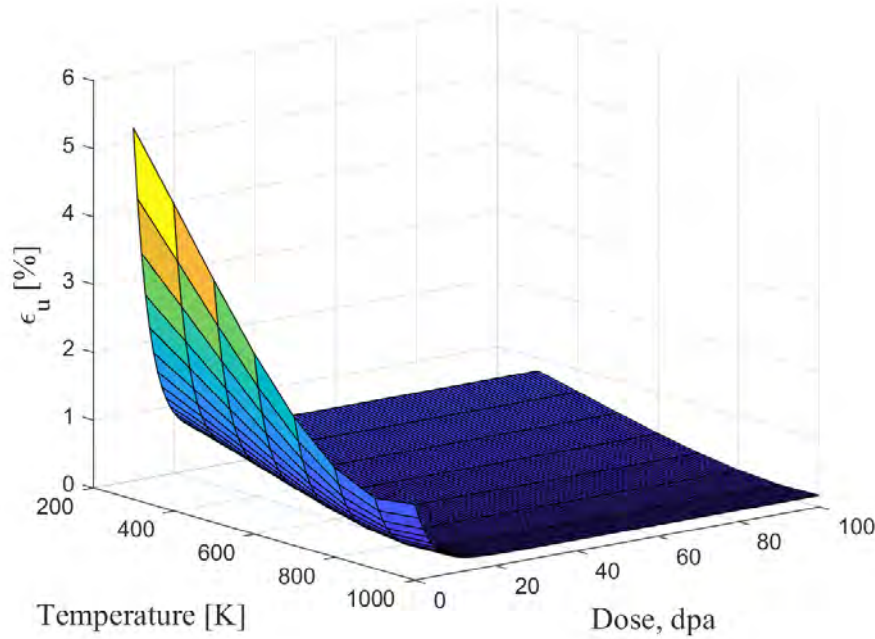


Figure 51: Dependence of the uniform elongation on the temperature and neutron dose (dpa) for F82H.

### 5.3 Stress-Strain Relationship

Because we now have complete information on the elastic properties, which are assumed not to be affected by irradiation, the yield strength, the ultimate strength, the uniform elongation, and the total elongation, we can construct approximate stress-strain diagrams for irradiated F82H at the operating temperature and neutron radiation dose. The fracture strength has been estimated as a linear combination of the yield and ultimate strengths from unirradiated data. Figures 52, 53, 54, and 55 show the predicted stress-strain relationships for F82H at 300, 400, 500, and 600 °C, respectively, taken at 20, 40, 60, 80, and 100 dpa.

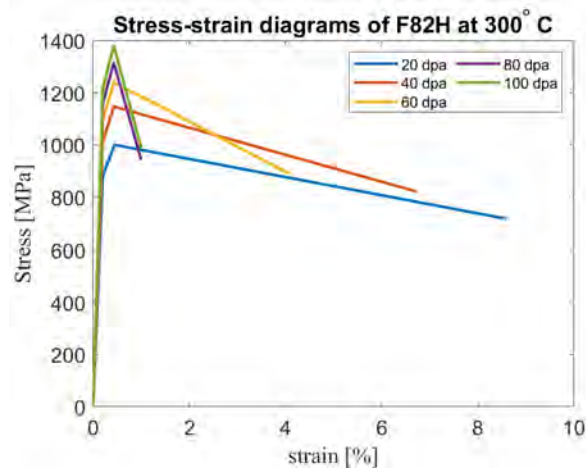


Figure 52: Predicted stress-strain relationship (simplified) for F82H at 300 °C at various neutron dose (dpa).

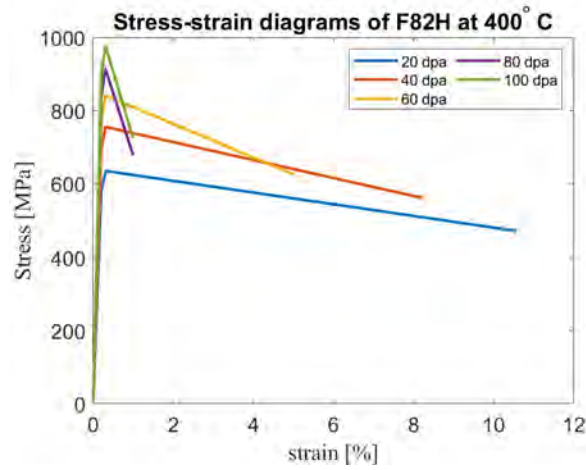


Figure 53: Predicted stress-strain relationship (simplified) for F82H at 400 °C at various neutron dose (dpa).

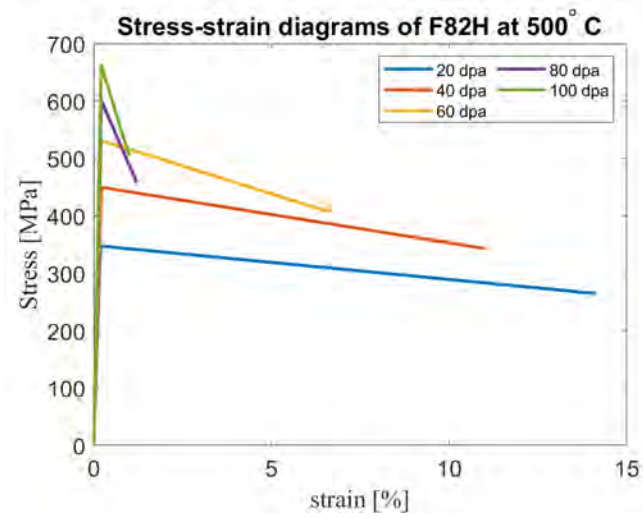


Figure 54: Predicted stress-strain relationship (simplified) for F82H at 500 °C at various neutron dose (dpa).

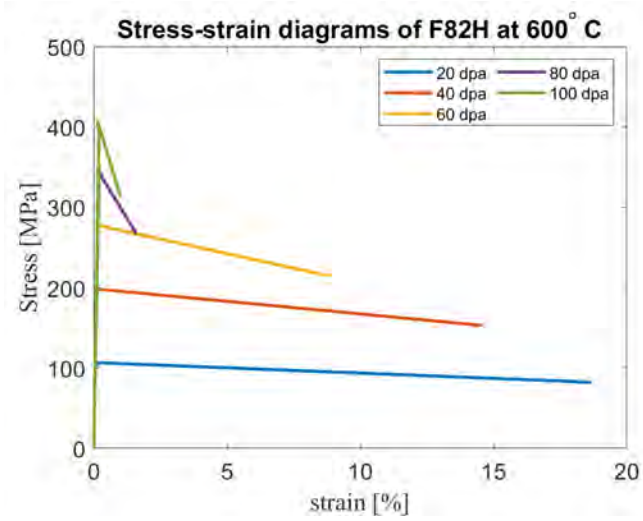


Figure 55: Predicted stress-strain relationship (simplified) for F82H at 600 °C at various neutron dose (dpa).

## 5.4 Volumetric Swelling

Neutron-induced void and bubble swelling ( $f_v$ ) is modeled as an inelastic isotropic strain. We will describe a simplified bi-linear swelling model based on the analysis of [38]. The diagonal components of the inelastic strain tensor ( $\epsilon^{\text{in}}$ ), which correspond to volumetric swelling ( $\epsilon^{\text{s}}$ ), are all set to be equal, where:

$$S = \Delta V/V = \epsilon_{11}^{\text{s}} + \epsilon_{22}^{\text{s}} + \epsilon_{33}^{\text{s}} \quad (69)$$

$$\epsilon_{11}^{\text{s}} = \epsilon_{22}^{\text{s}} = \epsilon_{33}^{\text{s}} = \frac{1}{3}S \quad (70)$$

Thus, the total strain tensor is composed of an elastic component, ( $\epsilon^{\text{e}}$ ), an inelastic component ( $\epsilon^{\text{in}}$ ), and a thermal strain component, ( $\alpha(T - T_0)\mathbf{I} = \alpha\Delta T\mathbf{I}$ ), where  $\alpha$  is the coefficient of thermal expansion, and  $\mathbf{I}$  is the identity tensor. The inelastic component is further decomposed into a volumetric swelling strain ( $\epsilon^{\text{s}}$ ), and a plastic strain ( $\epsilon^{\text{p}}$ ). One can then write:

$$\epsilon = \epsilon^{\text{e}} + \epsilon^{\text{p}} + \alpha\Delta T\mathbf{I} + \frac{f_v}{3}\mathbf{I} \quad (71)$$

The constitutive relationship between stress and strain as:

$$\sigma = \mathbf{C} : \epsilon^{\text{e}} = \mathbf{C} : \left( \epsilon - (\epsilon^{\text{p}} + \alpha\Delta T\mathbf{I} + \frac{S}{3}\mathbf{I}) \right) \quad (72)$$

where  $\mathbf{C}$  is the elastic constants tensor. The material properties in Equation 72 are generally functions of the triplet  $(\Phi, T, r)$ . However, not all the dependencies are available at the present time, and one has to make best estimates, consistent with current data and discuss the trends.

Neutron swelling data at 500 °C has been thoroughly analyzed by [38], and several suggested data fits were discussed. The swelling rate for F82H is very low below an incubation dose and then accelerates at a higher dose. There is considerable uncertainty in these predictions because of the lack of dedicated prototypical fusion irradiation facilities. This uncertainty is reflected in bounds for the swelling rate (minimum and maximum) that are consistent with current understanding [38].

The temperature dependence of the swelling is fitted to the Brailsford-Bullough function [39], and the fit is given by:

$$F(T) = -3.8603 \times 10^{-14}T^6 + 1.5344 \times 10^{-10}T^5 - 2.519 \times 10^{-7}T^4 + 0.00022T^3 - 0.10568T^2 + 26.9834T - 2843.2449 \quad (73)$$

The temperature dependence of the function  $F(T)$  is shown in Figure 56.

The volumetric swelling for HT9 at the peak swelling temperature is given by:

$$f_v = 0.035\Phi(1 - \exp(-\Phi/500)) \quad (74)$$

Guided by the swelling data of HT9, and the data in references [40, 41], the suggested dose-dependent swelling of F82H is given by:

$$F(\Phi, r) = 0.003(1 + 0.4r)\Phi(1 - \exp(-\Phi/(300 - 5r))) \quad (75)$$

where  $r$  is the helium-to-dpa ratio in appm/dpa. The fitted data for HT9, together with the predicted relationship for F82H at 10 appm/dpa are shown in Figure 57.

The suggested volumetric swelling of F82H as a function of dose ( $\Phi$  [dpa]), helium-to-dpa-ratio ( $r$  [appmHe/dpa]), and irradiation temperature ( $T$  [K]) is finally given by:

$$S_0(T, \Phi, r) = \frac{\Delta V}{V} = F(T)F(\Phi, r) \quad (76)$$

The predicted peak swelling as a function of dose (dpa) for F82H at 0, 10, and 20 appmHe/dpa is shown in Figure 58.

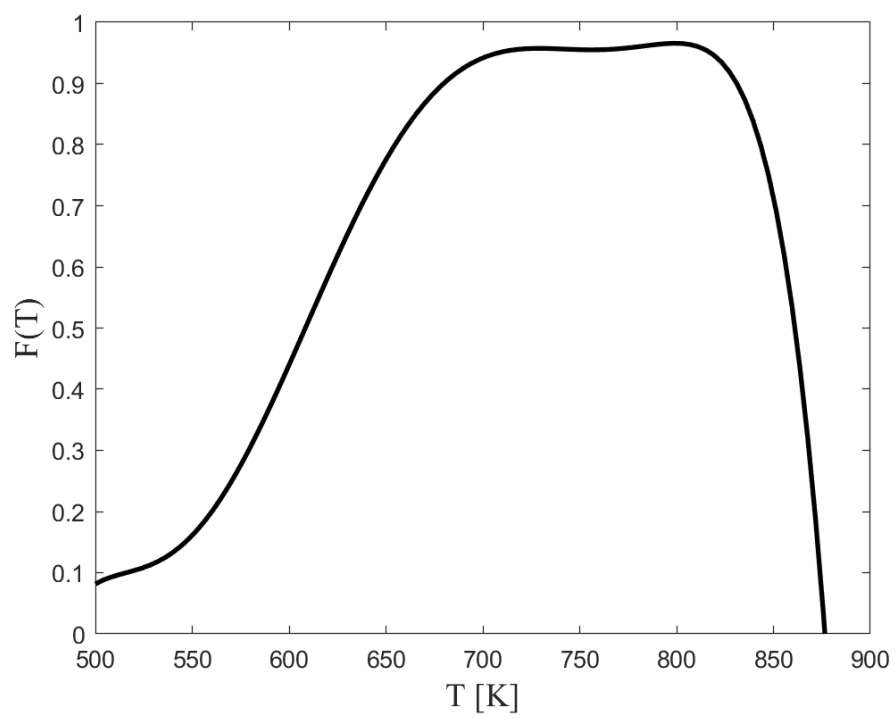


Figure 56: Temperature dependence of the swelling rate in F82H [39]



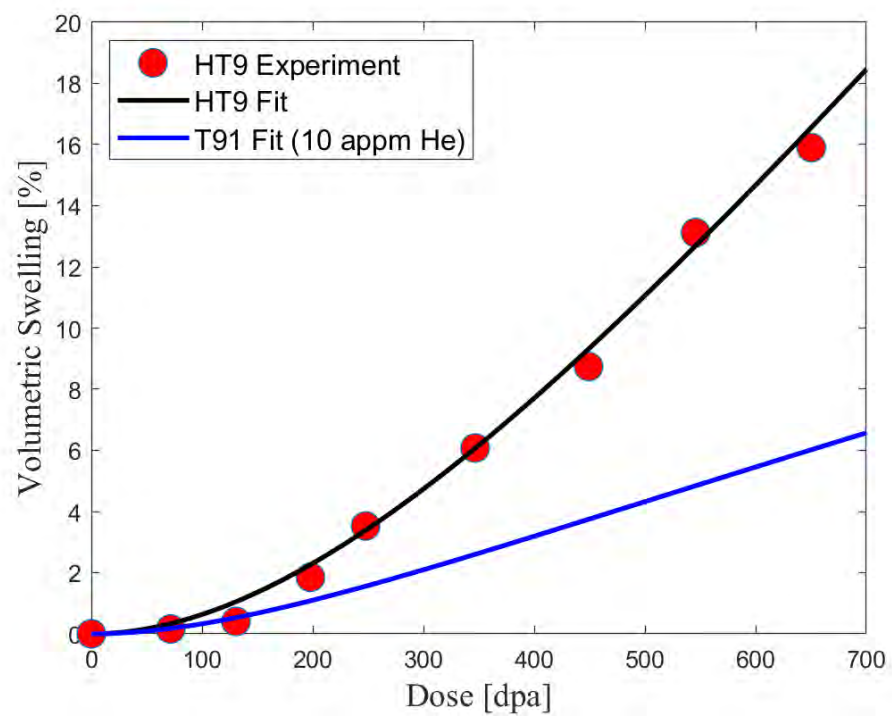


Figure 57: Dose dependence of the swelling in HT9 and F82H at 10 appm/dpa [40, 41]

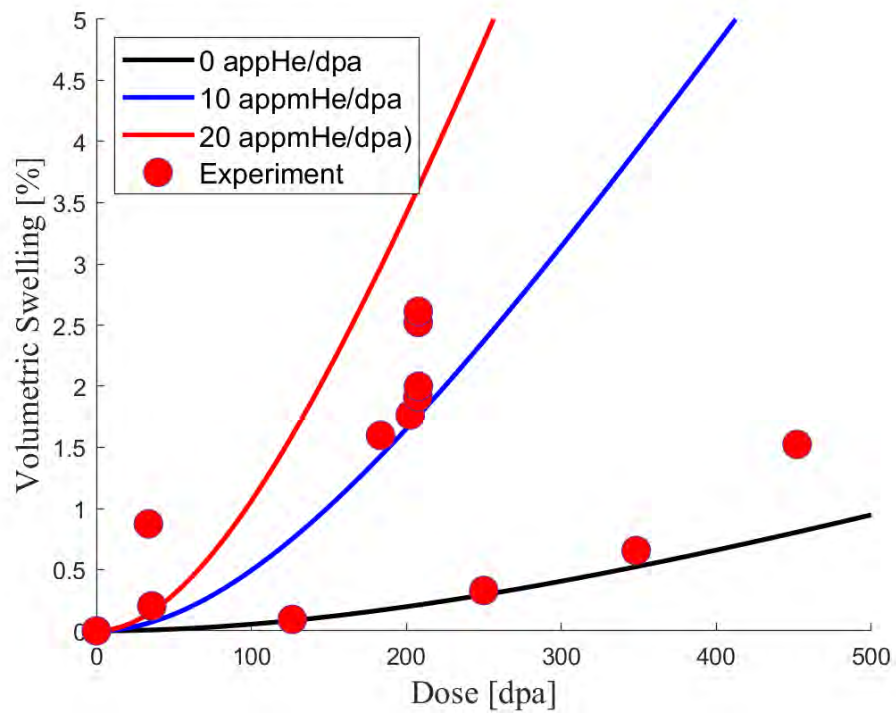


Figure 58: Predicted dose dependence of the swelling F82H at 0, 10, and 20 appmHe/dpa. Also shown are experimental data on T91 from reference [41] and F82H from reference [40].

At high stresses, the effects of external stress on the swelling rate can be significant. There is no data on the effects of stress on the volumetric swelling of F82H. However, the data available for austenitic steels can be used as an upper bound for stress effects. The only stress component that affects swelling is the hydrostatic stress component,  $\sigma_H = \frac{1}{3}(\sigma_{11} + \sigma_{22} + \sigma_{33})$ . The influence of stress on the volumetric swelling strain is given by [42]:

$$S = S_0(1 + B(T)\sigma_H) \quad (77)$$

where  $S_0$  is the "stress-free" swelling rate given above by Equation 76, and  $B(T)$  is a temperature-dependent coupling coefficient. The value of  $B(T)$  was found to be weakly-dependent on temperature and can be taken as constant. For F82H, we use the lower limit of values reported for austenitic steels. Thus,  $B(T) = 2 \times 10^{-3} \text{ MPa}^{-1}$  [42].

## 5.5 Fracture Properties

### 5.5.1 Ductile-Brittle Transition (DBTT)

The low-temperature design rules specify that the structure must avoid brittle fracture initiated from severe flaws and notches. The maximum mode-I stress intensity factor,  $K_I$ , due to all primary, secondary, and peak stress must be limited by the linear-elastic fracture toughness  $K_{IC}$ . To evaluate the structure's response to a postulated surface flaw following neutron damage, it is necessary to have correlations that relate  $K_{IC}$  to neutron displacement damage ( $\Phi$ ) and corresponding irradiation temperature ( $T_{irr}$ ), the operating temperature ( $T$ ), the shift in ductile to brittle transition temperature (DBTT), and width of the transition temperature ( $T_{trans}$ ) region between the Lower Shelf Energy (LSE) and the Upper Shelf Energy (USE).

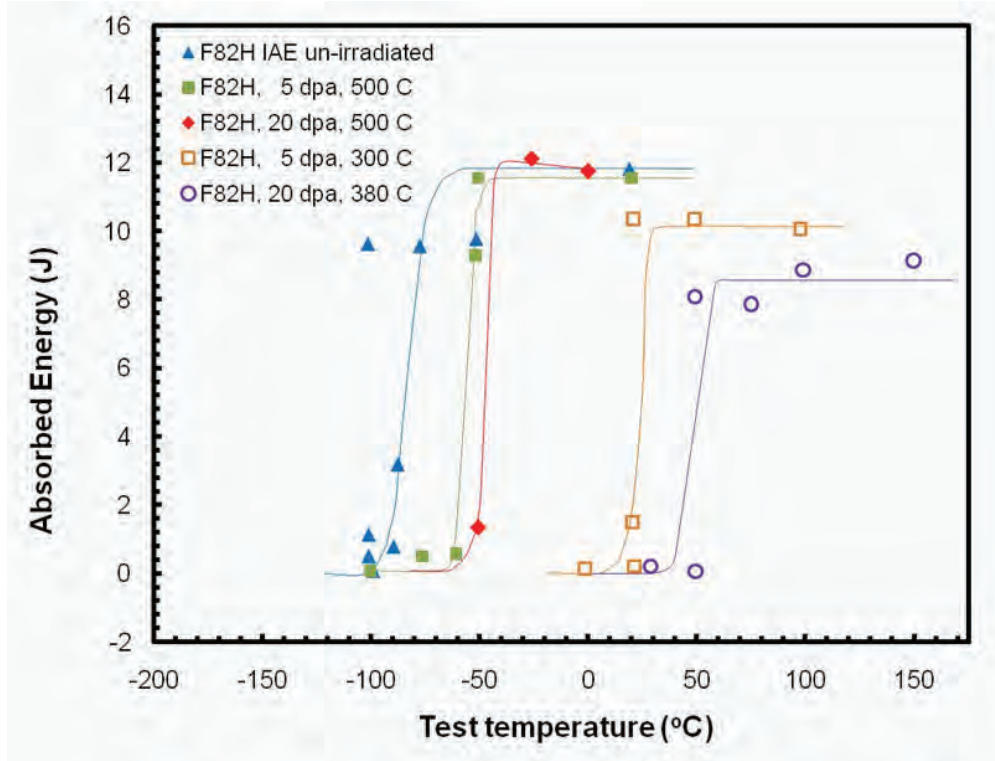


Figure 59: Charpy V-Notch impact energy of F82H IAE Heat [4]

### 5.5.2 Fracture Toughness

We represent the complex relationship of the fracture toughness  $K_{IC(irr)}$  on temperature ( $T$  [K]) and irradiation dose  $\Phi$  [dpa], using the following procedure.

Let the lower shelf fracture toughness be  $K_L$ , and the upper shelf value as  $K_U$ . They are both functions of the irradiation dose  $\Phi$ , and let the unirradiated DBTT be  $T_{DBTT}^0$ , and the width of the transition region in the DBTT be  $T_w$ . We follow the empirical relationship between the shift in DBTT and the displacement damage dose, such that the shift  $\Delta T_0 = A\Delta\sigma_y$ , where  $A$  is a constant and  $\Delta\sigma_y(\Phi, T)$  is the radiation hardening in [MPa].

$$K_{IC}^{irr}(\Phi, T) = K_L(\Phi) + \frac{1}{2} [(K_U(\Phi) - K_L(\Phi))] \times \left[ 1 + \tanh \left( \frac{T - T_{DBTT}(\Phi, T)}{T_w} \right) \right]$$

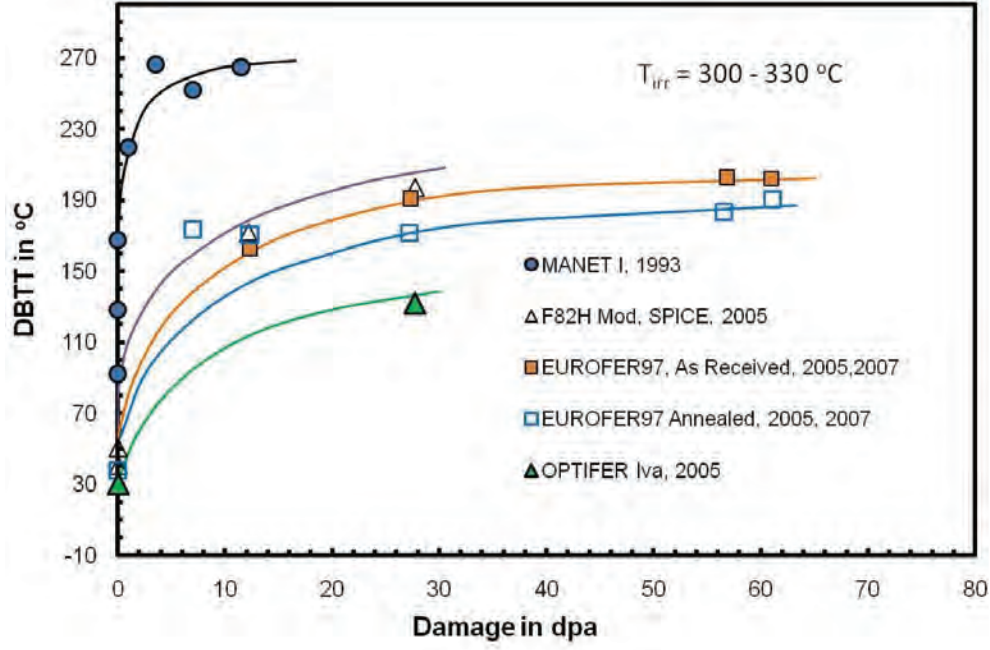


Figure 60: Shift in the DBTT for a number of F/M steels as a function of neutron displacement damage dose [9]

The functions in Equation 78 are given by:

$$T_{DBTT}(\Phi, T) = T_{DBTT}^0 + \Delta T_{DBTT}^0(\Phi, T) \quad (78)$$

$$K_L(\Phi) = (1 - B) \exp(-\Phi/\Phi_0) + B) K_L^0 \quad (79)$$

$$K_U(\Phi) = ((1 - B) \exp(-\Phi/\Phi_0) + B) K_U^0 \quad (80)$$

The values of the constants used in the previous equations for F82H are shown in Table 6.

A	B	$K_L^0$	$K_U^0$	$T_{DBTT}^0$	$T_w$	$\Phi_0$
-	-	MPa $\sqrt{(m)}$	MPa $\sqrt{(m)}$	[K]	[K]	dpa
0.25	0.4	30	220	223	50	25

Table 6: DBTT model parameters.

The ITER-TBM will experience maximum damage of 3.7 dpa at irradiation temperatures between 350 °C and 560 °C. As a first attempt, the  $K_{IC(irr)}$  correlation was therefore developed to within a range of maximum damage of 5 dpa and a maximum irradiation temperature of 560 °C. Corresponding fracture toughness data for F82H in this damage and irradiation regime was used. Fig. 61 shows the fracture toughness for un-irradiated and irradiated F82H at a damage of 5 dpa irradiated at 300°C, and Fig. 62 shows irradiated fracture toughness at a damage of 3.8 dpa irradiated between 221°C and 405°C. These data sets provide five  $K_{IC(irr)}$  data sets at irradiation temperatures, 220-280°C (average 250°C), 300°C, 350-400°C (average 375°C), 380°C, and 500°C. In addition, one set of data at a constant irradiation temperature of 500°C at two damage doses of 5 and 20 dpa is available. For the purpose of fitting the data, the values for  $K_{max}$  and

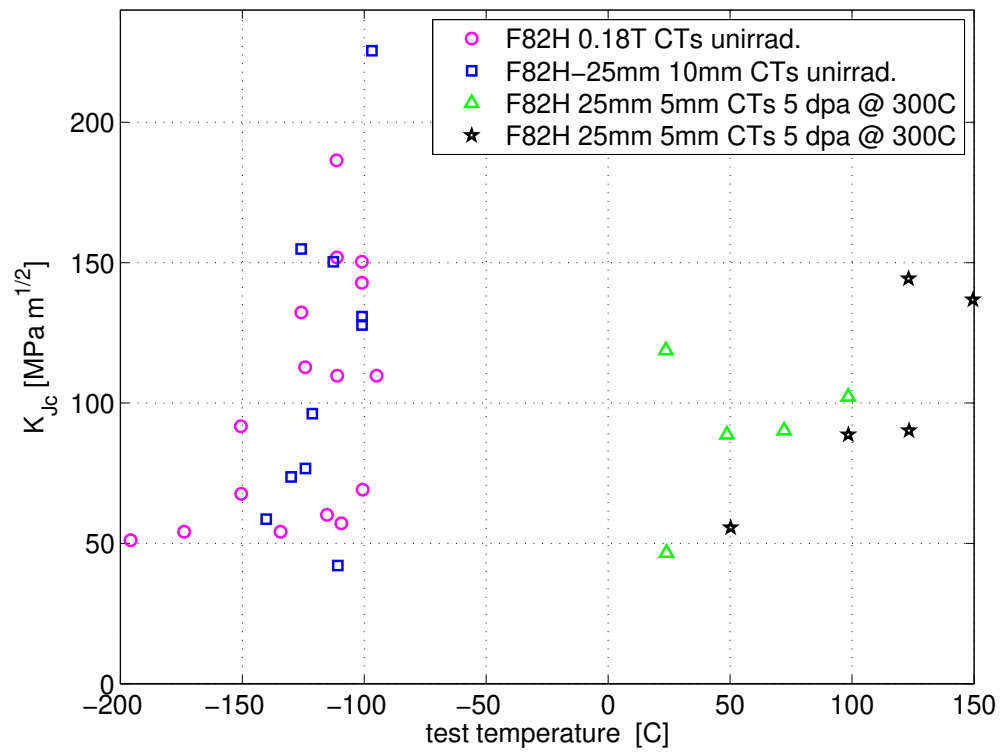


Figure 61: Dependence of the fracture toughness,  $K_{IC}$  on temperature for F82H, before and after irradiation to 5 dpa [43].



$K_0$  (upper/lower  $K_{IC}$ ) were taken to be the maximum and minimum reported values. The same holds for USE and LSE (Fig. 59).

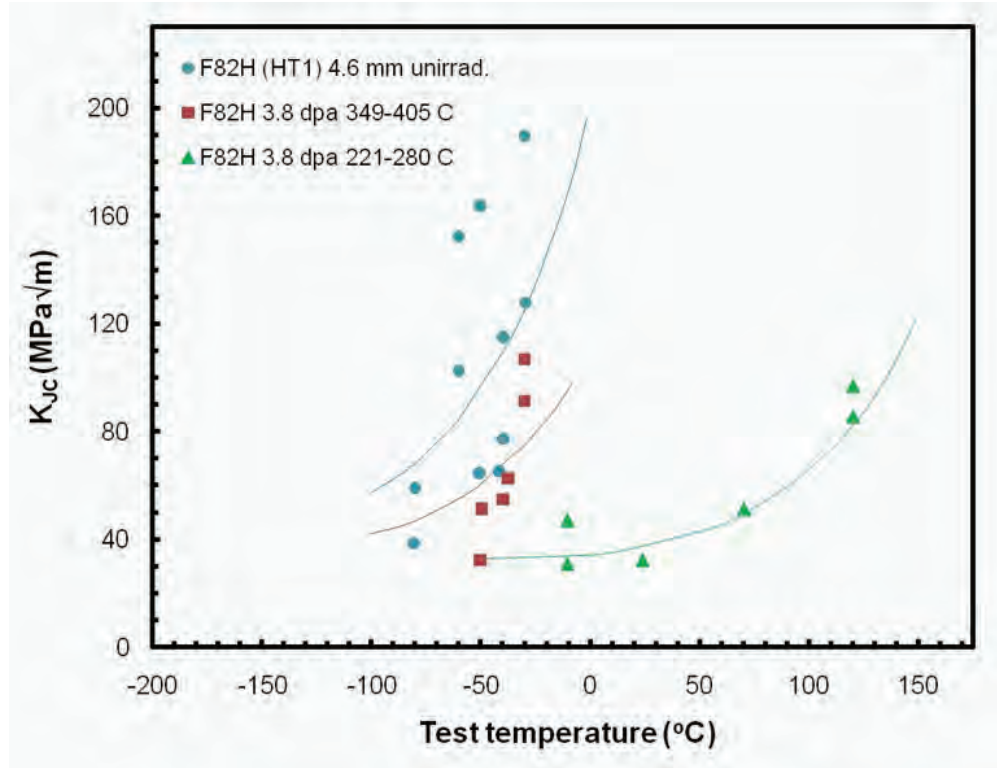


Figure 62: Fracture toughness data for F82H as normalized and tempered and after irradiation in HFIR at 221-280 and 349-405 °C to approximately 3.8 dpa (note: all data for F82H (HT1) T-L 4.6 mm thick DC(T)[44].

A representative sample of the developed correlation for  $K_{IC}$  along with some of the experimental data is shown in Fig. 63. The predicted dependence of the fracture toughness on dose and irradiation temperature is shown in Figs. 64 and 65.

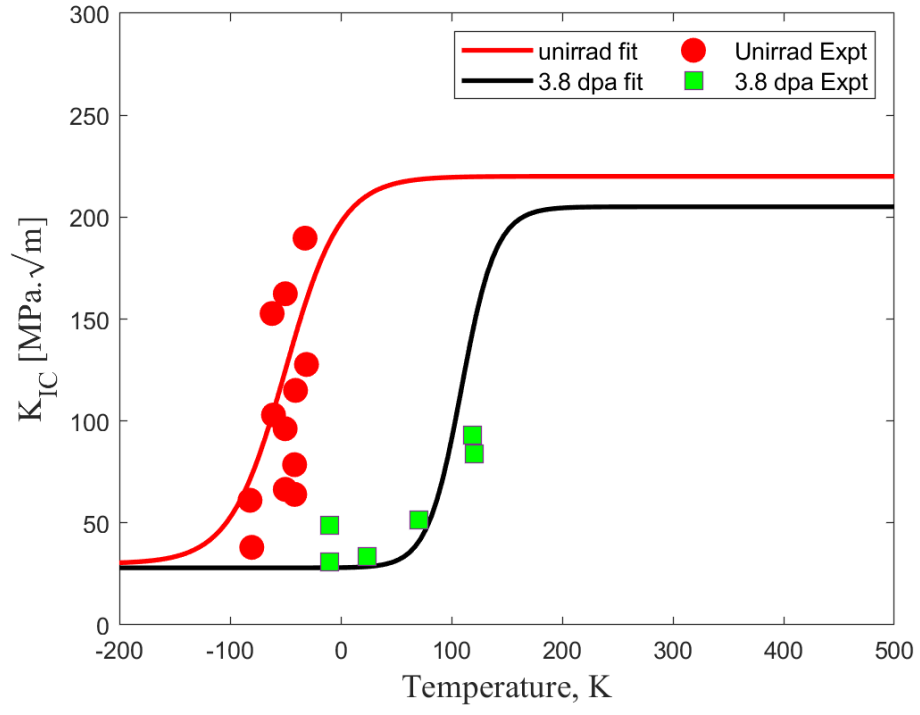


Figure 63:  $K_{IC(irr)}$  correlation (Eq. 78) fitted to experimental conditions [44].

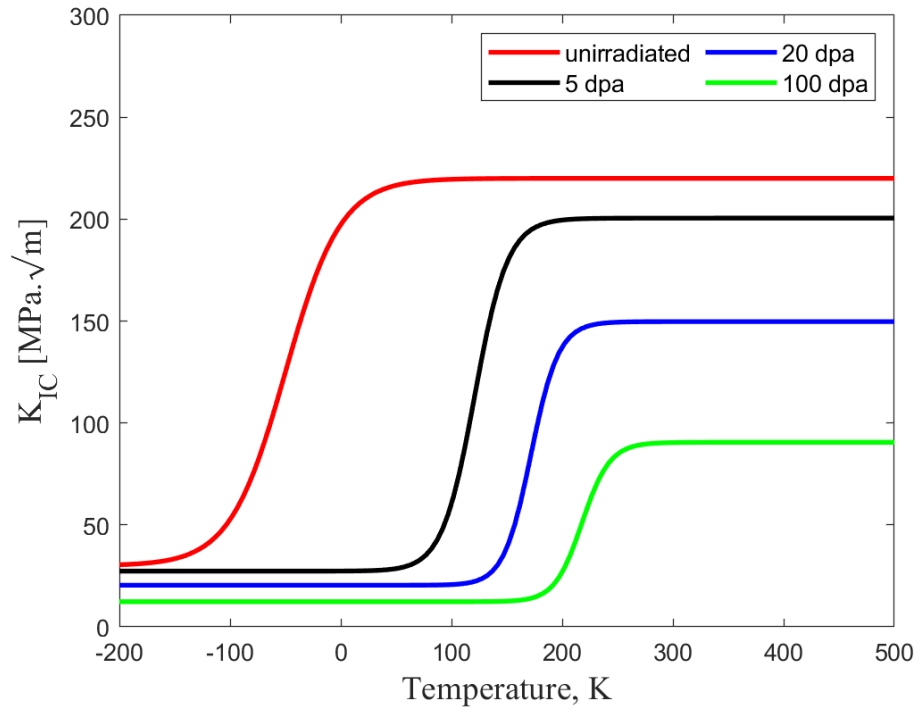


Figure 64:  $K_{IC(irr)}$  dependence on neutron irradiation dose and temperature.

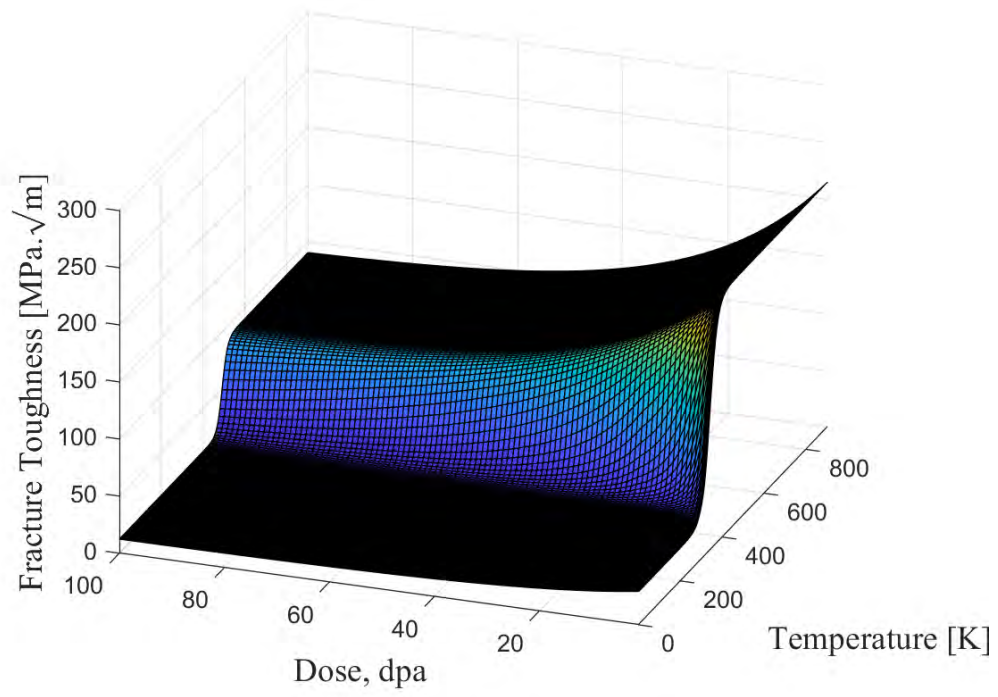


Figure 65:  $K_{IC(irr)}$  dependence on neutron irradiation dose and temperature, displayed as a 3D plot.

## 5.6 Irradiation Creep

The first suggestion for a correlation between swelling and creep was made by Foster et al. based on residual stress measurements in fuel pin cladding of type AISI 304 SS and on experiments with pressurized tubes. Foster et al. derived the following empirical equation:

$$\frac{d\varepsilon}{d\Phi} = (K + D \frac{de}{d\Phi})\sigma \quad (81)$$

where  $\Phi$  is the neutron fluence in dpa,  $e(T, \Phi)$  the “linear” swelling,  $K$  the irradiation creep ”compliance”, and  $D$  the swelling-creep coupling coefficient. The values of  $K$  and  $D$  obtained from experiments on various austenitic and ferritic/ martensitic steels are shown in Table 7. Recent data on F82H indicate that the stress

Steel Type	$K$ [dpa] <sup>-1</sup> .MPa <sup>-1</sup>	$D$ [MPa] <sup>-1</sup>	Reference
	Austenitic Steels		
SA-304L	$8.5 \times 10^{-7}$	0.01	[42]
CW-DIN1.4981	$1.4 \times 10^{-6}$	0.008	[45]
	Ferritic-Martensitic Steels		
HT-9	$5 \times 10^{-7}$	0.007 – 0.01	[42]
EM10 & EM11	$4.4 \times 10^{-7}$	0.006	[46]

Table 7: Irradiation creep compliance and creep-swelling coupling coefficients for various steels [42, 45, 46]

dependence of the irradiation creep compliance is not linear, and is also dependent on the irradiation dose. Helium content was not found to affect the irradiation creep compliance [47]. We modify the traditional irradiation creep correlation, given by Equation 81 to read as follows:

$$\frac{d\varepsilon}{d\Phi} = (K + D \frac{de}{d\Phi})\sigma^{m(T)} \quad (82)$$

where  $m(T)$  is a temperature-dependent exponent. Our analysis of the irradiation creep data give the following values for the irradiation creep compliance  $K$  and the exponent  $m$ .

$$m(T) = 1 + 0.0025U(T - 500)(T - 500) \quad (83)$$

$$K = 4 \times 10^{-7} \quad (84)$$

where  $U(T)$  is the unit step function, and the temperature is in [K]. The results of this procedure compared to the irradiation creep data are shown in Figure 66. The exponent  $m$ , when evaluated at 667 K is found to be 1.43, while it is found to be 1.68 at T=773 K.

The temperature dependence of irradiation creep is explained in terms of two mechanisms. At low temperatures, the primary mechanism is found to be Stress-Induced Preferential Absorption (SIPA), where the creep rate is linear in the applied external stress. However, at higher temperatures, roughly above 500 °C, the second mechanism is activated, contributing more significant creep rates than SIPA. This mechanism is the Preferential Absorption of point defects enabling climb-controlled Glide (PAG) for short [42].

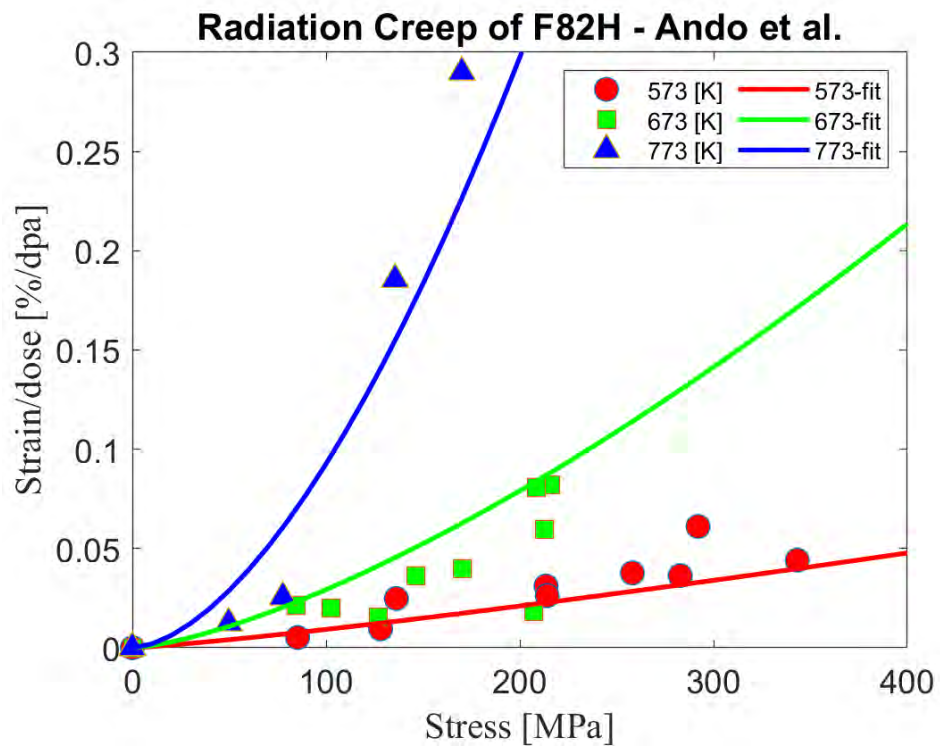


Figure 66: Irradiation Creep Strain dependence on stress and temperature. Data are taken from reference [47].

## 5.7 Fatigue Properties

We model the cyclic strain amplitude versus the number of cycles to failure using the same Coffin-Manson correlation that we developed for the unirradiated F82H. However, the effects of irradiation on fatigue properties are manifest in the reduction of plastic total ductility on the one hand, and in the increase in the fracture strength due to radiation hardening, on the other. It is interesting to note that while high-cycle fatigue properties may improve as a result of radiation hardening, it is the loss of ductility that will greatly impact low-cycle fatigue. The equations used to model the Manson-Coffin relationship are listed below.

$$\sigma_y^{un}(T) = 960.9 - 2.716T + 0.00496T^2 - 3.112e - 6T^3 \quad (85)$$

$$\sigma_u^{un}(T) = 1065 - 2.468T + 0.004087T^2 - 2.575 \times 10^{-6}T^3 \quad (86)$$

$$\varepsilon_u^{un}(T) = 7.393 - 0.002602T - 1.649 \times 10^{-6}T^2 + 1.282 \times 10^{-8}T^3 \quad (87)$$

$$\Delta\sigma_y(T, dpa) = \sqrt{(1 - \exp(-dpa/9.992))}(3700 - 7.9T + 0.0039T^2) \quad (88)$$

$$\Delta\sigma_{He}(x) = \max((-233.5 + 17.33\sqrt{x})\sqrt{1 - \exp(-x/0.02922)}, 0) \quad (89)$$

$$C(T) = 0.01\varepsilon_u^{un}(T)/(1 - \sigma_y^{un}(T)/\sigma_u^{un}(T)) \quad (90)$$

$$\sigma_y^{irr}(T, dpa) = \sigma_y^{un}(T) + \Delta\sigma_y(T, dpa) + \Delta\sigma_{He}(x) \quad (91)$$

$$\sigma_u^{irr}(T, dpa) = \sigma_y^{irr}(T, dpa)/(1 - 0.01\varepsilon_u^{un}(T)/C(T)) \quad (92)$$

$$\varepsilon_{tot}^{irr}(T, dpa) = \max(0.01(1.066 - 0.004282dpa - 0.0001004dpa^2) \dots \quad (93)$$

$$\times (62.09 - 0.2306T + 0.0003032T^2 - 1.082 \times 10^{-7}T^3), 0.01) \quad (94)$$

$$C(T, dpa) = 100 \ln(1 + \varepsilon_{tot}^{irr}(T, dpa)) \quad (95)$$

$$B(T, dpa) = 2.5(1 + \varepsilon_{tot}^{irr}(T, dpa))\sigma_u^{irr}(T, dpa) \times 10^8/E(T) \quad (96)$$

$$b = -0.06 \quad (97)$$

$$c = -0.63 \quad (98)$$

$$\Delta\varepsilon_e(T, dpa, N)/2 = B(T, dpa)N^b \quad (99)$$

$$\Delta\varepsilon_p(T, dpa, N)/2 = C(T, d)N^c \quad (100)$$

$$\Delta\varepsilon_{tot}(T, dpa, N)/2 = \Delta\varepsilon_e(T, dpa, N)/2 + \Delta\varepsilon_p(T, dpa, N)/2 \quad (101)$$

The results of this model are shown in Figure 67 and 68 at 10, 20, 50, and 100 dpa, respectively. Note the clear degradation of fatigue properties as a result of irradiation. The most severe effects of irradiation will be on cycles that generate large plastic strain amplitudes (low-cycle fatigue). The influence of irradiation on high-cycle fatigue seems not to be as significant.



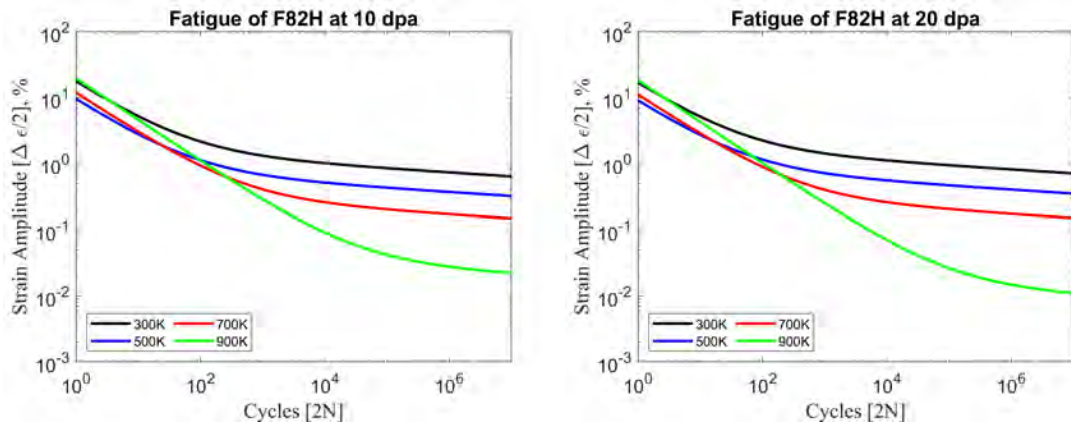


Figure 67: Strain amplitude versus the number of reversals (2N) for F82H irradiated to 10 & 20 dpa, at a He/dpa ratio  $x=10$ .

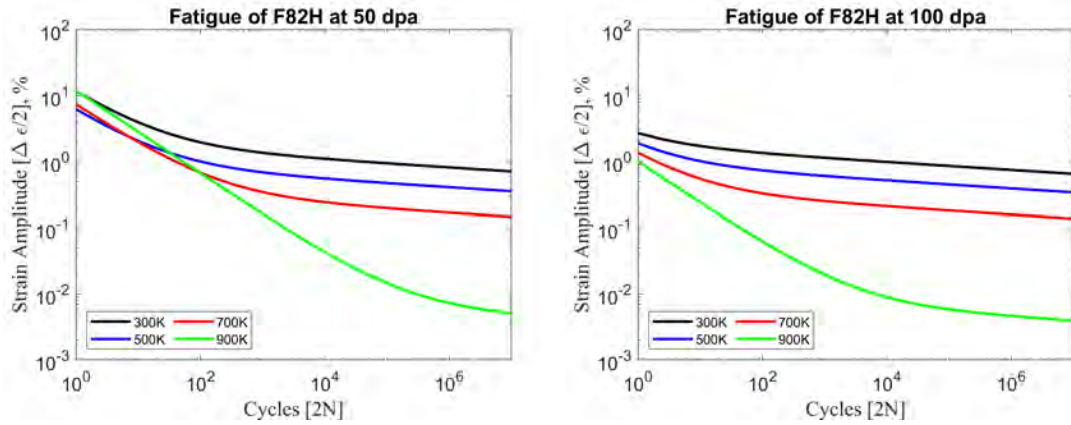


Figure 68: Strain amplitude versus the number of reversals (2N) for F82H irradiated to 50 & 100 dpa, at a He/dpa ratio  $x=10$ .

## 6 Chemical Compatibility

### 6.1 Liquid Metal Corrosion

Measurements of the time dependence of weight loss are important for estimations of structural wall thinning, deposition burdens, and radionuclide transport in the coolant system. For solubility-driven dissolution, the flux of an element into lithium or LiPb can be expressed as:

$$J = r_i(C_i^0 - C_i) \quad (102)$$

where  $C_i^0$  is the solubility of element  $i$  in the liquid metal,  $C_i$  is its actual concentration, and  $r$  is the mass transfer coefficient. Weight change results for type 316 stainless steel showed substantially higher dissolution rates as compared to F/M steels [48]. This difference can be attributed to the higher equilibrium solubility of Fe, Cr, and Ni in Pb-17Li [48] and is consistent with the solubility-controlled dissolution of the major alloying elements. The dominance of a  $\sqrt{t}$  dissolution in austenitic during the first few thousand hours indicates a diffusion-controlled mechanism till a ferrite layer is formed. Beyond this initial period, the dissolution rate is linear in time.

On the other hand, the dissolution kinetics of F/M steels shows a linear dependence on time right from the start. We express the dissolution rates of F/M steels in lithium and LiPb as an Arrhenius type process, given by:

$$R = A \exp\left(-\frac{Q}{kT}\right) \quad (103)$$

where  $R$  is the surface recession rate (in  $\mu\text{m}/\text{year}$ ),  $Q$  is the activation energy (in eV), and  $k$  is Boltzmann's constant. Available experimental data [49, 50] were fitted to this equation with the following parameters.

Coolant	A [ $\mu\text{m}/\text{yr}$ ]	Q [eV]
Lithium	$5.0119 \times 10^7$	1.15
LiPb	$1.22 \times 10^8$	0.99

Table 8: Dissolution rate parameters for F/M steels in Li and LiPb

The data and Arrhenius fits are shown in Figure 69. The size of the corroded layer is shown as function of time for F/M steels in lithium in Figure 70, and in LiPb in Figure 71

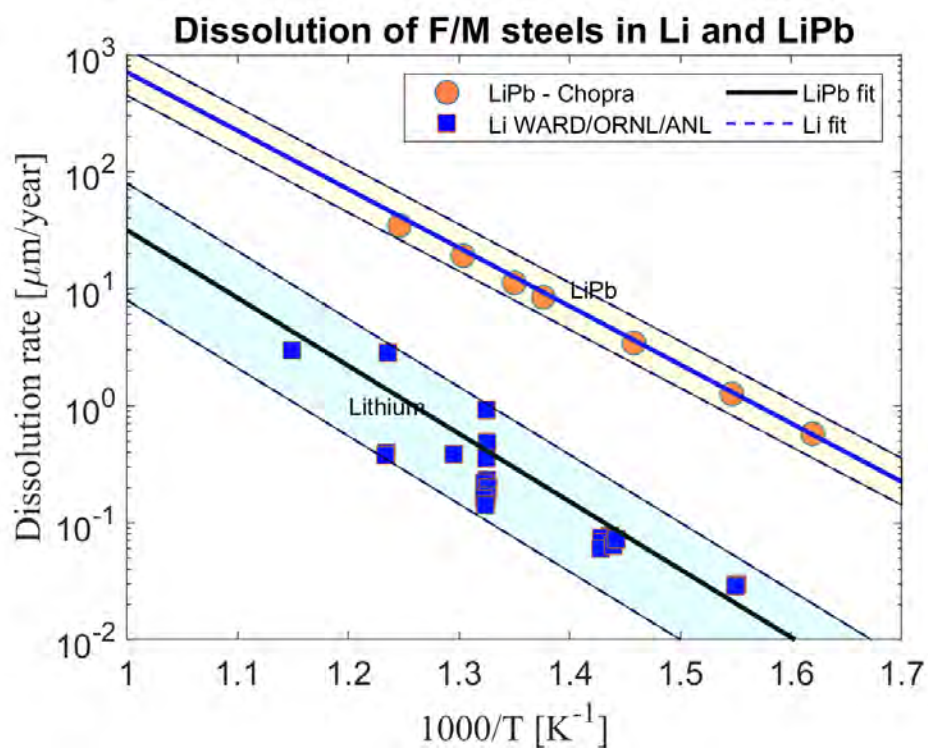


Figure 69: Dissolution rates of F/M steels in Li and LiPb [49, 50]

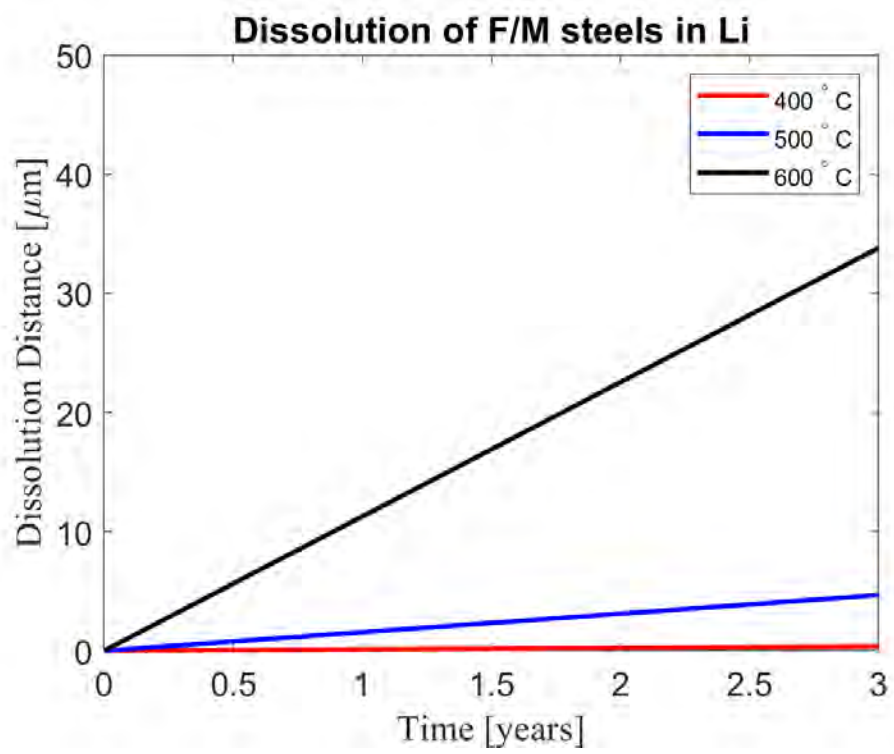


Figure 70: Dissolved layer thickness as a function of time for F/M steels in Li.

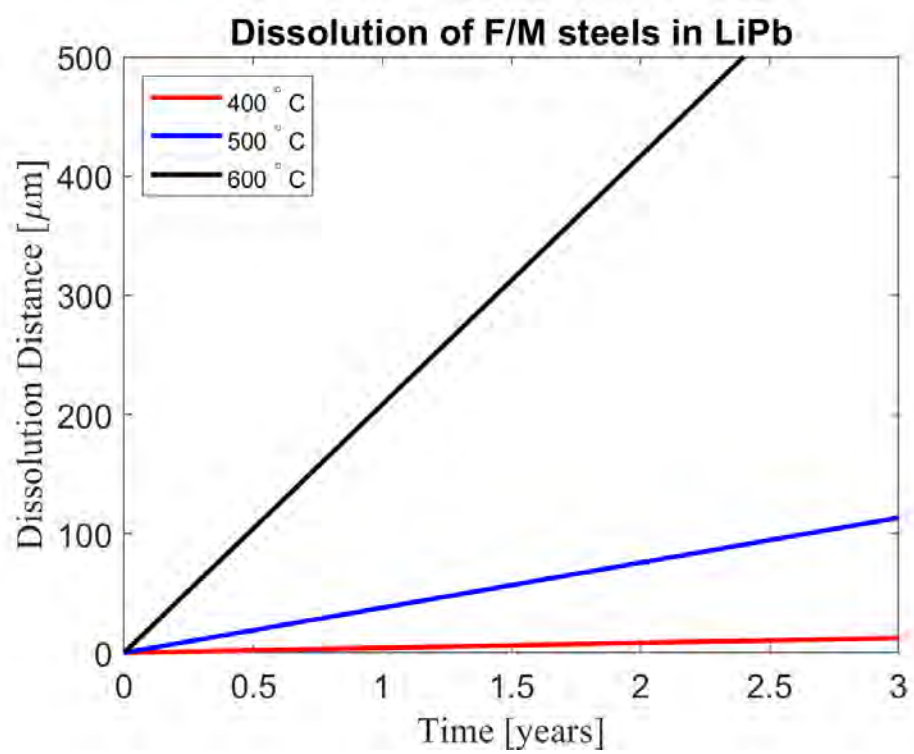


Figure 71: Dissolved layer thickness as a function of time for F/M steels in LiPb.

## 6.2 Liquid Metal Embrittlement (LME)

## 6.3 Oxidation in Steam

## References

- [1] N. Ghoniem, R. Conn, [Assessment of ferritic steels for steady-state fusion reactors](#), International Atomic Energy Agency, Vienna (Austria); Panel proceedings series IAEA-TC-392/62 (1983) 486–492.  
URL [chrome-extension://efaidnbmnnnibpcajpcglclefindmkaj/https://inis.iaea.org/collection/NCLCollectionStore/\\_Public/53/051/53051820.pdf](chrome-extension://efaidnbmnnnibpcajpcglclefindmkaj/https://inis.iaea.org/collection/NCLCollectionStore/_Public/53/051/53051820.pdf) 4
- [2] D. S. Gelles, N. M. Ghoniem, R. W. Powell, [Low activation ferritic alloys](#), US Patent No. 4622067, Tech. rep., Hanford Engineering Development Lab., Richland, WA (United States) (1985).  
URL <https://www.osti.gov/biblio/5365778> 4
- [3] N. M. Ghoniem, G. Po, S. Sharafat, [Deformation mechanisms in ferritic/martensitic steels and the impact on mechanical design](#), Journal of nuclear materials 441 (1-3) (2013) 704–712.  
URL [https://www.sciencedirect.com/science/article/pii/S0022311513005485?casa\\_token=UYhjzEEBRBOAAAAA:jOBi8Kzog7ca1mNEMSaKY9JOTFlyXkgp\\_Fcwj2AYjcmGf3cVuYfx0ID2EvKSPWuLQ8qta8SevgA](https://www.sciencedirect.com/science/article/pii/S0022311513005485?casa_token=UYhjzEEBRBOAAAAA:jOBi8Kzog7ca1mNEMSaKY9JOTFlyXkgp_Fcwj2AYjcmGf3cVuYfx0ID2EvKSPWuLQ8qta8SevgA) 4
- [4] S. Jitsukawa, M. Tamura, B. Van der Schaaf, R. Klueh, A. Alamo, C. Petersen, M. Schirra, P. Spaetig, G. Odette, A. Tavassoli, et al., Development of an extensive database of mechanical and physical properties for reduced-activation martensitic steel f82h, Journal of Nuclear Materials 307 (2002) 179–186. 4, 62
- [5] R. Chaouadi, T. Hirai, J. Linke, G. Pintsuk, [A radiation hardening model of 9% cr–martensitic steels including dpa and helium](#), Journal of nuclear materials 386 (2009) 544–549.  
URL <https://www.sciencedirect.com/science/article/pii/S0022311508009239> 4, 47
- [6] L. Tan, L. L. Snead, Y. Katoh, [Development of new generation reduced activation ferritic-martensitic steels for advanced fusion reactors](#), Journal of Nuclear Materials 478 (2016) 42–49.  
URL [https://www.sciencedirect.com/science/article/pii/S002231151630232X?casa\\_token=27f39PROABsAAAAA:5gVunHoH-W2X7vveNJMQNN8V0fnWVpkY6c7UVP5dqcg2WGDlwTsZx5P0joUkbjUvBgDTcfcWaKM](https://www.sciencedirect.com/science/article/pii/S002231151630232X?casa_token=27f39PROABsAAAAA:5gVunHoH-W2X7vveNJMQNN8V0fnWVpkY6c7UVP5dqcg2WGDlwTsZx5P0joUkbjUvBgDTcfcWaKM) 4, 6, 7, 9
- [7] Q. Huang, C. Li, Q. Wu, S. Liu, S. Gao, Z. Guo, Z. Yan, B. Huang, Y. Song, Z. Zhu, et al., [Progress in development of clam steel and fabrication of small tbn in china](#), Journal of Nuclear Materials 417 (1-3) (2011) 85–88.  
URL <https://www.sciencedirect.com/science/article/abs/pii/S002231151000992X> 4
- [8] E. Cheng, [Concentration limits of natural elements in low activation fusion materials](#), Journal of nuclear materials 258 (1998) 1767–1772.  
URL [https://www.sciencedirect.com/science/article/pii/S0022311598001342?casa\\_token=71wbfdE\\_ZDoAAAAA:gyZECxI1SCuDTlMC6fy-65SxGqwmwhyg1oEPUICRoSbtD1PXH5TT0466VQvnBv1IYjXuo1DmcQ8](https://www.sciencedirect.com/science/article/pii/S0022311598001342?casa_token=71wbfdE_ZDoAAAAA:gyZECxI1SCuDTlMC6fy-65SxGqwmwhyg1oEPUICRoSbtD1PXH5TT0466VQvnBv1IYjXuo1DmcQ8) 5
- [9] R. Lindau, A. Möslang, M. Rieth, M. Klimiankou, E. Materna-Morris, A. Alamo, A.-A. Tavassoli, C. Cayron, A.-M. Lancha, P. Fernandez, et al., [Present development status of eurofer and ods-eurofer for application in blanket concepts](#), Fusion Engineering and design 75 (2005) 989–996.  
URL [https://www.sciencedirect.com/science/article/pii/S0920379605003534?casa\\_token=uuiqiCf4LSYAAAAA:OD8b1ar77jwS4JeyV3AXtCi2N14uOcPJTlcyuMzWu-54Yms7-r6vhv1BPflTpC\\_6WDnxDplXfqg](https://www.sciencedirect.com/science/article/pii/S0920379605003534?casa_token=uuiqiCf4LSYAAAAA:OD8b1ar77jwS4JeyV3AXtCi2N14uOcPJTlcyuMzWu-54Yms7-r6vhv1BPflTpC_6WDnxDplXfqg) 6, 63



- [10] T. Hirose, K. Shiba, T. Sawai, S. Jitsukawa, M. Akiba, [Effects of heat treatment process for blanket fabrication on mechanical properties of f82h](#), Journal of nuclear materials 329 (2004) 324–327.  
URL [https://www.sciencedirect.com/science/article/pii/S0022311504001825?casa\\_token=8DVSGffxjysAAAAA:HHL0tzIxI4q0DEvE3ccDKEgVCbjpUkv4xqXcoiLNCKC4dhBuDeJvuUyZZG7gP82-SFhdp2oWS4c](https://www.sciencedirect.com/science/article/pii/S0022311504001825?casa_token=8DVSGffxjysAAAAA:HHL0tzIxI4q0DEvE3ccDKEgVCbjpUkv4xqXcoiLNCKC4dhBuDeJvuUyZZG7gP82-SFhdp2oWS4c) 6, 9, 10
- [11] K. Haarmann, J. Vaillant, B. Vandenberghe, W. Bendick, A. Arbab, [The t91/p91 book](#), Vallourec & Mannesmann Tubes 19992002 (1999).  
URL <https://drive.google.com/file/d/1QV52zaIzUeyy-GXQ01e75YvxAHiZIVf/view?usp=sharing> 7, 8
- [12] A. Chakraborty, R. F. Webster, S. Primig, [Lath martensite substructure evolution in low-carbon microalloyed steels](#), Journal of Materials Science 57 (22) (2022) 10359–10378.  
URL <https://link.springer.com/article/10.1007/s10853-022-07275-9> 7, 8, 9
- [13] X. Jia, Y. Dai, [Microstructure in martensitic steels t91 and f82h after irradiation in sinq target-3](#), Journal of nuclear materials 318 (2003) 207–214.  
URL [https://www.sciencedirect.com/science/article/abs/pii/S0022311503001016?casa\\_token=D0IRBN4C514AAAAA:aAyEzFHKYkfeeUb0\\_KaqMbNH3oaCJqtiq2gk5kVMhy-y9uqbg7qT7P9AvxNlnZaKVQLMp7qCbDQ](https://www.sciencedirect.com/science/article/abs/pii/S0022311503001016?casa_token=D0IRBN4C514AAAAA:aAyEzFHKYkfeeUb0_KaqMbNH3oaCJqtiq2gk5kVMhy-y9uqbg7qT7P9AvxNlnZaKVQLMp7qCbDQ) 11
- [14] M. Mahler, G. Po, Y. Cui, N. Ghoniem, J. Aktaa, [Microstructure-specific hardening of ferritic-martensitic steels pre and post 15 dpa neutron irradiation at 330° c: a dislocation dynamics study](#), Nuclear materials and energy 26 (2021) 100814.  
URL <https://www.sciencedirect.com/science/article/pii/S2352179120300892> 12
- [15] A.-A. Tavassoli, Present limits and improvements of structural materials for fusion reactors—a review, Journal of Nuclear Materials 302 (2-3) (2002) 73–88. 13
- [16] A.-A. Tavassoli, J.-W. Rensman, M. Schirra, K. Shiba, Materials design data for reduced activation martensitic steel type f82h, Fusion Engineering and Design 61 (2002) 617–628. 13, 14, 15, 16, 17, 18, 20, 22, 23, 24, 25, 26, 27
- [17] C. Davisson, J. Weeks, [The relation between the total thermal emissive power of a metal and its electrical resistivity](#), JOSA 8 (5) (1924) 581–605.  
URL [https://opg.optica.org/view\\_article.cfm?pdfKey=6af3cca3-d637-4e09-869803cd0c47093e\\_47617](https://opg.optica.org/view_article.cfm?pdfKey=6af3cca3-d637-4e09-869803cd0c47093e_47617) 18
- [18] A. Sievers, [Thermal radiation from metal surfaces](#), JOSA 68 (11) (1978) 1505–1516.  
URL [https://opg.optica.org/directpdfaccess/83053044-daa6-46e1-888e95578640cd01\\_57333/josa-68-11-1505.pdf?da=1&id=57333&seq=0&mobile=no](https://opg.optica.org/directpdfaccess/83053044-daa6-46e1-888e95578640cd01_57333/josa-68-11-1505.pdf?da=1&id=57333&seq=0&mobile=no) 18
- [19] T. Echániz, I. G. de Arrieta, A. Gil-Muñoz, J. Fernández-Pereda, R. Fuente, M. Klimenkov, G. López, [Infrared emissivity of reduced-activation eurofer 97 for fusion reactor applications](#), Journal of Nuclear Materials 549 (2021) 152907.  
URL <https://www.sciencedirect.com/science/article/pii/S0022311521001318> 19
- [20] E. Daum, K. Ehrlich, M. Schirra, [Proceedings of the second milestone meeting of european laboratories on the development of ferritic/martensitic steels for fusion technology](#) (1997).  
URL <https://publikationen.bibliothek.kit.edu/270041382> 22, 23, 24, 25, 26, 27
- [21] R. Klueh, [Proceedings of the iea working group meeting on ferritic/martensitic steels](#), Tech. rep., Oak Ridge National Lab. (1996).  
URL [https://inis.iaea.org/collection/NCLCollectionStore/\\_Public/28/080/28080146.pdf](https://inis.iaea.org/collection/NCLCollectionStore/_Public/28/080/28080146.pdf) 22, 23, 24, 25, 26, 27

- [22] M. F. Ashby, [A first report on deformation-mechanism maps](#), Acta Metallurgica 20 (7) (1972) 887–897.  
URL [https://www.sciencedirect.com/science/article/pii/000161607290082X?casa\\_token=NCDAoD80vLAAAAA:VcKewv\\_whUyB\\_Dextx6vMHWD6k\\_TAhWeIFLj-YXwEk-Syy1kvcp5hqzDVWFKUH3uyMk7RV4nDaQ](https://www.sciencedirect.com/science/article/pii/000161607290082X?casa_token=NCDAoD80vLAAAAA:VcKewv_whUyB_Dextx6vMHWD6k_TAhWeIFLj-YXwEk-Syy1kvcp5hqzDVWFKUH3uyMk7RV4nDaQ) 30, 31
- [23] H. J. Frost, M. F. Ashby, Deformation-mechanism maps: the plasticity and creep of metals and ceramics, (No Title) (1982). 30
- [24] K. Shiba, M. Suzuki, A. Hishinuma, [Irradiation response on mechanical properties of neutron irradiated f82h](#), Journal of Nuclear materials 233 (1996) 309–312.  
URL <https://www.sciencedirect.com/science/article/abs/pii/S0022311596002231> 30
- [25] A. K. Mukherjee, J. E. Bird, J. E. Dorn, [Experimental correlations for high-temperature creep](#) (1968).  
URL <chrome-extension://efaidnbmnmnibpcajpcglclefindmkaj/https://escholarship.org/content/qt31p4z5v2/qt31p4z5v2.pdf> 32
- [26] H. J. Ryu, Y. S. Kim, A. Yacout, [Thermal creep modeling of ht9 steel for fast reactor applications](#), Journal of nuclear materials 409 (3) (2011) 207–213.  
URL <https://www.sciencedirect.com/science/article/pii/S0022311510010676> 34
- [27] T. Shrestha, M. Basirat, I. Charit, G. P. Potirniche, K. K. Rink, [Creep rupture behavior of grade 91 steel](#), Materials Science and Engineering: A 565 (2013) 382–391.  
URL <https://www.sciencedirect.com/science/article/pii/S0921509312017194> 37, 38
- [28] M. Tamura, M. M. Nowell, K. Shinozuka, H. Esaka, [Creep behavior of double tempered 8% cr-2% wyta martensitic steel](#), Materials transactions 47 (5) (2006) 1332–1340.  
URL [https://www.jstage.jst.go.jp/article/matertrans/47/5/47\\_5\\_1332/\\_pdf](https://www.jstage.jst.go.jp/article/matertrans/47/5/47_5_1332/_pdf) 41
- [29] K. Shinozuka, H. Esaka, H. Sakasegawa, H. Tanigawa, [Creep strength and microstructure of f82h steels near tempering temperature](#), Journal of Nuclear Materials 464 (2015) 155–159. doi:<https://doi.org/10.1016/j.jnucmat.2015.04.035>.  
URL <https://www.sciencedirect.com/science/article/pii/S0022311515002457> 42
- [30] R. G. Budynas, J. K. Nisbett, et al., Shigley’s mechanical engineering design, Vol. 8, McGraw-Hill New York, 2008. 43, 44
- [31] D. S. Gelles, N. M. Ghoniem, R. W. Powell, Low activation ferritic alloys, uS Patent 4,622,067 (Nov. 11 1986). 45
- [32] T. Hirose, T. Kato, H. Sakasegawa, H. Tanigawa, T. Nozawa, [Evaluation of fatigue properties of reduced activation ferritic/martensitic steel, f82h for development of design criteria](#), Fusion Engineering and Design 160 (2020) 111823. doi:<https://doi.org/10.1016/j.fusengdes.2020.111823>.  
URL <https://www.sciencedirect.com/science/article/pii/S0920379620303719> 45, 46
- [33] M. Makin, F. Minter, [Irradiation hardening in copper and nickel](#), Acta Metallurgica 8 (10) (1960) 691–699.  
URL <https://www.sciencedirect.com/science/article/pii/0001616060902005> 47
- [34] H. Trinkaus, [The effect of cascade induced gas resolution on bubble formation in metals](#), Journal of nuclear materials 318 (2003) 234–240.  
URL [https://www.sciencedirect.com/science/article/pii/S002231150300103X?casa\\_token=90X1wPjVsEkAAAAA:2Z9ijHA9H6LjW25fqsj\\_ofD8yoFFfYctiEbczTwl5Eg7xmQShingvuIySCAFYdDGTc6k5dqDTME](https://www.sciencedirect.com/science/article/pii/S002231150300103X?casa_token=90X1wPjVsEkAAAAA:2Z9ijHA9H6LjW25fqsj_ofD8yoFFfYctiEbczTwl5Eg7xmQShingvuIySCAFYdDGTc6k5dqDTME) 47

- [35] T. Yamamoto, G. R. Odette, H. Kishimoto, J.-W. Rensman, P. Miao, [On the effects of irradiation and helium on the yield stress changes and hardening and non-hardening embrittlement of 8cr tempered martensitic steels: Compilation and analysis of existing data](#), *Journal of nuclear materials* 356 (1-3) (2006) 27–49.  
URL [https://www.sciencedirect.com/science/article/pii/S0022311506002418?casa\\_token=MiqueuMK4H\\_sAAAAA:yAuneQmW0\\_R5\\_2EhbrgljPpPOPJBuogzAckJ1McqDX3uAhNecOdAHhf\\_STMAfKcPcYfCEqWHApA](https://www.sciencedirect.com/science/article/pii/S0022311506002418?casa_token=MiqueuMK4H_sAAAAA:yAuneQmW0_R5_2EhbrgljPpPOPJBuogzAckJ1McqDX3uAhNecOdAHhf_STMAfKcPcYfCEqWHApA) 47, 48
- [36] E. Gaganidze, J. Aktaa, [Assessment of neutron irradiation effects on rafm steels](#), *Fusion Engineering and Design* 88 (3) (2013) 118–128.  
URL [https://www.sciencedirect.com/science/article/pii/S0920379612005364?casa\\_token=ADuHwhFwETAAAAA:CsQBQLLjxjxusjxvsElCiAcIUJ97550qtrdF1Tp7kU11owMcVA6rstrJ-fcpCi8jchf3cK0AT\\_c](https://www.sciencedirect.com/science/article/pii/S0920379612005364?casa_token=ADuHwhFwETAAAAA:CsQBQLLjxjxusjxvsElCiAcIUJ97550qtrdF1Tp7kU11owMcVA6rstrJ-fcpCi8jchf3cK0AT_c) 51, 54
- [37] E. Gaganidze, C. Petersen, [Post irradiation examination of rafm steels after fast reactor irradiation up to 71 dpa andj 340 c \(arbor 2\). rafm steels. metallurgical and mechanical characterisation. final report for tw5-ttms-001, d 10](#) (2011).  
URL <https://www.osti.gov/etdeweb/biblio/22599430> 52, 54
- [38] T. Yamamoto, G. R. Odette, [A fusion relevant data-driven engineering void swelling model for 9cr tempered martensitic steels](#), *Journal of Nuclear Materials* 576 (2023) 154085.  
URL <https://www.sciencedirect.com/science/article/pii/S0022311522005669> 57
- [39] A. Brailsford, R. Bullough, [The rate theory of swelling due to void growth in irradiated metals](#), *Journal of Nuclear Materials* 44 (2) (1972) 121–135. doi:[https://doi.org/10.1016/0022-3115\(72\)90091-8](https://doi.org/10.1016/0022-3115(72)90091-8).  
URL <https://www.sciencedirect.com/science/article/pii/0022311572900918> 57, 58
- [40] E. Wakai, N. Hashimoto, Y. Miwa, J. Robertson, R. Klueh, K. Shiba, S. Jitsukawa, [Effect of helium production on swelling of f82h irradiated in hfir](#), *Journal of Nuclear Materials* 283-287 (2000) 799–805, 9th Int. Conf. on Fusion Reactor Materials. doi:[https://doi.org/10.1016/S0022-3115\(00\)00268-3](https://doi.org/10.1016/S0022-3115(00)00268-3).  
URL <https://www.sciencedirect.com/science/article/pii/S0022311500002683> 57, 59, 60
- [41] E. Getto, K. Sun, A. Monterrosa, Z. Jiao, M. Hackett, G. Was, [Void swelling and microstructure evolution at very high damage level in self-ion irradiated ferritic-martensitic steels](#), *Journal of Nuclear Materials* 480 (2016) 159–176. doi:<https://doi.org/10.1016/j.jnucmat.2016.08.015>.  
URL <https://www.sciencedirect.com/science/article/pii/S0022311516305931> 57, 59, 60
- [42] K. Ehrlich, [Irradiation creep and interrelation with swelling in austenitic stainless steels](#), *Journal of Nuclear Materials* 100 (1) (1981) 149–166. doi:[https://doi.org/10.1016/0022-3115\(81\)90531-6](https://doi.org/10.1016/0022-3115(81)90531-6).  
URL <https://www.sciencedirect.com/science/article/pii/0022311581905316> 61, 69
- [43] S. Jitsukawa, A. Kimura, A. Kohyama, R. Klueh, A. Tavassoli, B. Van der Schaaf, G. Odette, J. Rensman, M. Victoria, C. Petersen, [Recent results of the reduced activation ferritic/martensitic steel development](#), *Journal of Nuclear Materials* 329 (2004) 39–46.  
URL [https://www.sciencedirect.com/science/article/pii/S0022311504001229?casa\\_token=kDGkrTvtzpAAAAA:uTHXgwWp1BB-eSuGg9PJEpj2MJ7gl1sn7Y8nOoaHZPfrceVFWV7ArpjtzeFx3dnGGsqMr8Is08g](https://www.sciencedirect.com/science/article/pii/S0022311504001229?casa_token=kDGkrTvtzpAAAAA:uTHXgwWp1BB-eSuGg9PJEpj2MJ7gl1sn7Y8nOoaHZPfrceVFWV7ArpjtzeFx3dnGGsqMr8Is08g) 64
- [44] R. Klueh, D. Gelles, S. Jitsukawa, A. Kimura, G. Odette, B. Van der Schaaf, M. Victoria, [Ferritic/-martensitic steels—overview of recent results](#), *Journal of Nuclear Materials* 307 (2002) 455–465.  
URL [https://www.sciencedirect.com/science/article/pii/S0022311502010826?casa\\_token=0I39hI1WGvcAAAAA:npMtr78a9Y3-ZS0nuJi\\_nnniItI3IJqMz70ZwlxRSVIsypGWJ7cKaaQvMtqA6izzw8cMDNVjDY](https://www.sciencedirect.com/science/article/pii/S0022311502010826?casa_token=0I39hI1WGvcAAAAA:npMtr78a9Y3-ZS0nuJi_nnniItI3IJqMz70ZwlxRSVIsypGWJ7cKaaQvMtqA6izzw8cMDNVjDY) 65, 66

- [45] K. Herschbach, W. Schneider, K. Ehrlich, [Effects of minor alloying elements upon swelling and in-pile creep in model plain fe-15cr-15ni stainless steels and in commercial din 1.4970 alloys](#), Journal of Nuclear Materials 203 (3) (1993) 233–248. doi:[https://doi.org/10.1016/0022-3115\(93\)90380-H](https://doi.org/10.1016/0022-3115(93)90380-H). URL <https://www.sciencedirect.com/science/article/pii/002231159390380H> 69
- [46] F. Garner, M. Toloczko, B. Sencer, [Comparison of swelling and irradiation creep behavior of fcc-austenitic and bcc-ferritic/martensitic alloys at high neutron exposure](#), Journal of Nuclear Materials 276 (1) (2000) 123–142. doi:[https://doi.org/10.1016/S0022-3115\(99\)00225-1](https://doi.org/10.1016/S0022-3115(99)00225-1). URL <https://www.sciencedirect.com/science/article/pii/S0022311599002251> 69
- [47] M. Ando, T. Nozawa, T. Hirose, H. Tanigawa, E. Wakai, R. E. Stoller, J. Myers, [Effect of helium on irradiation creep behavior of b-doped f82h irradiated in hfir](#), Fusion Science and Technology 68 (3) (2015) 648–651. arXiv:<https://doi.org/10.13182/FST14-963>, doi:10.13182/FST14-963. URL <https://doi.org/10.13182/FST14-963> 69, 70
- [48] P. Tortorelli, [Dissolution kinetics of steels exposed in lead-lithium and lithium environments](#), Journal of Nuclear Materials 191-194 (1992) 965–969. doi:[https://doi.org/10.1016/0022-3115\(92\)90617-T](https://doi.org/10.1016/0022-3115(92)90617-T). URL <https://www.sciencedirect.com/science/article/pii/002231159290617T> 73
- [49] O. Chopra, D. Smith, [Compatibility of ferrous alloys in a forced circulation pb-17li system](#), Journal of Nuclear Materials 141-143 (1986) 566–570. doi:[https://doi.org/10.1016/0022-3115\(86\)90055-3](https://doi.org/10.1016/0022-3115(86)90055-3). URL <https://www.sciencedirect.com/science/article/pii/0022311586900553> 73, 74
- [50] O. Chopra, D. Smith, [Compatibility of ferritic steels in forced circulation lithium and pb-17li systems](#), Journal of Nuclear Materials 155-157 (1988) 715–721. doi:[https://doi.org/10.1016/0022-3115\(88\)90402-3](https://doi.org/10.1016/0022-3115(88)90402-3). URL <https://www.sciencedirect.com/science/article/pii/0022311588904023> 73, 74